ENDOGRAFTS, PRESSURE, AND THE ABDOMINAL AORTIC ANEURYSM

A Dissertation

by

CLARK ANDREW MEYER

Submitted to the Office of Graduate Studies of
Texas A&M University
in partial fulfillment of the requirements for the degree of

DOCTOR OF PHILOSOPHY

May 2009

Major Subject: Biomedical Engineering

ENDOGRAFTS, PRESSURE, AND THE ABDOMINAL AORTIC ANEURYSM

A Dissertation

by

CLARK ANDREW MEYER

Submitted to the Office of Graduate Studies of
Texas A&M University
in partial fulfillment of the requirements for the degree of

DOCTOR OF PHILOSOPHY

Approved by:

Chair of Committee, James E. Moore, Jr.
Committee Members, Jay D. Humphrey
Wonmuk Hwang
Christopher Quick
Head of Department, Gerard Coté

May 2009

Major Subject: Biomedical Engineering

ABSTRACT

Endografts, Pressure, and the Abdominal Aortic Aneurysm. (May 2009)

Clark Andrew Meyer, B.S., Texas A&M University

Chair of Advisory Committee: Dr. James E. Moore, Jr.

Abdominal aortic aneurysms (AAA) are an expansion in diameter of the abdominal aorta and their rupture is a leading cause of mortality. One of the treatments for AAA is the implantation of an endograft (also called a stent graft), a combination of fabric and metal stents, to provide a new conduit for blood and shield the aneurysm sac from direct pressurization. After implantation of the stent graft, the aneurysm may shrink, grow, or stabilize in diameter – even in the absence of apparent flow into the sac – in some cases resulting in graft failure through component separation, kinking, or loss of seal at its ends.

Greater understanding of AAA and treated AAA could provide insight on how treatment might be modified to improve treatment methods and/or design devices to be more effective in a wider range of patients. Computational models provide a means to investigate the biomechanics of endografts treating AAA through analysis of the endografts, the AAA, and the combination of them.

Axisymmetric models of endograft-treated AAA showed that peak von Mises stress within the wall varied between 533 kPa and 1200 kPa when different material properties for the endograft were used. The patient-specific models, built from time

series of patient CT scans with similar patient history but different outcomes, show that wall shrinkage and stability can be related to the level of stresses within the vessel wall, with the shrinking AAA showing a greater reduction by endograft treatment and a lower final value of average von Mises stress. The reduction in pressure felt by the wall is local to the central sac region. The inclusion of thrombus is also essential to accurate stress estimation.

The combination of axisymmetric and patient-specific computational models explains in further detail the biomechanics of endograft treatment. The patient-specific reconstruction models show that when effectively deployed and reducing the pressure felt in the AAA wall, the graft is under tension in the sac region and compression at its ends.

ACKNOWLEDGEMENTS

This work would not have been possible without the assistance of the many people that helped directly and indirectly. Thanks are due to Drs. Clifford Buckley and Bob Feldtman of Scott & White in Temple, Texas for their contributions to my understanding of the clinical situation endografts are in through discussions and surgical observation. Also, special thanks to Shirley Buckley for her assistance with CT scans and coordination of the IRB approval process.

Professors have been very helpful with this work and my progression as a graduate student. In particular I would like to thank Dr. Humphrey for encouraging greater depth of thought on assumptions, Dr. Hwang for his encouragement and critical thinking skills in his courses, and Dr. Criscione for his perspective on research.

I thank Dr. Moore for his assistance, guidance, and tolerance as I worked on this project in addition to the funded stent work. The stent design work is not presented here, but details of it can be found in Lucas Timmins's dissertation (upcoming) and Julian Bedoya's thesis as well as the journal publications done with them as co-authors.

I would also like to thank the many people I have worked with while in the Moore lab group. These people include those I only worked with for a few summer months like Rebecca Dahlin, Matt Magnuson, Jamie Golson, and Kindall Carleton to many months like Fillipo Piffaretti, Krithika Sharma nee Veluchamy, Andy Peters, and Will Richardson to those that spent years with me like Julian Bedoya, Daisuke Mori, Shiva Yazdani-Beioky, Ellie Rahbar, Joao Soares, Mike Moreno, and Luke Timmins.

Each of them helped me by answering questions or testing my knowledge and encouraging deeper understanding, as well as just plain encouraging me on slow days. Particular thanks also to Rebecca Dahlin for assistance with the CT to FEM model conversion process as well as to Luke Timmins and Heather Hayenga for help with the figure preparation.

I would like to thank the friends I have made through graduate school and my side projects. They made my time very enjoyable. I look forward to staying in touch and hope to see them often.

I want to also thank my family for their support and understanding as I undertook this process.

I also would like to thank anyone reading this that I do not directly know. Please contact me anytime if you have any questions at all about the work presented herein. My contact information is on the last page as part of the vita. This dissertation represents years of work and it would be nice to know it even gets read. I will welcome any opportunity to explain it further or clarify any of it.

NOMENCLATURE

AAA	Abdominal Aortic Aneurysm
CT	Computed tomography
DICOM	Digital Imaging and Communications in Medicine
ECM	Extracellular matrix
EVAR	Endovascular repair
FEM	Finite element method
ILT	Intraluminal thrombus
IRB	Institutional review board
MMP	Matrix metalloproteinase
RPI	Rupture prediction index

TABLE OF CONTENTS

Page

Page

LIST OF FIGURES

Page

Page

Page

Page

Page

Page

LIST OF TABLES

Page

Page

1. INTRODUCTION

It is currently unknown what the key factors are in modeling the endovascular treatment of abdominal aortic aneurysm (AAA). Isolation and specification of what must be known about factors like geometry, mechanical properties, and boundary conditions with greatest precision would be useful for building models that can predict the likely success of treatment with greater accuracy. Greater understanding of AAA modeling could provide insight on how treatment might be modified to improve treatment methods and/or devices to be more effective in a wider range of patients. The work detailed in this dissertation addresses the issue of what key factors are in modeling treatment of AAA and shows the effect of the endograft on the stress imposed on the aneurysm wall.

1.1 Basic Overview

Abdominal aortic aneurysms (AAA) are focal dilatations (greater than 1.5x nominal diameter of ~ 2 cm) of the abdominal aorta [1]. The expansion sometimes includes the iliac arteries and/or a portion of the aorta proximal to the renal arteries. AAA rupture is usually fatal with 65% chance of surviving to the hospital, a 41% chance of surviving until surgery [2], and 48.5% chance of surviving emergency surgery for rupture [3]. The likelihood of rupture has been correlated to the diameter (unpressurized) of the aneurysm in autopsy studies, but some small aneurysms do rupture and some large ones do not [4, 5]. An autopsy based study by da Silva et al. used a balloon inflation (80 mmHg) technique to better quantify size. They saw most

---

This dissertation follows the style of Journal of Biomechanical Engineering.

ruptures occurred in the posterior-inferior wall (62% of 49 individuals) and were also related to aneurysm shape although they saw no ruptures of < 5.0 cm aneurysms [6]. Fillinger et al. showed in a small study that maximum stress was a better predictor of rupture than maximum diameter, which is currently the primary clinical factor for predicting rupture [7].

The endograft, a component of one of the two primary treatment methods available, is implanted to isolate the aneurysm wall from arterial pressure and provide a reliable conduit for blood flow in the event of a rupture. The use of endografts in the treatment of AAA is a promising therapeutic option that is as of yet underdeveloped. Presently, the use of endografts has led to short term improvements in the technical success of the procedure and the ability to treat patients with more co-morbidity; however device/implantation failures can result in death or require conversion of the procedure to an open surgical repair or an operation to reseat the device. Endograft patients require an annual follow-up CT scan to monitor for failures. The second operation is particularly problematic as many patients receive endograft therapy because they are not considered viable candidates for open repair, i.e. open repair for these patients is considered extremely high risk because of advanced age or co-morbid conditions. The inability to re-seat the device correctly or successfully complete an open repair following device/implantation failure can result in death.

When the endograft is deployed correctly, blood flow will be diverted through the graft, which serves as a conduit that extends through the aneurysm sac. Ideally, as flow is diverted through the endograft, flow-induced pressure on the aneurysm wall is

reduced – see Figure 1. Consequently, stresses in the aneurysm wall would decrease as would the likelihood of aneurysm rupture. A second function of the endograft is to provide a reliable conduit for blood flow even if there is a rupture. This, of course, requires reliable sealing of the proximal and distal fixation points as well as endograft component junctions. It is also necessary that the fabric portion remain intact and clotted adequately.

Figure 1. The graft is located below the renal arteries inside the abdominal aorta and continues into the iliac arteries, providing a path for blood and preventing blood contact with the aneurysm sac. (Source: http://www.nhlbi.nih.gov/health/dci/Diseases/arm/arm_treatments.html)

1.2 Objective and Aims

The goal of this study was to elucidate some of the biomechanical factors involved in achieving a reduction of stress in the aneurysm wall, to quantify this reduction as a function of the endograft therapy and initial patient conditions, and thereby reveal information on the conditions that increase the success rate of endograft therapy. The expectation was that stress is reduced by treatment, with the reduction most dependent on the endograft's material properties and shape. It was also expected that in cases where the graft is significantly reducing stress on the AAA wall, a course of imaging studies will show reductions in diameter, and that there would be minimal size reductions in other cases and regions. Based on standard material failure criteria and understanding that rupture is ultimately material failure, stress was investigated and modeled. It is expected that results of this study will contribute to improvements in the design of endograft devices as well as potentially provide technology and tools for the development of patient-specific treatment plans and expectations. The specific aims of this project were:

1. Develop and analyze axisymmetric models of AAAs in which an axisymmetric model of an endograft is deployed. These models incorporated material properties that account for a plausible range of mechanical behaviors and are suitable for use in large strain/deformation analyses. The material properties employed were obtained from the literature or derived from experiments [8, 9].

2. Develop patient-specific solid mechanical models of AAAs from CT data treated with endografts. Variations between endografts and anatomy were expected to be a key part of modeling the stress field.

3. Analyze a series of patient-specific solid mechanical models of AAAs treated with endografts over a period of 2 years. A series of models allowed for analysis of the changes in geometry and stress fields over time and provided insight on the effect on remodeling.

4. With the results obtained from aims 1 and 2, determine the effects of the key modeling assumptions on outcomes. The relative importance and costs of using the more advanced material models and patient-specific models as opposed to the more basic models was assessed.

The mechanical models are finite element models which are based on the finite element method (FEM) concept of breaking a problem into components called elements. For more detail, see Chapter VI as it covers the basics of FEM as well as the underlying continuum mechanics framework are discussed in greater detail. Chapter II discusses AAA in detail.

The investigation and characterization of endograft mechanical performance in patient-specific and axisymmetric models provided insight on their respective usefulness and appropriateness in certain cases as well as indications related to the level of complexity in modeling that is necessary for a particular level of precision in analysis (Specific Aims #1, #2, and #4). The investigation also provided an answer to the question; does an endograft really reduce stress in the AAA wall (Specific Aim #3)?

The results of this study may also allow for better decision making on how and when to treat individual patients by providing a method for analysis of stress and outcome prediction based on their specific anatomy, i.e. provide the foundation for the development of a clinical diagnostic tool that can help predict when to expect growth, shrinkage, or stability after graft placement.

2. ABDOMINAL AORTIC ANEURYSMS

2.1 Biology of AAA

Abdominal aortic aneurysms are a problem of the cardiovascular system. The system encompasses the arteries, such as the aorta, as well as the heart, veins, and capillaries. It holds approximately 5.5 L of blood [10]. The arterial circulation contains approximately 17% of the blood. It transports approximately 6 L/min [11]. This volume is distributed amongst the vasculature, with approximately 0.9 L/min amount traveling through the infrarenal aorta at rest and approximately 5.5 L/min at exercise [12]. These average values shown above are all subject to various assumptions, such as activity level, disease state, patient size, and age which can influence the amount and distribution of flow.

Blood flow is an important consideration for abdominal aortic aneurysms because through its dynamic action of flow it supplies the internal forces contributing to the biomechanical environment of aneurysms. The modeling of blood flow within AAA has been done by groups as a foundation to work combining flow and wall motion. This work typically considers blood to be a Newtonian fluid. This simplification ignores the particulate nature (suspension of cells in plasma) of blood, but it affords a reasonable model in vessels greater than 0.5 mm in diameter [13]. Other models incorporate the non-Newtonian behavior of blood, which accounts for viscosity changing with shear rate. Further modeling of the flow environment has been used to elucidate flow patterns within the AAA/aorta.

2.1.1 Anatomy

The aorta is the name given to the branch of vasculature extending up from the heart, arching over and continuing down to the bifurcation point, near the navel. At this bifurcation point, the aorta splits into the common iliac arteries. Along the path of the aorta there are many arteries branching off, supplying blood to different areas and organs. Particularly noteworthy are the renal arteries, which supply blood to the kidneys and typically are just proximal to the aneurysm. The abdominal aorta is the portion below the diaphragm and a continuation of the descending aorta (of the thorax).

Abdominal aortic aneurysms are "true" aneurysms in the sense that the wall is comprised of all three layers of the artery wall – intima, media, and adventitia [14]. A dissecting or "false" aneurysm is where the dilation is a result of blood flowing into the wall directly and separating the layers such that outer layers are directly loaded and separated from the lumen. The intima of an AAA patient is more than just a monolayer of endothelial cells, as the aorta in human patients of advanced age has thickened considerably.

The infrarenal aorta in humans has fewer, or at least less developed, vasa vasorum than that of other mammals and it is suspected that a relatively local ischemia could weaken the wall and provide means for eventual dilatation [14].

2.1.2 Vessel Wall Structure

An artery wall consists of three fundamental layers – the intima, the media, and the adventitia – listed inner to outer. The intima consists of a layer of endothelial cells except in the aorta where a subendothelial layer connective tissue and axially oriented

smooth muscle cells are present. The endothelial cells provide an anti-thrombogenic surface that prevents the formation of clots. The intima is separated from the media by a porous membrane consisting primarily of elastin. The media consists primarily of smooth muscle cells, which provide vascular tone and can further contract/relax to alter the diameter of the vessel. These cells are present in layers separated by layers of lamina, into what are called lamellar units, in elastic arteries. The outermost layer of the vessel is the adventitia, which primarily consists of collagen I fibers and fibroblast cells [15].

The human abdominal aorta has very little vasa vasorum (and typically none in the medial layer). Also present in the vessel is the extra cellular matrix, which consists of collagen, elastin, and other substances. These components provide much of the passive structural properties of the artery as has been shown through enzyme treated vessels [16]. The lumen of an AAA may also have some other pathogenic/diseased structures present. Specifically, the presence of atherosclerosis or its beginnings as fatty streaks is likely in patients with advanced age. These streaks consist of macrophages that have become engorged on lipids to become foam cells. There may also be calcification and thrombus.

At the cellular structure, endothelial cells are typically 0.2 to 0.5 μm thick by 10 to 15 μm wide by 25 to 50 μm long, and provide a monolayer along the lumen [15]. They align with the direction of flow under flow conditions. Cyclic stretch also leads to alignment. This alignment reflects a response of cells to mechanical stimuli [17]. Smooth muscle cells will proliferate when under greater loads. Fibroblasts will also

respond to changes in their mechanical environment through changing rate and ratio of protein synthesis products [15].

Cells connect to their environment through focal adhesions. The focal adhesions are localized anchor points which are connected using actin fibers. The structure of the cell consists of the cytoskeleton which includes actin fibers, microtubules, and intermediate filaments. These three components are the load bearing components of a cell. These structures can be activated by loading and their structures modified by the cell, in response to these loads. Cells also respond to signals other than mechanical. They react to autocrine or paracrine signaling pathways. These molecules include vasoactive agents like nitric oxide (NO), prostacyclin, interleukins, and matrix metalloproteinases (MMPs). The MMPs and their inhibitors (TiMPs) function to regulate cellular production of proteins and have been implicated in the development of AAA. It is noteworthy that the implication of MMP and TiMPs is primarily based upon an induced animal model of AAA. There is as yet no well accepted concept explaining the detailed beginnings of the development of an AAA. There is implication of the inflammatory process gone awry. Interestingly, diabetics are less likely to develop AAA but smokers are more likely [18].

2.1.3 Cell Mechanics

The cell's structural components include a phospholipid bilayer, cytoskeleton, and organelles, with the primary structural rigidity provided by the cytoskeleton. The bilayer is spanned by integrins and has attachment points that connect the cell to other cells or extra cellular matrix (ECM). The bilayer itself, with its primary components of

phospholipids does not provide much rigidity. The organelles supply materials and connect to some of the internal structures but also do not provide much rigidity. The rigidity of the cells is provided primarily by the cytoskeleton.

The cytoskeleton is comprised of microtubules, intermediate filaments, and actin filaments. The pipe-like microtubules have an outer diameter of ~25 nm, an inner diameter of ~18nm, and a length of tens of microns. The intermediate filaments are analogous to rope with a diameter of ~10nm and a persistence length of ~1 micron. They are highly resistant to elongation, much less resistant to bending and twisting. The actin filaments are cable like with a diameter of ~6nm with lengths of tens of microns. Together the components of the cytoskeleton provide most of the structural rigidity of a cell and thus support any loading of it [19].

The cells themselves through signaling can change their functionality from synthetic to proliferative to quiescent states/phenotypes. The synthetic state produces materials used in and outside the cell. The proliferative phenotype produces more cells similar to the parent cell. The quiescent cell is in a state of equilibrium, appearing to not do much interacting with its environment or itself. These states are brought about by loading and signaling conditions.

2.2 Etiology and Development

Since the growth of the aorta into an aneurysm involves cellular changes and a general inflammation, including leukocyte infiltration, throughout the media and adventitia, in addition to B cells and macrophages. The aortic wall weakness and dilatation that could result in rupture are associated with a breakdown of elastic structure

and organization. It has been shown that the macrophages present contribute to pathology in animal models by their production of matrix metalloproteinases (MMPs) and macrophages are present in greater numbers in AAA. A study looking at the role of natural killer cells, an immune system cell type, showed that this kind of cells have an increased prevalence in patients with AAA as compared to age matched controls; this increase in prevalence is in contrast to effects of smoking. The natural killer cells also showed an increase in their cytotoxicity. This study was undertaken because of the natural killer cells are known to initiate damage, direct inflammatory response, and sustain inflammation [20]. Other immune cells have been implicated in end stage AAA. Specifically that type 1 CD4+ T cells are the most common type within human AAA and that these cells produce elevated IFN-gamma and T-bet [21].

2.2.1 Risk Factors

The primary risk factors for developing AAA include a history of smoking, high blood pressure, high cholesterol, family history, male gender, and advanced age. The family history link is associated with connective tissue disorders like Marfan's as well as some genetic markers. Smoking is thought to contribute to vascular injury and impaired repair processes. Age is associated with reductions in the repair and remodeling processes of the arteries. The explanation of the link between gender and risk for AAA development is less clear. However, with the projected increase in the age of the population, an increase in the prevalence of AAA is expected and has been observed [22].

Interestingly, one of the protective factors inhibiting risk of AAA growth and development is diabetes. The odds of getting AAA if one has diabetes are half the odds of getting AAA if one does not have diabetes. This difference was determined by a study that screened a large population of Veterans looking at a variety of risk factors. The study was at a loss to explain why there is a reduced occurrence rate of AAA in diabetic populations [23]. A subsequent study looked at possible ways diabetes makes AAA less common (though not entirely prevented). The mechanism proposed and identified was de-activating effect, by presence of advanced glycation end products that reduces their production of MMPs. The authors demonstrated that the response of human monocytes to advanced glycation depends on the type of protein glycated and its form at presentation. Their study also found that patients with diabetes experienced slower aneurysm growth over a 3 year follow-up period [24].

2.2.2 Animal Models

There are a variety of animal models of AAA that have been developed to better understand the progression and development of the pathology. These animal models vary in how the aneurysm is generated (chemical solution or surgery) and the animals it is generated in (mouse, rat, dog, pig, etc). The variety provides models that are more suitable to experiments with different immediate aims.

A patch model, where arterial tissue is sewn into an aorta to achieve a locally larger diameter, was used for testing the impact of thrombus on pressure application to the vessel wall by Pacanowski et al. [25]. They used mongrel dogs and patches from the thoracic aorta sewn into an explanted and flow-rigged abdominal aorta. They showed

that pressure to the aneurysm wall decreased following graft deployment and that strain and pressure were not evenly distributed in the sac. Though there are some fundamental limitations of their technique, it did show the basic response that endotension at high levels is related to leak, and that thrombus can transmit some pressure even without a leak [25].

2.3 Mechanical Environment of the AAA

The mechanical environment within AAA has been subject to study due to its relationship to remodeling and rupture. Essential to the mechanics of the AAA is the pressure applied to the interior as this is the largest load placed on the aneurysm, although loading from axial tethering and other loads such as fluid shear could be significant. These loads give rise to stress and strain within the aneurysm wall.

2.3.1 Pressure Measurement

Pressure within the aorta is highly related to systemic blood pressure [26]. Pressure between patients will vary as a result of hypertension (a common risk factor for AAA), general health, and variations during the day as a result of circadian rhythms and exercise. Aortic pressure can be measured directly through invasive techniques or inferred from brachial measurements (either invasive or not).

One method for invasive measurement was described by Schurink et al. 2000 [27], where a 19-guage needle connected to a pressure measuring device was punctured just through the wall into the thrombus in 9 human patients. The point of this procedure was to determine the amount of pressure in between the wall and the thrombus, to see if pressure can be transmitted through thrombus – and by their results, it can.

Another invasive technique involves the implantable pressure sensor. These sensors are used to measure recurrent pressurization of the aneurysm sac, but have not yet made it to current surveillance protocols [28].

The relationship between peripheral arterial pressure and aortic pulse pressure was shown to be an underestimation of the pulse pressure within the abdominal aorta by a mean of 10% with a sphygmomanometer which was similar to a finger cuff measuring device [29]. These measurements are, of course, not for use in patients with evidence of peripheral vascular disease of the arms, not uncommon in the elderly patients with AAA.

The preliminary study by Sonesson et al. showed reduction in pressure to 20 % of mean intra-aortic pressure in patients with median shrinkage of 12 mm, 20 months (median) after treatment of AAA by endograft [30]. Further study has shown a relationship between pressures in the between the graft and wall and failure rate. They also show pressure is 19% of mean pressure index in shrinking, 30% in unchanged (stable), and 59% in expanding aneurysm without endoleaks [31].

2.3.2 Law of Laplace

Law of Laplace is a simplistic theory useful for calculating average circumferential stresses within thin walled structures (i.e. tubes). It can be derived by considering half of the tube (split lengthwise), with thickness h, length L and radius r – then doing a balance of forces. Consider the axes such that the x-axis is aligned with the tube direction, then y and z are perpendicular to it. The pressure acts on the interior of the tube, due to the symmetric nature, the balance of forces acting in the y-direction, if split along x=0, is equal to a net of zero because the tube is not in motion. The force

from the pressure in the y direction when integrated over the area comes to: $F = 2 \cdot P \cdot r \cdot L$. This force must be equal to the twice the tension in the tube because there are two edges of the tube crossing the x = 0 line. Tension is equal to circumferential stress multiplied by tube area: $T = \sigma \cdot A$. Solving for stress, one finds it is equal to pressure multiplied by radius and divided by thickness: $\sigma = \frac{P \cdot r}{h}$. This method provides an approximate value average circumferential stress, but it fails to take into account that the stress within the wall is not uniform because the wall is in fact of finite thickness and non-negligible bending stiffness [11]. The analysis also requires a circular cross-section but most AAA do not have a true consistently circular cross-section [32] .

A similar calculation can be done for thin walled spheres. The result is average wall stress is equal to pressure times radius divided by twice the thickness: $\sigma = \frac{P \cdot r}{2h}$. A sphere has effectively half the stress of a cylinder with same load, radius, and thickness [11].

Another means of estimating wall stress is the "modified Law of Laplace" which relies additionally on an area ratio of thrombus to wall (α) and asymmetry index (β)[33] with: $\sigma = 0.006 \frac{(1-0.68\alpha)\left(e^{0.0123\left(0.85 p_{sys} + 19.5 d_{AAA,\max}\right)}\right)}{t^{0.63}\beta^{0.125}}$ (MPa). The thickness can also be approximated with a correlation of: $t = 3.9\left(\frac{d_{AAA,\max}}{2}\right)^{-0.2892}$ with $d_{AAA,\max}$ in mm. They found it more accurate (using FEM as the standard) than law of Laplace and quicker than

a FEM analysis, but it was limited in that it did not work well for highly distorted shapes and does not provide the location of high stress.

2.3.3 Axial Stretch

The in-vivo stretch of the aorta is not frequently quantified in humans; however, it has been well known that when most arteries are cut, both ends will retract as if they were under tension. Han and Fung quantified the axial stretch ratio in the aortas of pigs and dogs. They showed stretch ratios of around 1.2 in the region of the descending aorta and a gradual increase to 1.6 in the lower abdominal region. They also showed that the relative cross-sectional area compared to the average cross-sectional area at a location had an inverse relationship to the stretch ratio [34]. This serves as the foundation for the models considered with stretch ratios varying from 1.0 (none) to 1.6, which should be at least as broad as the physiologic range.

2.4 Anatomic Features of AAA

2.4.1 Wall Motion

Studies have been done to quantify the wall motion experienced by AAA over the cardiac cycle. Vos et al. reported in 2003 on the wall motion before and after treatment with conventional AneuRx (Medtronic AVE) or Talent (World Medical) grafts. Their cinematic magnetic resonance imaging system (cine MRI) was capable of 0.55 mm x 0.55 mm in plane spatial resolution and a 227x280 mm field of view, with 12 cine loops per heartbeat. They used blinded observers for manual tracing of stent-graft contours during peak systole and end diastole at the outside of the aneurysm or stent-graft. They quantified the motion occurring in areas of sharp delineation in the head to

feet, left to right, and anterior-posterior directions. Generally motion vertically was increased after graft treatment by about 0.7 mm. Left to right motion was increased by 0.5 mm from none, and anterior-posterior motion reduced by 1 mm to none. The authors also note that the diseased wall is highly irregular. They also observed stent-graft bend occur with each systole at sites of angulations in 4 of the 7 patients, and in one with significant angulation, there was no motion probably because of calcification and the fibrosis of surrounding tissues [35].

2.4.2 Shape and Rupture

Hans et al. looked to quantify the relationship between thrombus shape and rupture [36]. Examining 2-D slices of CT scans from patients that subsequently ruptured and those that did not showed no definitive link between eccentricity of thrombus and rupture. However, they did see a similar thrombus volume/aneurysm volume ratio in both ruptured and intact AAAs. The thrombus was also usually anterior and eccentric. Their study was limited by looking at only large aneurysms, greater than 5cm and some of the patients with ruptured AAA did not undergo CT scans because of hemodynamic instability, potentially biasing the results.

A larger study was conducted at the Dartmouth-Hitchcock Medical Center to look at the anatomical characteristics of patients with ruptured AAA in contrast with matched controls. They showed a larger diameter in ruptured AAA patients than intact AAA patients, and a diameter of 5mm less for mean diameter of female patients with rupture. Statistical analysis showed a greater risk for patients with mild or no aortic tortuosity, diameter asymmetry (difference greater than 1 cm in major-minor axis), and

current smoking. This study also utilized 2-D CT axial sections. Mild tortuosity was defined as lumen center moves no more than one normal aortic diameter from renal to aortic bifurcation and severe tortuosity meant a vessel makes a nearly right angle from 1 axial section to the next – moderate was the remainder. In a diameter matched comparison, they showed rupture was more likely in current smokers, history of hypertension, and aneurysm cross-sectional diameter asymmetry. Rupture location was posteriolateral or lateral in the large majority of patients in which the location could be identified. Anterior or anteriolateral rupture was identified in 11% of patients with identifiable rupture location. The diameter asymmetry calculation was done at the point of maximal diameter and no 3-D reconstructions were part of the study other than to show how 2-D studies are limited [37].

Rupture location has also been associated with survivability, a ruptured anteriolateral wall is associated with sudden death, whereas a posteriolateral wall rupture can survive to hospitalization [38]. The reason is that the space into which a posteriolateral rupture occurs can restrict blood loss by containment whereas the anteriolateral rupture bleeds freely into a larger space.

2.4.3 Contact

There are several structures near the abdominal aorta which may influence its growth and susceptibility to rupture. The vena cava runs alongside the aorta, and the spine is behind it. There are also lumbar arteries, as well as the celiac, hypgogastric, and mesenteric arteries coming off the aorta in this region. These additional arteries are bypassed by implantation of an endograft and may allow blood flow into and out of the

aneurysm sac after excluding aortic flow – resulting in a type II endoleak. Endoleaks are described further in section 2.5.2.

2.4.4 Neck Growth and Remodeling

Aneurysm neck is the proximal portion of an AAA located between significant expansion and the renal arteries. Aneurysm neck growth following treatment is an area of concern for vascular specialists. The proximal seal could be affected by changes in the diameter of the aneurysm neck. A study by Badran et al. looked retrospectively at the changes in diameter after endovascular repair. Measurements of the outer neck diameter were made at 7.5mm below the lowermost renal artery using only axial images. Their work showed an intraobserver error of 2 mm, and changes in diameter from a pre-op baseline of 21.8 mm to 22.8 mm within 60 days post-op to 25.8 mm at latest follow-up. This change meant that the original stent-graft over sizing of 2.9 mm was reduced to 0.7 mm. Neck diameter increased in 84% of their patients. Their group's baseline over sizing was 13.7% was influenced by some cases of under sizing in their early experience and their current practice is to aim for 20% over sizing. Their results also raise the possibility that neck dilation may be exacerbated by greater degrees of stent-graft over sizing. Their results were confounded by the variety of grafts and corresponding radial force used, but showed that aneurysm neck dilation generally reaches a maximum in the first 2 years of follow-up [39].

2.5 Treatment Options

2.5.1 Open Repair

The two primary methods of treatment for AAAs are the open repair procedure and endograft placement. The open repair procedure is highly invasive and induces great trauma, as it involves gaining access to the exterior of the aorta, clamping off the dilated portion, cleaning up the interior/removing thrombus, and sewing in a graft made of Dacron or another material in order to provide a new lumen for flow. The remaining material, minus excess, is closed around the repair. There is a recovery period of approximately 10 days in intensive care. The risks include those associated with general surgery, e.g. infection and issues with anesthesia as well as the possibility of affecting the gut and reproductive blood supply [40]. These risks are sometimes considered to be so great that patients or doctors refuse the procedure as it is seen to not be in the patient's best interest/quality of life. Open repair is, however, a highly reliable treatment when surgery is successful – matching 2^{nd} year risk with endovascular repair [41].

2.5.2 Endovascular Repair

Generally, in endograft placement, a much less invasive procedure, incisions are made along the groin to access the femoral arteries. A guidewire is steered up to into the aorta past the renal arteries with aid from fluoroscopy. The deployment system of the endograft is passed over the guidewire into position both vertically and rotationally. The endograft is then released from its deployment system. Another guidewire is steered up the other femoral artery and positioned so that the contralateral leg of the endograft can be deployed. After deployment of the second leg, molding balloon inflations may be

used to ensure complete apposition of the graft at both the neck and legs – and potentially the connection joint between main body and contralateral leg as well. The Powerlink device (Endologix) being the exception to the general rule, as it requires only access from one side to deploy because its branch sits on the bifurcation, making it more technically difficult to use. The patient typically spends a day or two in intensive care before being released. The endograft procedure has potential risks associated with the anesthesia (patient is not usually unconscious) and surgical risk of damaging other internal structures.

The open procedure has a 30-day operative mortality of ~5%, whereas the operative mortality of the endograft procedure has a lower mortality of ~2%. The differences in long term survival are smaller, as the durability of the open procedure is much better. Also, the endograft is restricted to use in patients with acceptable geometry (adequate contact areas for the proximal and distal ends of the endograft) [42]. Cotroneo et al. analyzed the eligibility of patients with AAA for repair – looking at 182 consecutive patients identified with AAA. They found 39.3%, of the 130 patients needing treatment, eligible for EVAR. The exclusions were primarily caused by bad neck geometry (41 of 79). Specifically, the length of the neck was too short (< 1.5 cm), diameter too large (> 30 mm) or too tortuous (< 120º) [43]. These limitations reflect technical limitations of the device in attachment and deployment. Because the endograft procedure is less invasive and the surgery less traumatic, it can be used in patients with significant co-morbidities or contraindications for the open procedure (as it was in the Cotroneo et al. series for large sac diameters and shortened necks [43]), though the 4

year survival rate is not significantly improved between endograft treated and untreated patients in these high risk patients. The increased durability of the open procedure requires less postoperative monitoring than the endograft procedure. The endograft procedure has been shown to be generally effective but not without limitations or risk of complications [42]. The classification of endoleaks (flow around the graft) and the classification of endotension (apparent continued pressurization of the aneurysm sac) types are shown in Table 1 which is adapted from Veith et al. [44] and Chaikof et al. [45].

Table 1. Endoleak and endotension types.

Endoleaks (type)	Description Source of perigraft flow
I	Attachment site leaks
A	Proximal end of endograft
B	Distal end of endograft
C	Iliac occluder plug
II	Branch leaks (without attachment site connection
A	Simple or to-and-fro (from only 1 patent branch)
B	Complex or flow-through (with 2 or more patent branches)
III	Graft defect
A	Junction leak or modular disconnect
B	Fabric disruption (midgraft hole) Minor (< 2mm; e.g., suture holes) Major (≥ 2mm)
IV	Graft wall (fabric) porosity (< 30 days after graft placement)
Endotension Type	
A	With no endoleak
B	With sealed endoleak (virtual endoleak)
C	With type I or type III leak
D	With type II leak

3. ANEURYSM WALL AND THROMBUS MATERIAL PROPERTIES

3.1 The Basics

The material properties of the aneurysm wall and thrombus are essential in the mechanical modeling of AAA. Although the focal enlargement of aortic diameter defines abdominal aortic aneurysms, the aorta undergoes a change in wall properties and has been shown to have decreased elastin content [46].

3.1.1 Aneurysm Expansion

The rate of aortic expansion, as defined by maximum diameter, is related to the mechanical properties. The expansion has been quantified through ultrasound studies. One indicated that the rate of diameter increase is proportional to the diameter of the aneurysm [47]. However, another, more comprehensive study by Brady et al. showed that diameter increase was dependent on initial diameter but also on diabetes (inhibiting) and smoking (promoting). Their study showed a mean growth of 2.6 mm/yr, yet the variation within the raw growth data indicated that some aneurysm showed linear growth whereas others showed step-wise growth spurts and stasis periods [48]. Another study by Love et al. in 2005 indicated that a high degree of mural calcification is associated with failure of sac shrinkage after EVAR [49]. The rate and onset of diameter AAA growth is clearly patient dependent and may be associated to factors such as age and age of onset, which are reflective of underlying aneurysm etiology.

3.1.2 Aneurysm Constituents

The typical constituents of AAA include the wall itself, calcifications, and thrombus. Each constituent varies in thickness between patients and within the same patient; thrombus and calcification may be present to varying degrees.

Thickness measurements on the wall have varied, but typically fall within 1.5 to 2.0 mm. Thubrikar et al. measured thickness of unpressurized autopsy specimens by micrometer in conjunction with a resistance circuit and found some regional variation – anterior 2.09 +/- 0.51 mm, lateral 2.52 +/- 0.67 mm, and posterior 2.73 +/- 0.46 mm [50]. By contrast, Raghavan et al. found thickness to vary from 0.23 mm at a rupture site to 4.26 mm at a calcified site within 4 AAA from autopsy, with a median value of 1.48 with 5^{th} percentile of 0.80 and 95^{th} percentile of 2.83 mm. They also report a different regional variation than Thubrikar et al., with posterior and regions slightly thinner than the anterior and left regions. Additionally, it was reported that the proximal neck had greater thickness than the aneurysm regions. Also noteworthy, the calcified plaque regions were the thickest, 92% greater than 2mm thick – when present [51].

The typically hard flat plating structures of calcifications grow and accumulate along the aneurysm wall and are much more rigid than the wall or ILT. In a study of just calcifications, Marra et al. reported that the pieces were up to 8 mm in largest dimension with thicknesses ranging from 0.7 to 2.0 mm in a sample of 12 calcifications from 12 patients [52].

Thrombus thickness has been associated with rupture due to a report from Satta et al, which showed a greater endoluminal thrombus thickness (3.5 cm) in ruptured than

symptomatic aneurysms (2.0 cm) [53]. The study by Marra also referred to a study by Pillari et al. that indicated some thrombus was present in all cases of a 55 patient study [52].

3.1.3 Experimental Methods for Determining Properties

Material properties can be ascertained using a variety of experiments, but the methods most commonly employed for AAA tissue are uniaxial and biaxial tension tests using longitudinal/circumferential strips cut from the wall. These tests are typically conducted on either superfluous tissue from subjects having undergone open repair or on autopsy tissue with age matched tissue donors/cadavers used as controls [9, 54]. The tests are typically carried out, after preconditioning, at low strain rates to failure so that both stress-strain relations and failure strength can be determined.

3.1.4 Material Properties of Aneurysm Constituents

Experiments by Raghavan and Vorp reported in 2000 indicated a strain energy function for aneurysm wall tissue of $W = \alpha(I_B - 3) + \beta(I_B - 3)^2$, with $\alpha = 17.2$ N/cm^2 (172 kPa) and $\beta = 188.1$ N/cm^2 (1881 kPa). These fits were good to nearly a 1.2 stretch ratio and a load of 100 N/cm^2 (1000 kPa). These results also showed no significant difference in α or β between longitudinal and circumferential groups [8].

Experiments by Wang et al. on thrombus indicated a strain energy function: $W = C_1(II_B - 3) + C_2(II_B - 3)^2$, with $C_1 = C_2 = 2.6$ N/cm^2 on average. Again, they saw no statistical difference between directions, but did see a trend. They also report their values in terms of the layer of thrombus, as the medial layer is less stiff than the luminal layer [9].

3.1.5 Computational Models of Aneurysms

These properties were subsequently used in studies analyzing the sensitivity of stress analyses to them. These studies showed that population values were adequate for predicting peak stress to within 5% in asymmetric models. These material models were also used to estimate stresses within the wall for different patients, which highlighted the protective role thrombus can have, at least when considering it homogenously [55]. Modeling has continued to develop and advance, providing consideration of more complex properties for stiffness/strain energy and for strength.

3.2 The Details

Mechanical properties of the aortic wall are useful for calculating equilibrium position and when rupture will occur. The relationship between wall stress and wall strain allows determination of the equilibrium position of the wall under applied load. When wall stress exceeds wall strength, rupture results as the material fails to support the load. Also, because the wall is a living tissue its properties can change as a result of the tissue's load and material history [56]. There are also variations in properties associated with smoking, age, gender, and family history differences [57].

3.3 Aneurysm Morphology

The shape and structure of the abdominal aortic aneurysm is useful from a variety of standpoints. Currently, diameter threshold is a common consideration for surgery. However, due to the risk of surgery, patient-specific modeling that accounts for a patient's parameters is being advanced as a more precise means of predicting rupture risk.

3.3.1 Wall

The wall of the aneurysm is a distended and modified version of the aorta. The wall of the aorta, as with any major artery, is composed of layers including an intima, media, and adventitia. The intima is comprised of a monolayer of endothelial cells on a basement membrane. The media consists of smooth muscle cells which can control the tone of the vessel. The adventitia consists primarily of extracellular matrix and fibroblasts, providing the outer retaining sheath. However, this is a simplistic view of the actual aorta in the typical patient with AAA. The patient that typically gets an AAA also has atherosclerosis and other irregularities in their aorta.

3.3.2 Blebs

A paper by Hunter et al. analyzed the presence of blebs – focal outcroppings of the wall and showed them to be present in 10% of aneurysms. Immunohistochemistry on samples removed at resection indicated these blebs had lymphocytic infiltrate and elastic tissue attenuation [58].

3.3.3 Thrombus

The thrombus, which typically lines the dilated segment of the aorta in AAA, contains a mixture of blood cells, platelets, blood proteins, and cellular debris in a fibrin structure. Gross observation showed 3 layers, differentiable by location and color. Newer thrombus located luminally was red and older thrombus located medially was white, whereas abluminal thrombus located closest to the wall was brown. SEM further indicated that the different layers had different underlying structures with degenerate

fibers in the abluminal region, some degeneration in the medial layer, and thick fibrin bundles with secondary linking structures in the luminal layer [9].

3.3.4 Calcifications

In addition to the paper indicating that calcification inhibited aneurysm reduction after EVAR, another paper associated greater calcification with aneurysm stability prior to treatment. In a Danish study on small aneurysms, the cross-section of the CT at maximum diameter was judged to be more or less than 50% of the circumference calcified. About half (51%) had greater than 50% calcification and these had a growth rate of 1.72 mm/year compared to 2.97 mm/year in the remaining group [59].

3.4 Experimental Methods

The material properties of abdominal aortic aneurysm and components have been studied by mechanical experiments to determine material properties. These experiments included both uniaxial and biaxial extension testing as well as compression tests. Important considerations when conducting experiments are the rate of the test, preconditioning, material sourcing, tissue preparation, and storage.

3.4.1 Uniaxial Testing

Uniaxial extension testing consists of strips of tissue held in clamps then pulled apart. The testing can show the relationship between components of stress and strain, direction preference, and failure stress/strain.

A 1996 paper by Raghavan et al. detailed experiments on tissue from surgical repair. The segments were 4-7 cm in length, at least 1 cm wide, and oriented either circumferentially or longitudinally. The control segments were from the remnants of

infrarenal aorta following kidney transplant. Samples were refrigerated for less than 24 hours at 4C, and then tested at room temperature. They used preconditioning of 10 cycles at 8.5% strain per minute to 7% strain. Then the samples were stretched to failure at the same rate, only recording samples failing away from clamps. Lower yield stress in AAA than in normal (longitudinal and circumferential) was found (65.2, 70.7 N/cm^2 vs. 121 N/cm^2) [54]. This testing covered a larger strain range than He and Roach [46].

Another example can be found in Wang et al. describing thrombus testing. The samples of thrombus were removed intact from AAA, peeled into layers of ~0.6 mm thickness for uniaxial tensile testing, and then sliced into dimensions of approximately 10 x 2 mm. The preconditioning was done for 10 cycles to 10 percent strain at a rate of 0.08 %/second. The mechanical testing was only for a portion of the thrombus as the layers nearest the wall were too degenerated [9].

3.4.2 Biaxial Tensile Testing

Biaxial testing has been shown to better indicate differences between material directions within aneurysmal tissue. In testing on aortic wall tissue, Vande Geest et al. the effects, found an increase in circumferential stiffness for AAA tissue compared to age matched aortic aneurysm tissue. Their study utilized square (2.0 cm by 2.0 cm) obtained from anterior portion of aneurysm undergoing open surgical repair or autopsy for controls. The testing of the never frozen tissue (stored at 4C) was done to a maximum tension of 120 N/m and data from the 10^{th} loading cycle recorded, controlling both axes at once to control relative stretch [60].

Another biaxial test was conducted on thrombus and indicated a lack of orthotropy [61]. The procedure was similar to that used by in the aortic testing by the same group [60], though the maximum tension was only 40 N/m as preliminary testing indicated that was the maximum tolerated without attachment of loads pulling out. These experiments indicated no difference between directions, as the uniaxial tests had, but did result in different values. These were attributed to the test method constraining the samples more.

3.4.3 Pressurization

Pressurization testing has been conducted on aortic samples to provide a means of quantifying the global response of the tissue. Tests by Ohashi et al. on porcine thoracic aortas inflated circles of tissue into hemispheres and calculated mean breaking stress. They found in the distal samples a mean breaking pressure of 2.3 +/- 0.8 MPa for distal pressurization and contrasted that with uniaxial tension results of 2.0 +/- 0.7 MPa for longitudinal samples and 3.3 +/- 0.6 MPa for circumferential samples (only circumferential statistically different from pressurization results) [62].

A non-invasive quantification of aortic stiffness was done by using in vivo pressurization information from blood pressure and ultrasound measurements of the maximum external diameter 4 cm distal to superior mesenteric artery. They showed an increase in pressure-strain elastic modulus (defined as Ep = (Ps-Pd) [Dd/ (Ds-Dd)]) from 14.0 N/cm^2 in the elderly control group to 31.3 N/cm^2 in the aneurysm group. They did show wide variability in their results between patients and within groupings [63].

3.4.4 Nanoindentation

Marra et al. used nanonindentation (unconfined compression) to measure the properties of calcifications because the calcification samples were so small. The indenting area was 3 μm^2. Their system applied a maximum of 1500 μN at a rate of 60 μN/sec to samples, either parallel or perpendicular to the thickness direction [52].

3.4.5 General Experimental Considerations

Curve fitting the data from experiments is problematic and two primary methods (phenomenological and microstructure based) have been used to identify what underlying curve type to fit. The phenomenological approached was used in the 2000 Raghavan and Vorp paper to get $W = \alpha(I_B - 3) + \beta(I_B - 3)^2$ [8]. The microstructure based approach was used in a Raghavan et al. paper to incorporate the recruitment of fibers into a model of 1-D behavior [54].

The underlying structure of the aneurysm is complex with many layers and constituents so experiments must address homogeneity, isotropy, and variability.

3.5 Published Mechanical Properties

3.5.1 Aortic Wall

Early papers in field used linear elastic material properties, with some relying on the justification that, over the range of pressures experienced in vivo, the tissue response is nearly linear and cited the work of MacDonald 1974 [64]. The paper by Thubrikar [65] used a Young's modulus of 4.66 N/mm^2 with a Poisson's ratio of 0.49 in analyzing a model based on one patient. Work done by Vorp et al [66] used a modulus of 500 N/cm^2 (5.00 N/mm^2) with a Poisson's ratio of 0.49 in analyzing axisymmetric models.

Isotropic wall properties have been published by Raghavan and Vorp 2000 for the $W = \alpha(I_B - 3) + \beta(I_B - 3)^2$ strain energy function. The mean values reported were 174 kPa and 1881 kPa. They found no significant difference in alpha or beta between longitudinal and circumferential groups [8].

Anisotropy has been investigated and a biaxial response function proposed by Vande Geest et al. to model the results of experiments they conducted which showed aneurysmal degeneration is associated with an increase in mechanical anisotropy, with the circumferential direction preferentially stiffening [60]. The resulting SEDF:

$W = b_0\left(e^{\frac{1}{2}b_1 E_{\theta\theta}^2} + e^{\frac{1}{2}b_2 E_{LL}^2} + e^{b_3 E_{\theta\theta} E_{LL}} + e^{\frac{1}{2}b_4 E_{\theta L}^2} + e^{b_5 E_{\theta\theta} E_{\theta L}} + e^{b_6 E_{\theta\theta} E_{\theta L}} - 6 \right)$ with $b_0 = 0.14$, $b_1 =$ 477.0, $b_2 = 416.4$, $b_3 = 408.3$ kPa, and shear constants = 10 kPa was utilized in subsequent analysis of patient-specific aneurysms [67].

Very recent work incorporates anisotropy [68], and uses more material parameters. $\Psi(C, a_0, b_0,) = U(J) + \overline{\Psi}(\bar{I}_1, \bar{I}_2, \bar{I}_4, ..., \bar{I}_8)$ The invariants are defined in terms of C, a_0, and b_0. The dependency on the invariants varies between proposed isotropic and anisotropic constitutive relations. The isotropic form: $\Psi = U(J) + \frac{C_1}{C_2}[e^{C_2/2(\bar{I}_1 - 3)} - 1]$, with constants $C_1 = 1.04$ kPa and $C_2 = 280.04$ kPa.

The anisotropic form:

$\Psi = U(J) + C_1(\overline{I_1} - 3) + \frac{k_1}{2k_2}\{e^{k_2[(1-\rho)(\bar{I}_1 - 3)^2 + \rho(\bar{I}_4 - \bar{I}_4^0)^2]} - 1\} + \frac{k_3}{2k_4}\{e^{k_4[(1-\rho)(\bar{I}_1 - 3)^2 + \rho(\bar{I}_6 - \bar{I}_6^0)^2]} - 1\}$

, with constants $C_1 = 0.12$, $k_1 = k_3 = 244.90$ kPa, $k_2 = k_4 = 1576.20$, $\rho = 0.14$, and $\phi = 5.0$ deg. The values for these constants were based on an experimental study by Vande

Geest et al. [60]. The work by Rodriguez et al. also indicates that though anisotropy results in higher stress values, these values do scale linearly to isotropic model results over their axisymmetric model [68].

The strength of the wall has also been studied because it has been noted to change with aneurysm progression and between patients. Work by Vande Geest et al. [69] using multiple linear regression and mixed modeling techniques arrived at an equation defining local wall strength using parameters measurable noninvasively and cost effectively.

$$STRENGTH = 72.9 - 33.5 * (ILT^{1/2} - 0.79) - 12.3 * (NORD - 2.31) - 24 * HIST + 15 * SEX$$

In this equation, the units are N/cm^2 for strength, cm for ILT – intraluminal thrombus thickness, dimensionless for the local normalized diameter NORD, and dimensionless binary variables HIST and SEX. The binary variable HIST has a value of ½ for positive family history and -1/2 for no family history. The binary variable SEX is ½ for males, -½ for females. This equation was used for the calculation of an RPI, rupture prediction index, which is equal to stress divided by strength for each location of the wall. Alternately, in another paper by the mostly the same group, determined based upon 38 patients and 81 samples an equation with the following constants.

$$STRENGTH = 71.9 - 37.9 * (ILT^{1/2} - 0.81) - 15.6 * (NORD - 2.46) - 21.3 * HIST + 19.3 * SEX$$

It is noteworthy, that for the worst case scenario, female with family history, large ILT, and NORD =3.9, the model predicts a negative strength – though there was no patient with this combination of features. Also interesting was that their methods showed that age and smoking had insignificant effects on strength [57].

The 2006 paper by Raghavan et al. tested samples from two blisters or blebs. They found a T_f of approximately 6 N/cm, which was on the low end (median 14.8 N/cm) of the range observed over the samples taken from throughout the four aneurysms studied (obtained by autopsy).

3.5.2 Thrombus

Due to the degenerated nature of the layer nearest the aortic wall, they tested only the luminal and medial regions – fitting the results to a strain energy function of the form: $W = C_1(I_2 - 3) + C_2(I_2 - 3)^2$. Significant differences were found between luminal and medial samples, but not between longitudinal and circumferential directions. Depending on how constants averaged (considering all values tested or with equal size representative groups), values in the neighborhood of $C_1 = 3$ N/cm^2= C_2 for the luminal, and for medial more like $C_1 = 2.1$, $C_2 = 2.2$ N/cm^2 were found. An overall average on the order of 2.6 N/cm^2 was found for C_1 and C_2 [9]. The table below summarizes the values.

Table 2. Thrombus constants

Sample Source	C_1 (N/cm^2)	C_2 (N/cm^2)
Luminal, longitudinal	2.89 +/-0.39	3.10 +/- 0.45
Luminal, circumferential	3.19 +/- 0.45	2.93 +/- 0.36
Medial, longitudinal	2.06 +/- 0.33	1.77 +/- 0.28
Medial, circumferential	2.21 +/- 0.48	2.57 +/- 0.43

A linearization of the Vorp model by Hinnen et al. [70] found an elastic/Young's modulus (E) of about 50 kPa, which is at the high end of what the Hinnen experiments

estimated over a frequency range of 0.8 to 3.9Hz, with little change in variability (which was quite wide ~15 to 60 kPa). Their average E was about 38 kPa. This group also tested incompressibility and found a Poisson's ratio to be close to 0.5.

3.5.3 Calcifications

The Marra et al. paper found an average modulus of 24.4 GPa for calcification samples oriented perpendicular to thickness and 21.0 GPa for samples parallel. The tests showed wide variation (13.7 to 35.1 GPa) over the 8 samples tested, though this variation is all at 3 orders of magnitude stiffer than AAA wall tissue. The authors assumed a Poisson ratio of 0.27 as measured by Grenoble et al. for mineral hydroxyapatite [52]. A very recent paper used a Mooney-Rivlin model, with constants A=18,804.5 Pa and B=20, which had been previously used in a study of plaque calcification [71].

3.6 Other Computational Results

3.6.1 Patient-specific

The results of experiments have been used in axisymmetric and patient-specific analyses to better understand aneurysm risk and development. In a review of aneurysm repair mechanics, Raghavan et al. noted patient-specific models reported that stress is distributed non-uniformly, with peak values on the order of 35 N/cm^2 with a range from 25 to 75 N/cm^2. They noted that posterior wall tends to be the region with high stress although the bulge is predominantly anterior. They also suggest that there is an actionable level of stress at 44 N/cm^2 at which point watchful waiting is no longer wise and suggest the average aneurysm is likely to start tearing at 65 N/cm^2. They note also

that turbulent blood flow results in slight increase (6 mmHg) in pressure at distal end and increases shear stresses by about 10 x 10^{-4} N/cm^2 (100 dynes/cm^2) [26].

Raghavan and Vorp showed that patient-specificity in parameters of the strain energy function was not necessary – the population mean is adequate [8]. The strain energy function with parameters alpha and beta was subsequently utilized in the paper by Fillinger et al. 2003 to show that wall stress correlates with rupture risk [7].

3.6.2 Idealized Shapes

The effect of varying these experimentally determined constants of thrombus was investigated [72]. This study showed that over the range of values determined by experiment, it did not make more than a 5% difference in an idealized model of AAA. The study concluded that patient-specific values do not need to be used for thrombus; rather population mean values should be sufficient.

4. ENDOGRAFT MATERIAL PROPERTIES

An important component of modeling the endograft/tissue interaction is an appropriate representation of the endograft material properties, including differences in behaviors in compression versus tension. The endograft typically consists of fabric and a reinforcing metallic structure that may be attached using suture or by another method. Depending on the device, the precise properties and response to mechanical loads can differ. Inflation and compression experiments on endografts were conducted to measure these properties. This section describes the experiment and results of measuring endografts for mechanical properties as well as the limitations of the experiment and analysis.

4.1 Endograft Background

Material properties of the endograft were necessary for modeling the material within the finite element framework. The design of the endograft resulted in a marked difference in circumferential expansion and compression response due to its combination of two materials. Prior published work on the endograft properties focused on the response of the bare metal stents that make up the backbone of the graft [73].

4.1.1 Published properties

To address the gap in the published literature on endograft material properties, experiments were necessary. Filling the gap was essential for modeling them as part of the treated aneurysm models. Prior work incorporating grafts into models, instead of detailing tests to find material properties, used an arbitrary but generally reasonable linear elastic modulus, such as 100 MPa with a Poisson ratio of 0.35 [74]. Another study

used 10 MPa and cited another work as the experimental source – though the experimental source did not calculate a modulus [75]

4.1.2 Approved Devices

There were four endografts/stent grafts currently approved by the Food and Drug Administration (FDA) for usage in the USA as of August 2008; these fell under the "MIH" product code with the classification of "System, Endovascular Graft, Aortic Aneurysm Treatment". The four products currently listed were the AneuRx Stent Graft System from Medtronic Vascular, Excluder Bifurcated Endoprosthesis from W. L. Gore & Associates, Inc., Powerlink System from Endologix, Inc., and Zenith AAA Endovascular Graft from Cook, Inc. All of these devices were class III medical devices and as such required premarket approval and general controls. Class III devices underwent the highest level of scrutiny from the FDA. There was also a consensus standard for their development – ASTM F2129-04 – "Test method for conducting cyclic potentiodynamic polarization measurements to determine the corrosion susceptibility of small implant devices". The testing of graft designs was also covered by the ISO standard 25539-1:2003, amended 2005. The ASTM standard was broadly applicable to implantable medical devices and geared toward evaluating material biocompatibility, not directly evaluating their ability to function correctly in patients. The ISO standard provided instructions for testing various attributes of the device. To address the fundamental issue of efficacy, the device developers conducted animal studies and clinical trials prior to FDA approval.

The designs of the approved endografts are generally similar, incorporating metal stent(s) and fabric components. The endografts differed in the shape, composition, and assembly of their components [76].

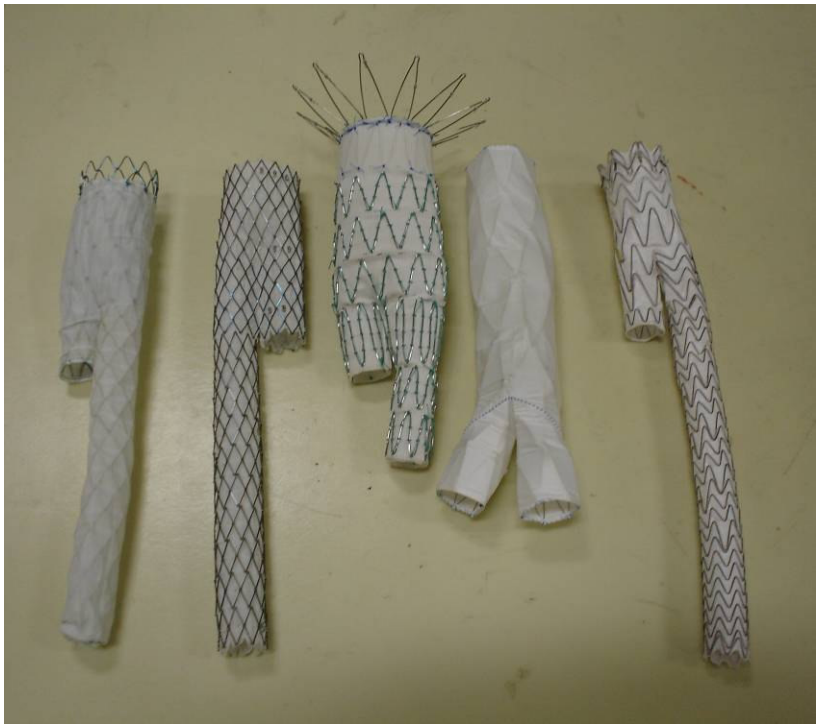

Figure 2. Endograft designs tested included, from left to right: Boston Scientific Vanguard, Medtronic AneuRx, Cook Zenith, Endologix Powerlink, and Gore Excluder.

4.2 Methods of Endograft Experiments

Three of the approved devices were tested for material/mechanical properties. The set of circumferential compression and tension tests were done by the cuff method described by Fallone et al. [77] and by balloon inflation within the tube.

4.2.1 Compression Tests

Briefly, for the compression tests, a cuff made from paper, that was nearly inextensible over the range of loads used, was wrapped around the endograft leg (and through itself). The top end was hung via binder clip from a spring scale that was fixed in a table-mounted clamp. The low end was loaded by hanging weights (Fisher Scientific) from a binder clip. At each load, the position of the pass-through on the cuff was marked. The resulting circumference and force were recorded over a range of loads from 5g to 250g. The cuff dimensions varied and were between 14 and 18.31 mm wide, and 0.11 mm in thickness. See Figure 3 for a picture of the test method for compression.

Figure 3. Picture showing the system used for loading the endograft with external pressure by a collar with dead weights. Binder clips provide means of connection to collar.

4.2.2 Inflation Tests

The balloon inflation method used to test circumferential tension employed balloons similar to those used for the expansion of endografts to ensure their apposition in vivo. The balloon catheter was connected to a syringe and T joint, which allowed for pressurization of the balloon with water and pressure measurement via catheter. Pressure measurements were conducted using a Millar pressure transducer catheter connected to LabVIEW. A custom LabVIEW program converted the voltage from the catheter to a display of pressure (mmHg). The Equalizer Balloon Catheter (EQL/40/7/2/100) from Boston Scientific was used as was a CODA Balloon Catheter (CODA-10.0-25-100-32) from Cook, Inc. The inflation required a second person or caulk-gun due to the amount of force required to hold a given pressure with the syringe. The catheter-syringe-balloon-endograft system was level to minimize pressure variation. Diameters were measured externally using a digital caliper and recorded with pressure readings. The compression test was done four times and the extension test six times. Data from both tests were converted into stress and strain components using the methods of Agrawal as if they were from uniaxial tests [78]. The circumferential components were plotted against each other and a least squares fit was performed with the stipulation that the fit must pass through the origin. See Figure 4 for a schematic diagram of the test method. Figure 5 and Figure 6 show the inflation test in pictures.

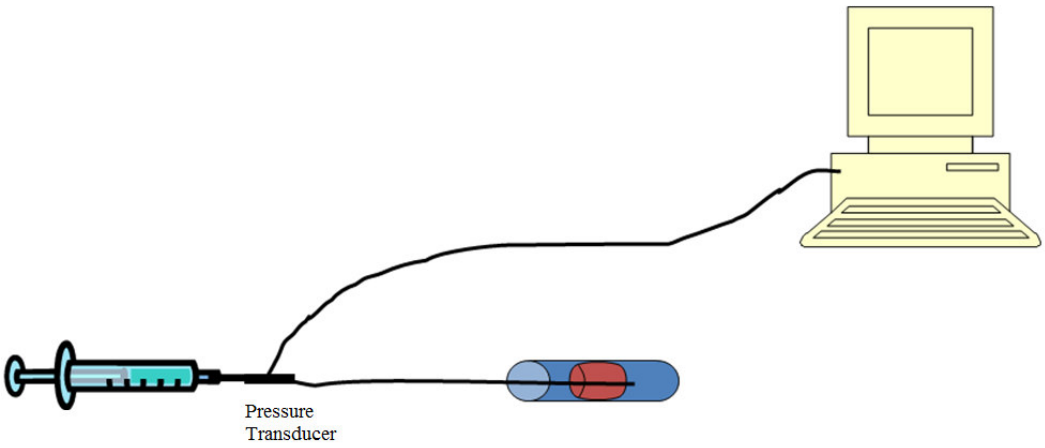

Figure 4. Schematic diagram of inflation test shows computer, syringe for balloon inflation, and balloon inside endograft. Balloon external diameter measured with calipers.

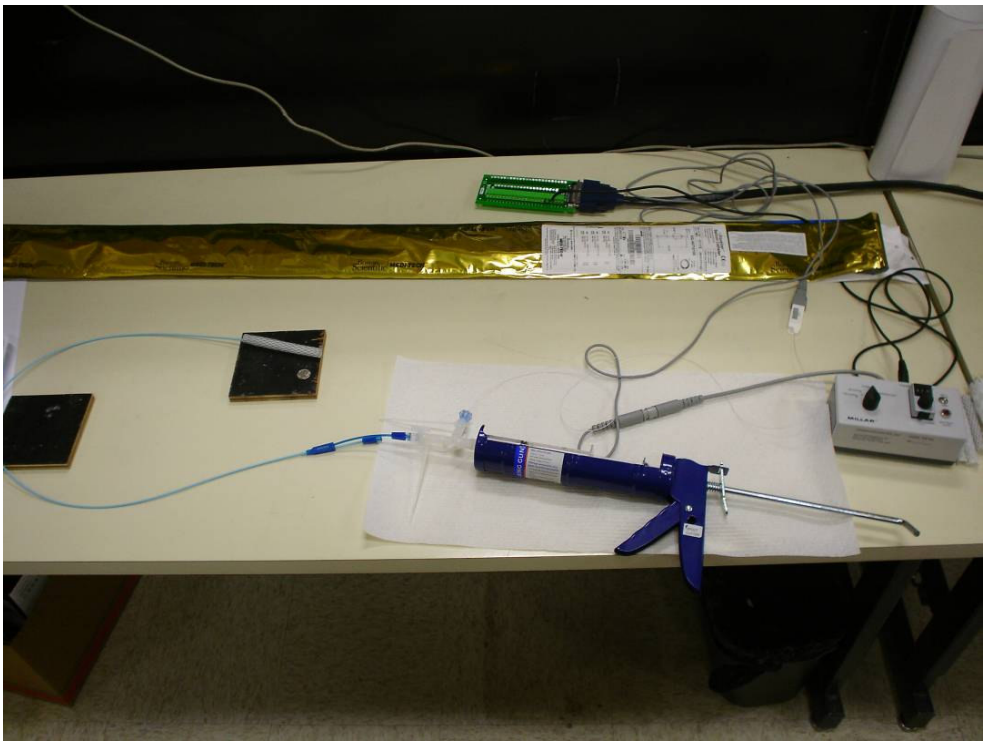

Figure 5. Picture of system used for loading grafts.

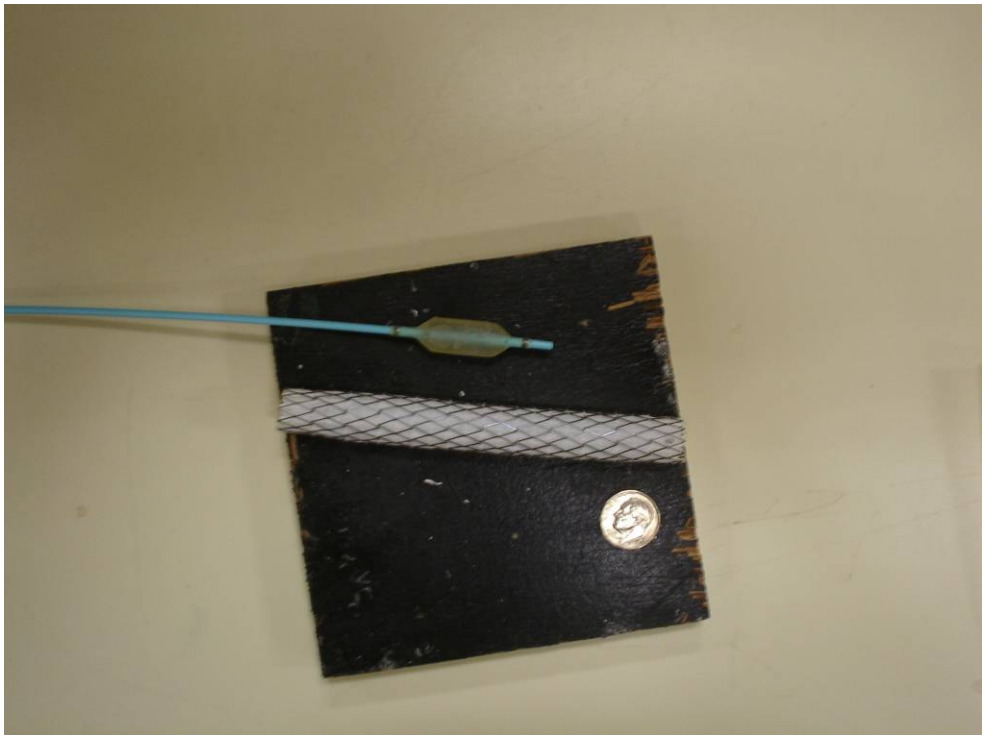

Figure 6. Picture showing partially inflated inflation balloon, stent graft leg, and a dime for scale.

4.2.3 Fitting Stress-Strain Curves

Computational fits of stress-strain curves were done by least squares regression, with the intercept specified as zero to ensure that the no load state was indeed unloaded in the fit. Fit evaluation was conducted by looking at the goodness of fit and evaluation of the R^2 value for predictive capability. Additionally, thicknesses of the grafts were measured by digital caliper.

4.2.4 Validation via FEM Implementation

Once graft parameters were determined, these values were used in finite element model a cube and a tube. The cube, subjected to uniaxial tension and compression

loading conditions, was used to determine if the moduli could indeed be applied differently within the same model. The tube model was used to confirm that the moduli showed good agreement between experiment and model of experiment. The boundary conditions were those necessary to prevent rigid body motion, but nothing beyond that so that the model was not over-constrained. Also, the Poisson's ratio, ν, had to be assumed 0.3 (same as stainless steel) because no shear tests were conducted to estimate it from experiment. Using 0.5 would have resulted in an incompressible structure, tying the graft length changes fully to the circumferential strain.

4.3 Results of Endograft Experiments

The results for the compression and extension tests are given in Figure 7, Figure 8, and Figure 9. The figure shows the linear fits and constants for modulus to vary between 10 MPa and 20 MPa for tension and 1 MPa and 5 MPa for compression. The figure also shows the variation between each experiment. Compression is on the left part of each graph with negative strains and negative stresses.

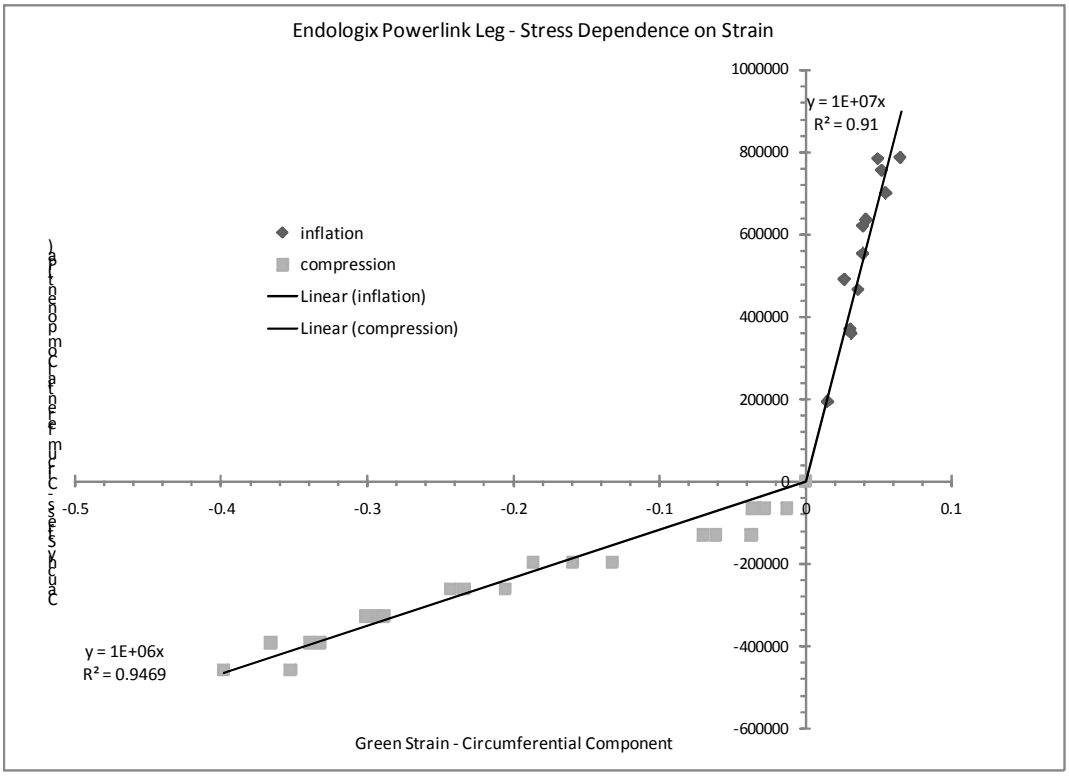

Figure 7. Plot of circumferential stress (Pa) and strain component from endograft testing for Powerlink graft showing linear fit to data.

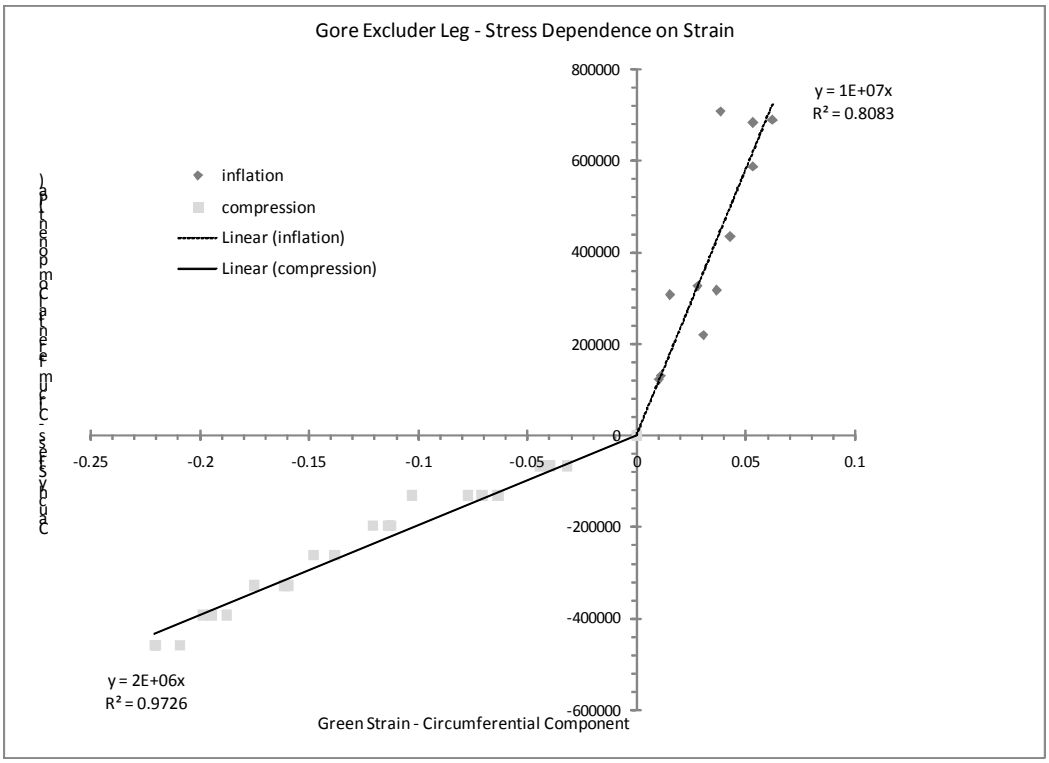

Figure 8. Plot of circumferential stress (Pa) and strain component from endograft testing for Excluder graft showing linear fit to data

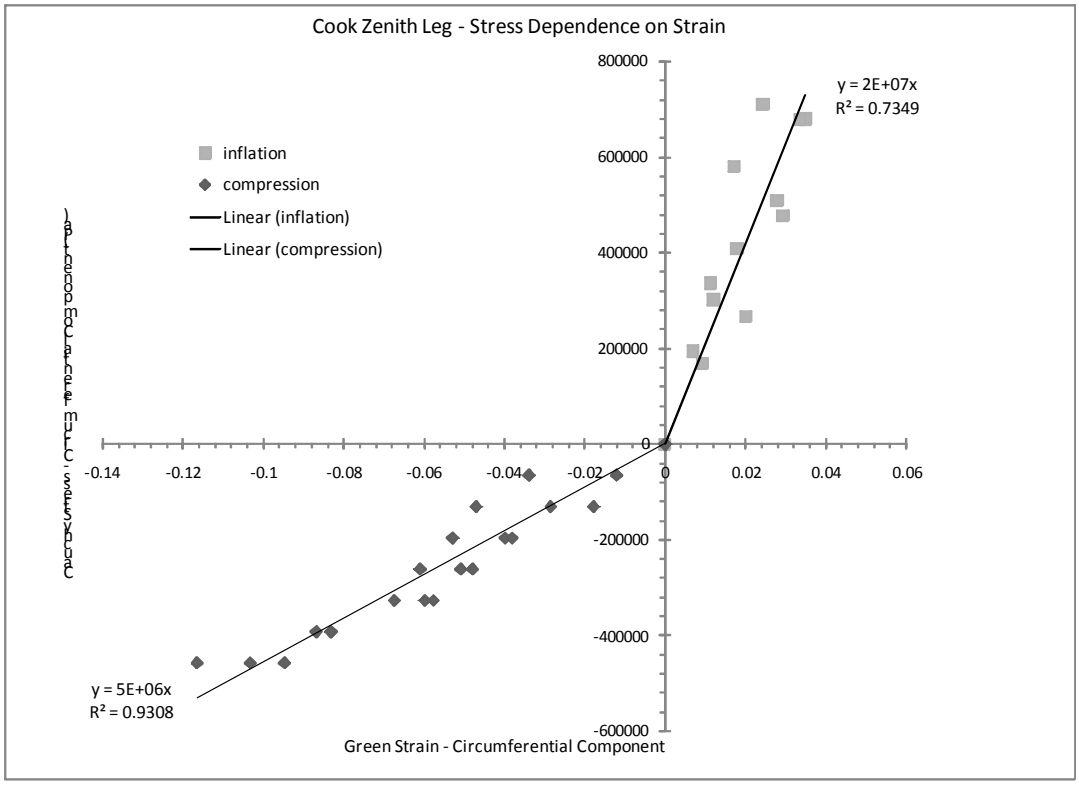

Figure 9. Plot of circumferential stress (Pa) and strain component from endograft testing for Zenith graft showing linear fit to data.

The data show substantial variation, particularly in tension. This variation seems to be primarily due to the sharp transition in the material between slight expansion and rigid response to increased pressure. Also notable is that the pressures required to get significant circumferential strains are quite high. Note that the fabric only substantially resists dilation as it buckles easily during compression; in contrast, the nitinol stent structures resist both tension and compression.

The Zenith graft is nearly twice as stiff in both compression and tension as the other endografts tested. Measurements indicate it to be thicker than the other endografts (2 mm vs. 1 mm). Measuring the thickness proved to be difficult because of the multi-component nature of the devices including suture, graft, and fabric resulted in uneven surfaces.

4.3.1 Bilinear FEM Model

Confirmation that the material behavior could be modeled accurately was necessary to ensure that the complicated properties could be appropriately represented using the same FEM tools as were used for the rest of the modeling. A figure showing the stress strain response of the cylinder model is shown below in Figure 10.

Varying the Poisson ratio between 0.25 and 0.4 had no significant impact on stresses under the tube models. This finding is unsurprising given the relative lack of shear loading on the tube.

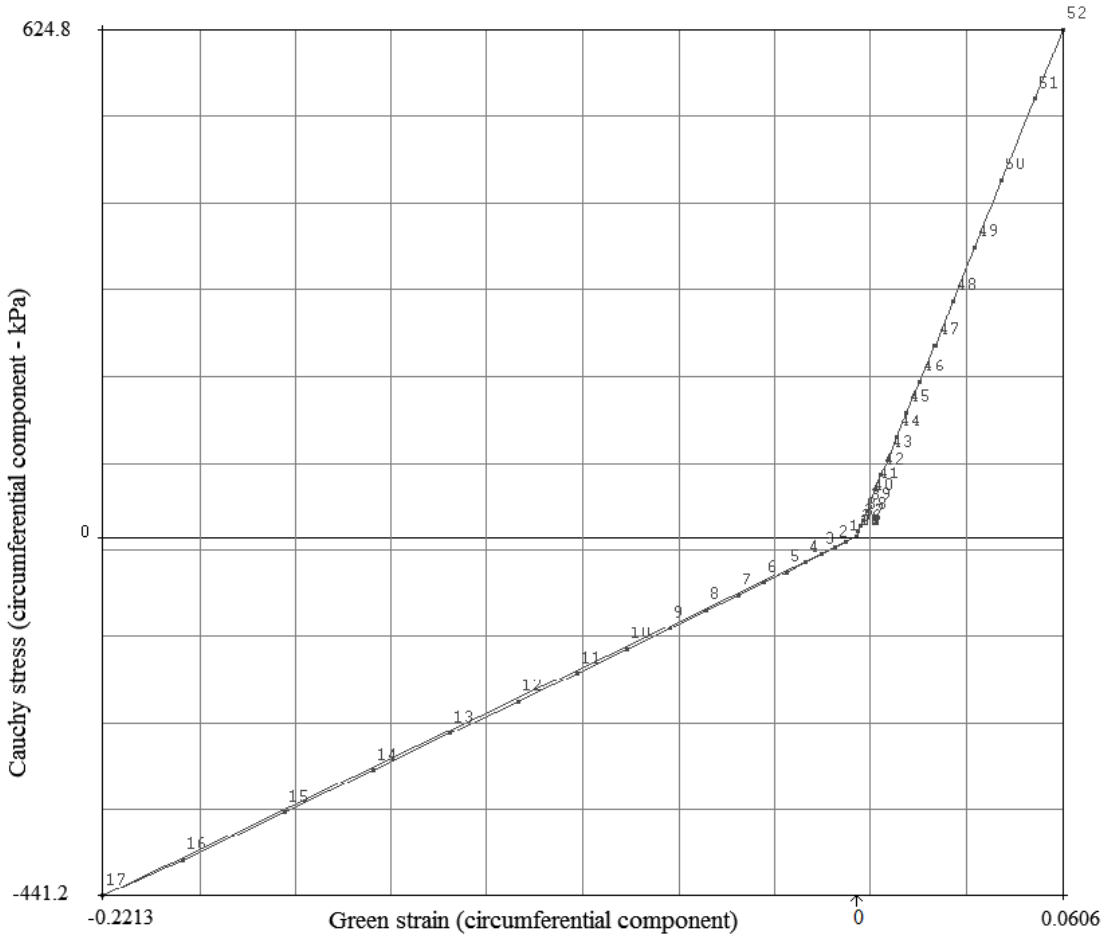

Figure 10. Stress strain diagram from loading of cylinder using bilinear material model in Marc.

4.4 Discussion of Endograft Experiments

A linear fit, of the uniaxial stress-strain data of all designs tested, gives average Young's moduli values of 2 MPa for compression and 20 MPa for tension. This range of values is not out of line with other values used [75].

Variations in the data are likely present because of the measurement technique used – particularly the digital caliper and the assumption of cylindrical nature of the graft. While it is crudely cylindrical at the macro scale – the pressure of the stent struts

and tethering by suture creates structures that are not completely uniform in diameter or circular. The contacting method of the measurement may have also slightly influenced pressure readings and agreement between tests, as well as the fact that the compression test applied to only part of the endograft instead of its full length, resulting in local edge effects.

5. BUILDING PATIENT-SPECIFIC MODELS

5.1 Background

Imaging studies, which are part of the standard of care for AAA diagnosis and follow-up, can provide data useful to building computational models specific to patients and their treatments. Ultrasound studies sometimes quickly confirm or detect AAA but do not provide wholly reliable 3-D geometry measurements. However, diagnostically definitive imaging techniques, e.g. fluoroscopy and computer tomography (CT), provide information on the blood flow and structure within the body and are useful for surgical planning/detailed diagnosis.

Fluoroscopy is an imaging modality that uses low intensity x-rays – generating a 2-D image that captures information through the entire thickness of the body using an adjustable gantry. Such a technique is useful in treating/assessing cardiovascular disease as visualization of blood flow and lumen geometry can be achieved with the addition of an injected contrast agent. During the endograft implantation procedure, fluoroscopy is used as an aid to assist the surgeon in directing catheters and guidewires. Fluoroscopy images confirm arterial dimensions before implantation and confirm successful flow through the graft immediately after implantation during the surgery. However, because of its two dimensional nature, it is not generally useful for 3-D reconstructions.

CT scans consist essentially of regularly spaced planar x-rays scans and provide information on the structures within the abdomen through the 2-D slices themselves and/or as a 3-D reconstruction. The CT scan can confirm a preliminary diagnosis of AAA, suspected from physical exam or ultrasound screening, and it is useful for initial

graft sizing and procedure planning/eligibility determination. CT scans are part of annual post-surgical treatment follow-up to confirm proper graft placement and functionality to ensure lack of endoleaks and size stability/reduction.

Some commercial software packages and services, such as M2S, use CT scans to plan endograft procedures and to visualize and measure AAA/endograft parameters such as sac volume and constituent distribution/locations. One product provides information on centerline locations, lengths, and angles as well as visualization of graft placement and constituents of the aneurysm including thrombus, calcification, and wall. This information can be useful for planning the endograft procedure and assessing procedure feasibility. Although, a radiologist might glean the same information by doing a 3-D reconstruction for the purposes of surgical planning and decision making in collaboration with a vascular surgeon instead.

Shape variation, between AAA and within a particular AAA, is important as it implies that loads and stress distributions will not be uniform throughout the AAA and could be useful to predict rupture location. Otherwise similar aneurysms rupture in different locations due to differing morphology. Some studies have reported that rupture is more likely to occur retroperitoneally [79] and [5]. The goal patient-specific modeling generally is to help the individual instead of populations; characterization of an individual's condition requires an imaging methodology with greater specificity and precision than a population based geometry.

5.1.1 Patient-specific Modeling

The modeling of patient-specific geometry begins with the acquisition of CT scans which are acquired prior and post implantation. CT scans are also taken as part of typically annual follow-up exams to ensure treatment effectiveness, whether or not leaks are present, and to determine if the aneurysm is continuing to grow. These follow-up examinations allow analyzing a time series of patient geometries.

There is significant literature available on methods for segmenting images into 3-D structures/images/models. The problem of fitting surfaces to 3-D points is present in a wide variety of fields such as reverse engineering, automotive design, and neuroscience. For an example of one of the possible techniques for converting surface data sets into surface models with C2 continuity, see Smith et al. [80].

Other groups have used a relative mesh density established in one patient-specific case as their foundation for considering the other models run at similar mesh densities to be resolved to an adequate degree of accuracy [7]. This assumption is reasonable if the cases are similar enough or if the most sensitive case was the foundation.

5.1.2 Boundary Determination

One of the fundamental issues in 3-D reconstruction of AAA is the uncertainty of the boundary between constituents that are generally differentiable due to the different absorption amounts resulting in different intensity in images. The uncertainty is either a result of resolution issues (spatial and temporal) or the nature of the structures themselves. The diffusivity of x-rays limits the CT scan precision, as does the non-

instantaneous nature of the acquisition time. The result of the limitations is images that represent essentially an averaged, both spatial and temporal, geometry. The small thickness of the vessel/aneurysm wall is at the limits of resolution, and contrast may be such that wall thickness is clear in only a few places, if any.

Segmentation algorithms try to deal with the uncertainty of the precision of the underlying images by using a variety of techniques – one of the more common being growth. In growth segmentation, similar intensity of nearby 3-D pixels controls the expansion of a surface to its boundaries. Level set methods differentiate geometry using a calculation of rate of change between neighboring pixels to create a map of areas of dramatic intensity changes. These intensity change lines are then useful for separating out the different constituent groups or identifying their borders [81].

Smoothing algorithms, algorithms that make the boundaries more continuous and rounder, work hand in hand with segmentation algorithms. Due to the nature of the images acquired by CT and the inherent speckle, averaging, and pixilation, smoothing is required to get the surface to match the reality seen during surgery, where the vessels are smooth and changes in diameter and shape are typically gradual in appearance. The result of reconstruction, which is largely subjective to the user, will have an impact on the finite element models, in that sharper edges lead to non-physiologic stress concentrations and too much smoothing causes unrealistic shapes and spreading of stresses. This issue was addressed in the study by Doyle, where they found a medium level of control points and then smoothing provided the most reasonable results [82].

5.2 Methods

The process of converting images into patient-specific finite element models with multiple components took several steps. After patient selection and image identification, images were converted between programs for segmentation and mesh generation. Subsequent to mesh generation, analyses determined centerlines and measured aneurysm shape change. A flowchart of the steps and programs used in reconstruction is shown below.

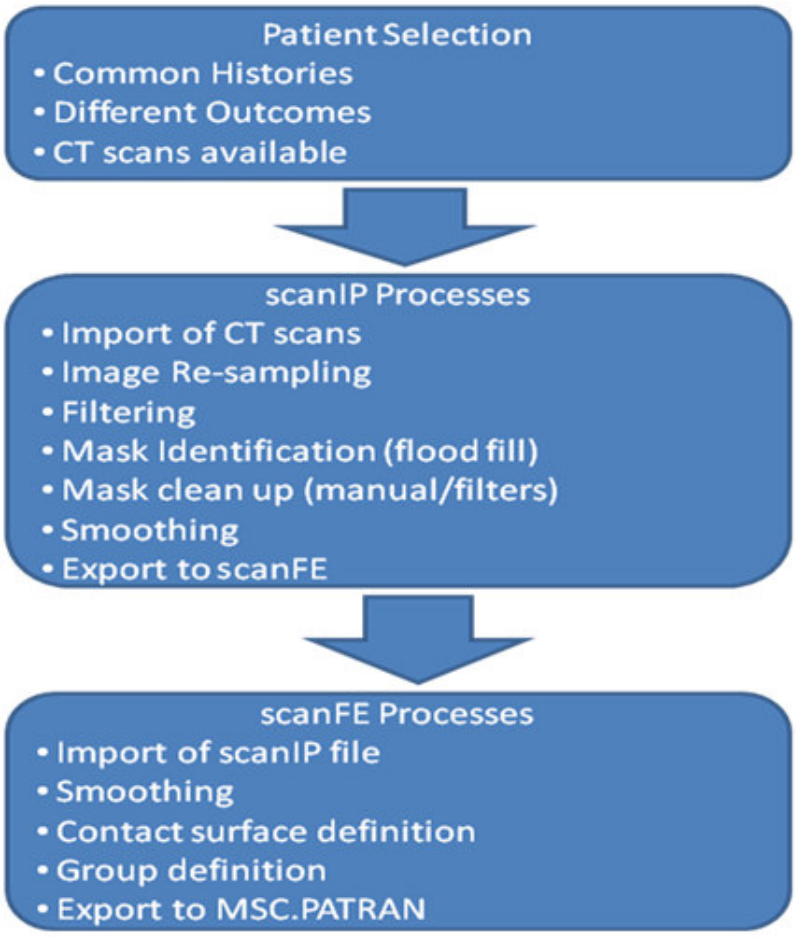

Figure 11. Conversion process of images into finite element models.

Shown in Figure 11 are some of the key steps in the conversion process from image stack to finite element model. Images from some of the steps in the process are shown below in Figure 12.

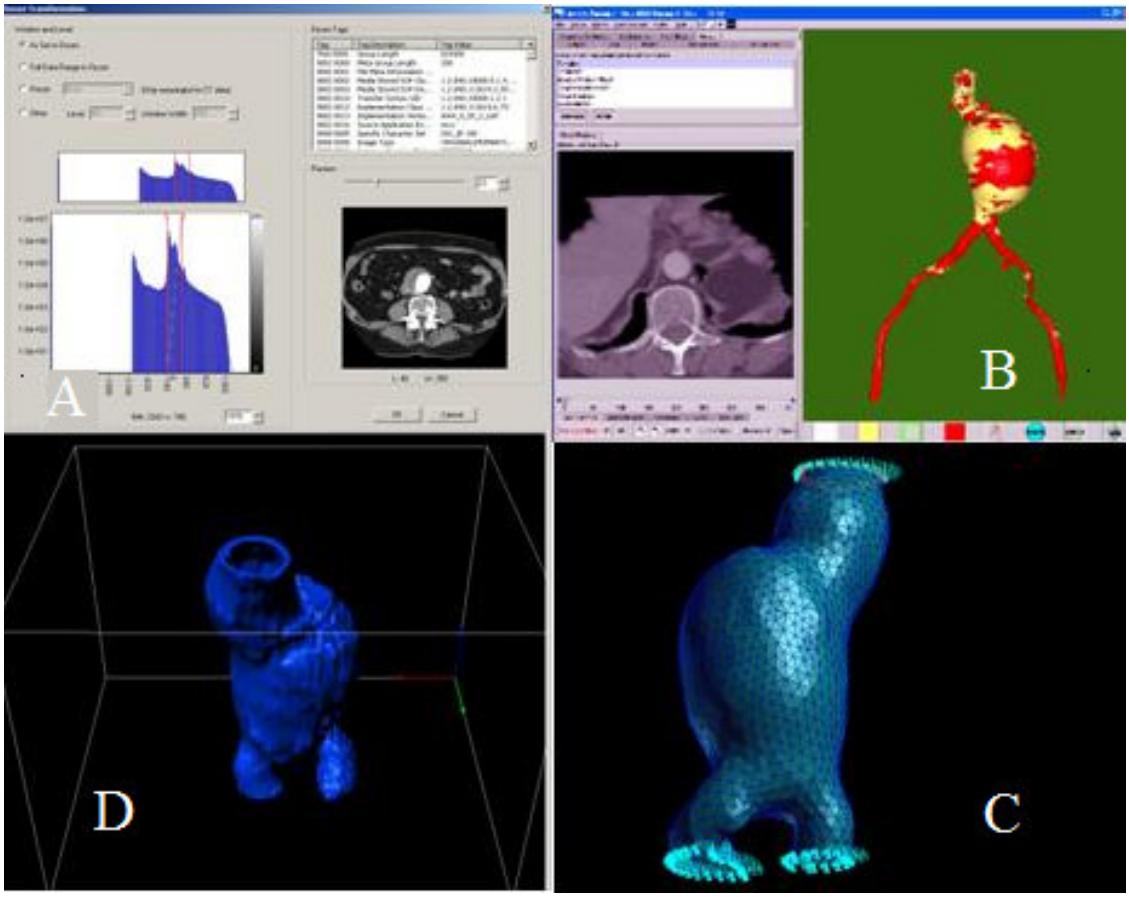

Figure 12. A-D clockwise from upper left. A) Image from scanIP of dynamic range, B) Reconstruction from M2S, C) Finite element mesh, and D) reconstructed geometry pre-smoothing

5.2.1 Patient Selection

Two patients were identified based on similar backgrounds, yet different responses to treatment, namely, aneurysm stabilized and aneurysm shrinkage. Background similarity depended on several factors – endograft device (brand and dimensions), age, blood pressure, original sac volume/diameter, smoking history, family history of AAA, and availability of pre-scan, post-scan, and long-term follow-up scans. The patients were potentially differentiable by changes in the aneurysm sac subsequent to the surgery (growth, shrink, stable) or in growth rate prior to surgery. IRB (Institutional Review Board) approvals from both Scott & White Hospital in Temple, Texas and Texas A & M University located in College Station, Texas allowed access to scans and pertinent medical records. The approval covered patients treated with AAA and iliac artery aneurysms between August 2000 and August 2007.

Despite incomplete medical records, patients with differing outcomes and similar histories were identified. Patient "A" had sac stability whereas patient "B" had sac shrinkage based on observations by radiologists of their CT scans. The differences did not appear to be explicable by endoleak. Once patients were identified by looking through medical records for similarity and completeness, the scans were transferred to College Station for conversion into finite element models. The nature of the medical records made identifying smoking history and other factors of interest difficult. Patients do not have all information of potential future research interest recorded at each visit and the forms are not like a checklist.

5.2.2 Image Preparation

The obtained DICOM images had a resolution (at worst) of nearly 0.7mm x 0.7mm x 2.5mm resolution. The DICOM format allows for embedding additional information (such as patient name, hospital, accession number, etc) into the file as well as the image itself. The format should have allowed the images to be directly imported into scanIP (Simpleware Ltd, Exeter, UK), but there were difficulties with some of the files requiring an intermediate conversion to tiff files. These difficulties included the lack of proper co-registration of the images by scanIP and an inability to determine properly the dynamic range of the contrast and brightness. When possible, the patient-specific models were generated from CT scans that were conducted in the presence of an IV contrast agent. The usage of contrast enhanced CT scans provides greater information on the lumen boundary by enhancing its brightness compared to the wall and thrombus. This thickness resolution limitation has in part to do with the resolution of CT being near 0.5 mm x 0.5 mm x 2 mm thickness, at best, within each slice. The wall itself is typically only 1.5 mm thick ([51]. Speckle is also present in the images. Resampling of the images made the voxels within the models 1.5 mm x 1.5 mm x 1.5 mm in size.

5.2.3 Segmentation

Reconstruction was primarily accomplished using Simpleware Ltd.'s scanIP program (Exeter, UK); software written expressly for 3-D reconstructions for computational modeling. A flood-fill command with connected region growing filled the moderately and brightly colored areas, creating a mask covering the lumen and the

thrombus as well as some other high-density structures. A second mask was generated over just the brightly colored areas using a higher threshold. The subtraction of these masks left behind a mask for just the thrombus and vessel wall. A similar process separated out the thrombus from the wall. It is difficult to distinguish the components of the AAA because the signal strengths are not particularly different amongst the soft tissues when compared to the noise that is present within the images. To address this issue, noise reduction filters were applied to the raw image background, which allowed the mask borders to be more smoothly defined. Also, if other structures (such as the vena cava) were included in masks, they were manually removed. The resulting masks were processed further to smooth any edges or inclusions that appeared to be artifacts, and were processed to remove small branching vessels for simplicity. There was difficulty in measuring wall thickness, even where the thickness of the wall, not including thrombus, was highlighted or indicated by nearby confining structures. For simplicity, the wall was assumed to be 1.5 mm thick for the two patients studied here and this thickness was achieved by defining the wall mask by a dilation process of one pixel in all directions from a mask combining the graft's mask, if present, as well as the lumen and thrombus masks. Additionally, any calcifications present were considered as part of the wall instead of being separated out and associated with different properties.

CT scans typically cover a large abdominal area that includes much of the aorta as well down into the iliac and femoral arteries of the legs. The area of interest for all models constructed was the region between the lowest renal arteries and the bifurcation

of iliac arteries into internal and external branches. Portions of the image stack/reconstruction beyond this region in any dimension (x, y, or z), were cropped out.

Defining the endograft shapes required two masks, one for the main body and one for a contralateral leg. The endograft legs were defined with separate masks so that the contact between the legs could be used to define shell elements. These shell elements in the region between the legs provided structural stability and proper expansion characteristics for the endograft, as well as a more faithful reconstruction of the patient's geometry.

The mesh density of the model was controlled though parameters in scanIP and scanFE. Increasing the sampling rate of the image is a way to refine the mesh; mesh refinement is essential to accurate calculation of stress tensors and strain tensors as one checks the accuracy of one answer by comparing it to the answer of a mesh at different density of the same model. This method is quickly limited by size limitations on the model imposed by the capacity of the solver or solving computers. Another means of controlling the number of elements and nodes in these models was through the reduction of elements within the thrombus. The solid thrombus provides a region whose thick interior structure could be composed of elements with a larger size and lighter density than those within the wall.

5.2.3 Shape Analyses (Calculations of Centerline and Hydraulic Diameter)

Analysis of the shapes that resulted from the reconstruction process was important for comparisons between cases. Analysis consisted of node definition, centerline calculation, and hydraulic diameter calculation. The hydraulic diameter

calculations required finding the planes normal to a calculated centerline at various z (axial) values. Hydraulic diameter was calculated for the outer surface of the aneurysm wall and for the outer surface of the endograft.

Shape analysis was conducted on endografts and on the outer walls of the aneurysm reconstructions. ScanFE, which allows for the export of node sets as groups in Patran, defined the basis node sets of the reconstructions. An analysis deck written by a Patran command provided the nodal position data, which was imported into Matlab (Mathworks, Natick, Massachusetts). The Matlab algorithm takes an initial data set and measures a centerline from nodes identified using convex hull over a range of z values. Convex hull determines which points lay on the outer edge of a 2-D polygon. The centerline is calculated by determining the average position of the points on the outer edge at fixed z sub-range. These values then provide a starting point for the fitting of a centerline. Subsequent to the selection of these points, they are used in the calculation of the normal plane. The normal plane is then used to identify points laying in close enough proximity, such as within 1 mm. These points are then rotated and projected onto the plane so that they lie in 2-D. A convex hull operation is performed to determine those on the outer border, and upon these nodes, an operation is conducted to determine their center. The operation accounts for unequal spacing of nodes on the edge by oversampling based on the length of the boundary line segment so that artificial points are created of equal distance apart. These points can then be averaged to calculate a truer centerline. Hydraulic diameter (D_H) was calculated from these boundary nodes, using the formula:

$$D_H = \frac{4A}{U}$$

where A is area and U is total perimeter of the polygon defined by convex hull on the nodes of interest.

For the endografts, node sets were analyzed separately for the main body graft and for the contralateral leg. The goals of the analyses were measurements of diameters for identification of compression or tension of the structure in order to associate specific regions with the strain state of the implanted endograft. The endograft node sets were segmented using both a high and low sampling rate to see the effect of sampling rate to confirm the robustness of the procedure. Also analyzed was the effect of the rotations on the accuracy of the centerline and hydraulic diameters.

For each AAA, the nodes representing the outer surface of the wall over the entire region of interest were used in analyses to determine the diameter changes over time. The calculation of a splitting centerline through a bifurcation is non-trivial. The bifurcation was not handled directly in these models and instead the code allowed a centerline to continue to describe the average of the outer nodes of the iliac legs. The term hydraulic diameter in this region is meaningless relative to its true definition because the convex hull operation operates to connect both iliacs.

Quantification of the models' differences in shape over time was done by the calculation, from nodes in the model walls, of hydraulic diameter in addition to calculations of maximum radius from center line and slice area. Hydraulic diameter provides a means of assessing the "diameter" of non-circular cross-sections and has been used in fluid mechanics. It is defined as four times the cross-sectional area divided by

the total perimeter – reducing to diameter for a circle. Maximum radius was calculated as the largest distance from the centroid of a slice to any node in that slice – closely paralleling the maximum diameter measurement of the radiology department. The slice area calculation is the cross-sectional area of the area encompassed by the outer nodes of a given slice. These calculations could either be done relative to a calculated centerline or done relative to the axial direction, which was set fundamentally by patient alignment within the CT scanner. Axial alignment varied slightly between visits and patients. Alignment of these quantification measures for comparison between models was handled by matching the bifurcation's position; as it was assumed that the bifurcation was reasonably static between models. The initial quantification of model shapes was done by radiology, who calculated the maximum diameter and aneurysm sac volume for each patient at each time point and provided the fundamental classifications of "stable" and "shrinking".

5.2.4 Boundary Conditions

The calculation of pressure boundary condition requires identifying the surfaces of the lumen. To do this, a node set exported by scanFE lists those nodes contacting the interior from the thrombus and wall masks. After comparison with the element connectivity list written by Patran, the appropriate matching element surfaces are compiled into a list that is used for the application of the pressure load. This provides a pressure load that acts normal to the surfaces on the interior, regardless of their orientation because the surfaces are the element faces.

5.3 Results

5.3.1 Patient Parameters

Two male patients were chosen, of advanced age (i.e. > 70 years old), with no apparent family history of aneurysm, same graft type (AneuRx), with scans available for all periods (including pre treatment, post treatment near term, and post treatment long term), and yet with different outcomes. Patient A had an essentially stable outcome – with slight increase in volume and reduction in maximum diameter of his AAA, whereas patient B had a reduction in aneurysm volume and maximum diameter, as reported by radiology reports based on reconstructions done internal to Scott & White on the CT scans that were subsequently used for FEM model creation (see Table 3).

Table 3. Reconstructed patient parameters

	Patient (A)	Patient (B)
Characteristic	"Essentially stable"	Reduced
Gender	Male	Male
Age at implant	71 yr	75 yr
Time to 1st follow-up scan	24 months	20 months
Time to 2nd follow-up scan	43 months	32 months
Family History	None reported	None reported
Smoking History	None reported	None reported
Pre-Op Sac Volume/ Maximum Diameter	108.1 cc, 44.5 mm	179.8 cc, 62.3 mm
Follow-up Sac Dimensions	1st : 111.3 cc, 43.1 mm 2nd: 116.4 cc, 41.3 mm	1st : 156.9 cc, 58.8 mm 2nd : 146.4 cc, 57 mm
Graft Dimensions – as recorded in surgical notes	AneuRx 28 mm x 60 mm x 13.5 cm 8.5 cm x 16 mm contralateral limb (right) Extender limbs both sides 8.5cm x 16 mm extender	AneuRx 28 x 16 x16.5 mm 16 x 8.5 right iliac limb extender, left 11.5 x 16 x 16 right limb extender, 11.5 and 8.5 extenders on left

5.3.2 Generated Surfaces

Surfaces that define the luminal surface, thrombus, and vessel outer surface were created for the finite element models. An example of the generated surfaces is shown in the figure below. It shows the nodes on the surface of each of the components of the untreated AAA. The red nodes are along the lumen, the yellow nodes along the thrombus and wall contact region, and blue nodes represent the wall's outer surface. The reconstruction process takes slightly less than a day for each stack of images, with time improvements seen as the operator becomes more experienced.

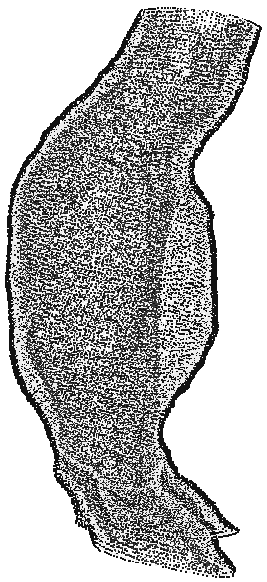

Figure 13. Nodes of surfaces of the wall and thrombus for Patient A shown prior to treatment.

In Figure 13, the left side of the image indicates the anterior side of the aneurysm; the posterior side is bulging and close to contacting the spine (spine not shown). Also noteworthy is the lack of other secondary structures like spine or vena cava, and that the reconstruction includes part of the iliac arteries.

5.3.3 Mesh Density

The resampling of the original image stack primarily controls the density of the mesh. Subsequent mesh adaptation is applied so that elements are not overused in the central region of the thrombus. An application of this can be seen in the image below in Figure 14.

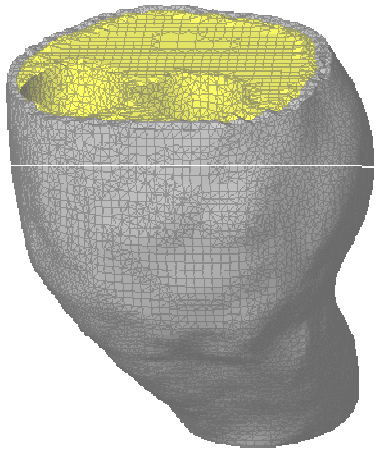

Figure 14. Mesh density and mesh adaptation illustration showing top half of aneurysm from below. Thrombus is represented with yellow elements and vessel wall with gray elements.

5.3.4 Segmented Images

The images are segmented to allow for separate properties to be applied to the different components (such as graft, ILT, wall) of the model. An example of segmented

reconstruction of the endograft into two parts and AAA is shown below (Figure 15). The wall and thrombus are semi-transparent. The connection between the two parts of the graft is not ideally smoothed.

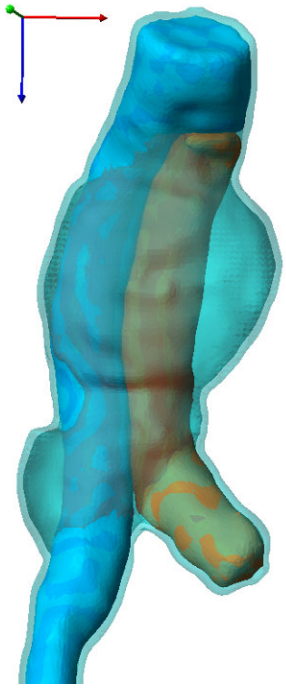

Figure 15. Segmented reconstruction from patient B shows the two-mask endograft and aneurysm wall.

5.3.5 Centerlines and Hydraulic Diameters of the Endograft

For each AAA, a centerline and hydraulic diameter (in 2 ways) was calculated. Diameters along the normal direction were typically 4 mm less than those measured perpendicular to the axial direction.

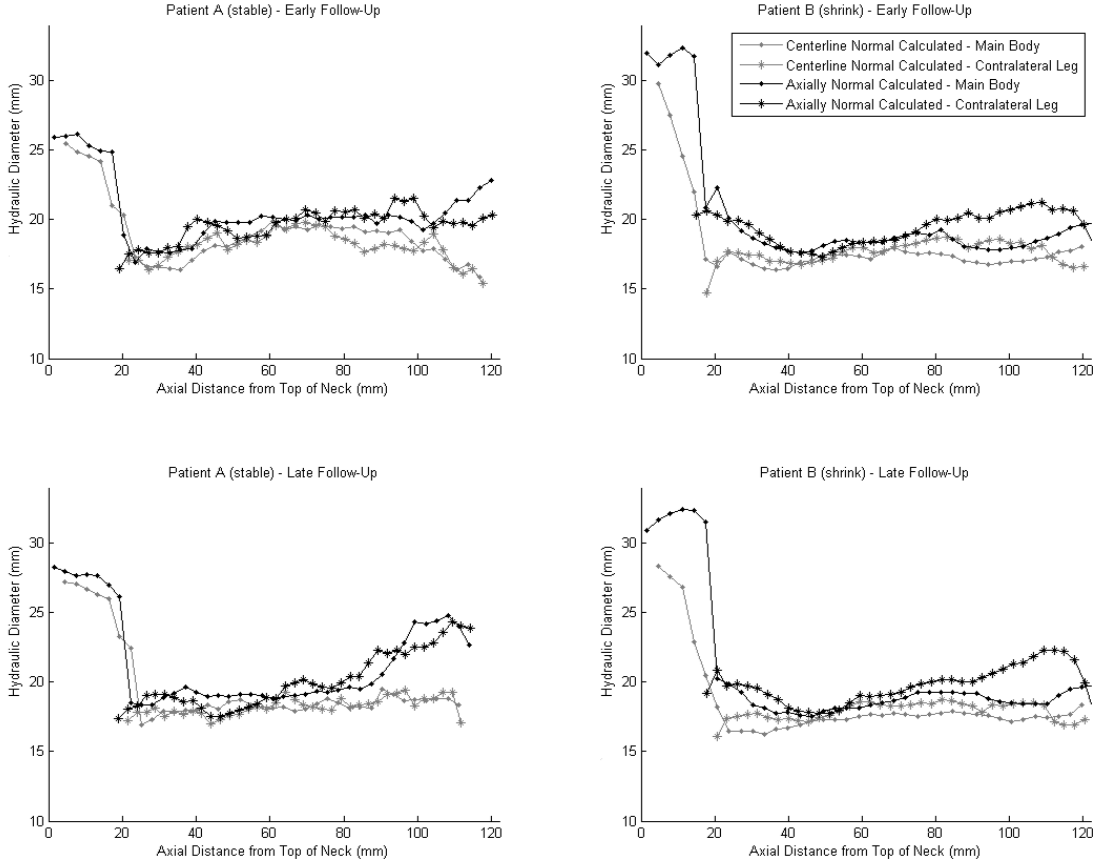

Figure 16. Hydraulic diameters (calculated normal to the centerline and normal to axial direction) as functions of axial distance from top of neck.

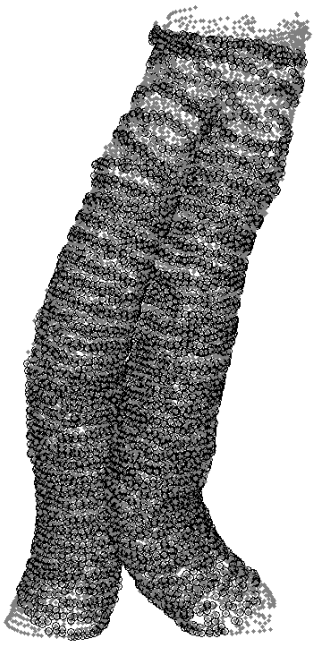

Figure 17. Endograft, with nodes used in hydraulic diameter normal to the centerline calculation shown as black circles; grey dots are graft nodes.

5.3.6 Aneurysm Hydraulic Diameter Over Time

Change in aneurysm hydraulic diameter over time was such that using the normal hydraulic diameter, both aneurysms reduced in diameter. The reduction in patient B, which had been characterized by the radiologist as having a shrinking AAA, is greater. Both had a greater reduction in maximum hydraulic diameter between the initial and 1st follow-up compared to between 1st and 2nd follow-ups (Figure 18 and Figure 19).

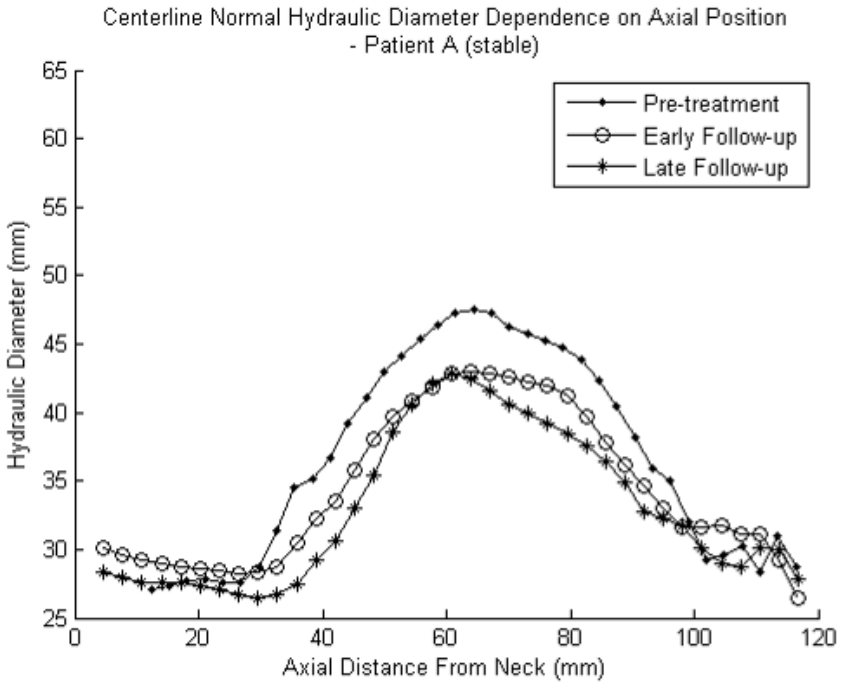

Figure 18. Hydraulic diameter from patient A (stable).

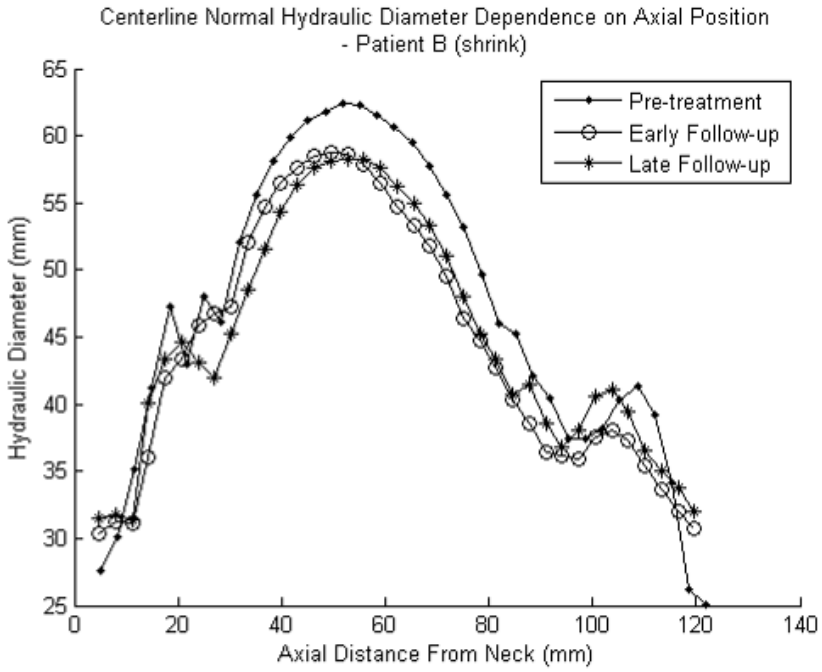

Figure 19. Hydraulic diameter from patient B (shrink).

5.4 Discussion

Models of patients with a stable aneurysm and shrinking aneurysm were created from CT scans that covered pre-op, initial follow-up, and 2nd post-op follow-up. The selection of patients was made difficult by the nature of medical records, but relatively comparable patients were selected that still had different outcomes despite apparent technical success of the procedure (no leaks, no migration).

5.4.1 Reconstruction Accuracy

The accuracy of the models constructed from CT scans is limited by factors related to the scans (spatial and temporal resolution), by factors related to the procedure implemented (semi-automation, smoothing, image re-sampling, constituent

identification), and by factors related to the concept (lack of contact with other structures, region of interest, and patient alignment).

The spatial resolution is affected by the limitations of the CT scanner as well as its imaging protocol. Motion averaging occurs due to the finite time of imaging and the lack of a gating process to synchronize the images to a period of the heart rate. This deficiency impairs accuracy because of the pulsatile nature of the vessel in response to changes in blood pressure in the aorta over the cardiac cycle. Variation between instantaneous and average blood pressure may also influence the representativeness of the CT scans reconstructed.

The procedure used has inherent limitations including that of a semi-automated technique, image re-sampling, and constituent identification. A semi-automated technique that requires human involvement introduces human variability; this variability was somewhat mitigated by having the reconstructions done by the same person. However, the method of reconstruction took substantial time (a half day) and its reproducibility was not tested. The surfaces are reasonably reflective of what has been observed in vivo, possibly due to smoothing algorithms. The smoothing does not appear to be severe enough to take out the native angularity of the abdominal aortic aneurysm. However, some of the smoothness and the geometry are affected by the nature of the underlying DICOM image sets. This reduction, if not carried too far, is still adequate for resolving the stresses present in the aneurysm wall and providing some details regarding the stresses present in the thrombus. Image re-sampling reduces some of the information that could be gleaned from the original stack. However, it does allow for models to be

run successfully, which was more important. Constituent identification in this study was done using thresholding based off of intensity values, except that apparently calcified regions were lumped into the wall. This simplified calculations and modeling, but prevented fully accurate, representative modeling.

The reconstructions of AAA, for mechanical analysis, by CT scan were also limited in what structures were considered. Only the AAA's wall, thrombus, and potentially endograft were modeled despite the presence of other structures in contact or proximity with them such as spine and vena cava. The region of interest including iliac arteries up to just below the renal arteries, limits the involvement of potentially convoluting as well as illuminating factors. In this study, the aorta and some connected branches are isolated through the application of filtering methods and cropping that remove other structures within the thorax, eliminating the possibility of modeling perivascular tethering.

Patient alignment is also an area that could have an effect on reconstruction comparisons. For although comparison between models was done relative to a centerline was used, the centerline calculation itself can be affected by more than just changes to the AAA. The patient is always lying on their back when getting a CT; thus, the general orientation is consistent between scans, but body mass changes and shifting slightly left or right were present in the time series of images, as the patients had aged generally two years between scans.

5.4.2 Centerline and Bifurcations

In addition to the uncertainties created by the limitations above, the centerline accuracy is limited by the approximations used in its calculation. Though the method is quick and relatively straightforward, it is of limited precision in that the surface definition is not regular and there is no smoothing other than averaging of neighboring points. It is also based on the aneurysm wall and not the lumen. The bifurcation, as was mentioned in the methods, is not accounted for, and thus there is no accounting for how it is impacted by treatment or time. However, by using two parts for the endograft, the common iliac arteries can be assessed individually. The usage of separate masks for the endograft legs meant that the region of graft were the legs meet could also be modeled with shell elements. These elements in between the legs are necessary so that the pressurization of endograft leg remains appropriate and realistic.

5.4.4 Rate of Growth

An interesting attribute not considered was growth tracking prior to surgery. It would be interesting to see what relationship exists between pre-treatment growth rates and post treatment shape change.

The region between the lowest renal arteries and the bifurcation of iliac arteries into internal and external branches was chosen for all models as it represents the region typically covered/contacted by endograft components. This choice is beyond the region typically modeled in prior works [55]. The advantage is a greater specificity to the mechanical environment of that patient and better distribution of tethering loads.

5.4.5 Classification of Outcome

From the results of hydraulic diameter calculations, it appears that both sacs demonstrate shrinkage. The shrinkage of patient B, is larger, and occurs over a greater portion of the sac. Interestingly, in both cases the majority of the size change occurred during the first interval. Change between follow-ups was minimal, though reductions are seen in hydraulic diameter of the iliac aneurysm sac of patient B and in the distal portion of the AAA sac in patient A.

5.5 Conclusions

In order to assess the aneurysm shapes after implantation of an endograft, patient-specific models were built from CT scans from patients identified as having sac stability and sac shrinkage after endograft treatment. These models were analyzed and compared for centerline and hydraulic diameters to assess change over time. The constituents (endograft, thrombus, and vessel wall) were separated using a semi-automated technique, which was not ideal due to the amount of time required and the expertise required by the operator. However, the technique was adequate and sufficient for separating the constituents and building a model with appropriate continuity between structures. This continuity, of course, is essential to finite element structural models running quickly and accurately. Although the accuracy of the smoothing technique was not investigated, the results appeared reasonable in comparison with others. Generally, the reconstructions were not confirmed against the patients' true geometry in any direct way. Indirectly, the reconstructions were confirmed against the CT scans for proper

appearance and it was shown that measurements of the CT matched closely to the patient-specific finite element models.

6. FINITE ELEMENT METHOD AND ITS USE

6.1 General Finite Element Method Background

The finite element method is a means of engineering analysis that involves decomposing the problem into small regularized parts. The method includes seeking an approximation to the solution of the descriptive PDE as a linear combination of the parts, deriving the relations among the nodal values of each part, and assembling the parts to obtain the solution to the whole. It can be used to determine equilibrium configuration of deformable bodies under load and is used for such purpose in the research presented herein. The fundamental feature of the finite element method is the representation of the bodies by smaller elements. The elements are regular in shape and are used for simplifying the calculations and the solution representation. The element dimensions are defined by nodes which are located at the corners for linear elements and additionally at the middle of the edges of the sides of quadratic elements.

For the purposes of the studies described here, an element can be thought of as a brick (3-D solid cube like structure), and nodes considered to be like points at the corners of the brick. Elements are put together like blocks and varied slightly in size and shape to combine to represent the original total model. The elements are put together in a special way. The corners and edges all match up exactly so that there are no unintentional gaps or unintended holes. For a twenty node brick element, the nodes lie at the corners and at the midpoints of the sides.

Nodes are defined by their location within the coordinate system and by a unique number that indicates which node it is. The node numbering is used so that each node

has a unique number within the model allowing it to be distinguished and uniquely referred to. Each element can then be defined by the nodes that lie along its edges and corners. The element's orientation is precisely defined by the ordering of the nodes that make up its corners and edges. The orientation is also useful in identifying the faces, which can then be identified by naming structure for the application of loads or boundary conditions. In the figure above, the numbers indicate the proper ordering of the nodes that make up this element. Node ordering is essential for the evaluation and assignation of material properties/calculation of the stiffness matrix as well as the consistent creation of the overarching element's edges as a sort of connect the dots can be employed to determine the edges once the prescribed nodal order is known. The order is prescribed by the underlying code and can vary between codes or can be defined by user specification. However, as employed here with commercial finite element software, the ordering and numbering of nodes is taken care of in an automated way that requires no extensive intervention by the user [83]. Although, there may be exceptional cases where nodes and elements need to be modified or created directly.

A data structure called the connectivity matrix is used to define each element. Elements are assigned a number and listed with the nodes that comprise them in the order that they need to be in to recreate the element without turning inside out or having edges crossing through the elements instead of being on the perimeter where they belong. The connectivity matrix is usually generated by the commercial code and requires no intervention from the user. However, as was noted previously in the geometric reconstruction methods section, the connectivity matrix was used in

conjunction with a list of nodes belonging to the lumen in order to define the surfaces over which pressure would act. The connectivity matrix and the specificity of it when defining elements means that one can use it to consistently define faces of elements from the components of it. These regular definitions can then be associated with a numbering scheme that allows the six faces to be numbered and referred to more simply than as if than through the listing of nodes. Also integral to the definition of faces is which side of them is the outward face. This definition is especially important when applying pressures. The code that determines pressures from nodes takes the information in the connectivity table and the information on how the element faces are defined in terms of nodal locations to determine which elements and which of their faces have pressure on them.

A data structure consisting of nodes and their coordinates is also necessary. This listing is related to the coordinate system. For the models run here, the default Cartesian (X, Y, Z) coordinate system was used, though it would have been possible to use a cylindrical coordinate system. The usage of a coordinate system other than Cartesian complicates the setup of the analysis. Also, because of the nature of the underlying equations, the method is fundamentally coordinate system independent. Though it does present results in a coordinate system, a coordinate system of choice corresponding to the maximum principle directions can be chosen. In other work, it was confirmed that as expected, this reporting option of using maximum principle directions and values highlights and confirms the coordinate system independent nature of the method and the underlying mechanics.

The purpose of the nodes is the representation of the solution at points of interest. In order to accomplish this, it needs to be able to interpolate the underlying equation of interest and still satisfy the boundary conditions. In the models run for this dissertation, the interpolation used Lagrangian functions for both linear and quadratic elements. The interpolation functions are often evaluated by numerical integration. The method of choice used by MSC.Marc is Gaussian integration, which involves evaluating the approximation at Gauss points which are not located at the nodes. The number of Gauss points required for exact integration depends on the nature of the underlying function.

Also noteworthy, is that in addition to the solid elements (bricks) it is possible and generally preferable to model thin structures with shell elements. The purpose of shells is to model the physics of thin structures in such a way that requires less computational effort, though it provides less information on the distribution of stresses across the wall. Shell elements exist as 2-D sheet pieces in a 3-D environment. These elements also have corresponding reduction in nodes to match the reduction in dimensions.

Properties of elements may vary between elements within a model so that each element need not be homogenous. In addition to varying in type like as solid or shell, they vary in the properties assigned to them. The properties assigned to them are related to the specific problem being solved, and in the case of a structural model involve describing the underlying materials that the problem is about. These materials which compose the structures under analysis are described by physical constants which relate to their underlying mathematical description or material law/strain energy function. It is

desirable to associate constants with sets of elements instead of needing to associate them to each element individually. To do this, there are two methods. The first of which is that of associating a finite element mesh, or collection of nodes and elements, with a solid. Solids and other geometric structures can be created within Patran much like any CAD (computer aided design) software – either directly or from simpler geometric constructs like line segments, arcs, or surfaces. This method works well when the mesh is created on top of solids or other geometric constructs, but does not do well with the free form meshes that are imported from scanFE. The axisymmetric model, which is described in detail in the subsequent chapter, was created such that each constituent (wall, thrombus, graft) existed as part of a separate solid, but each solid shared common surfaces and edges. It was important for them to share common surfaces and edges so that when meshing occurred and the nodes and elements were created, they were created in such a way that they matched up between the different structures. Matching is important because it allows for an equivalence process which removes redundant nodes and ties the solids of the structure together. This tying is important for accurate solution and accurate representation of how close/connected the components of an abdominal aortic aneurysm are. The second method is the usage of groups. With groups, elements within a model can be segregated so that the elements belonging to the different constituents (wall, calcification, thrombus, graft, etc) are separated. The groups can be posted to the view-space of Patran individually so that they can be selected and the properties assigned. While properties will not be updated as

the mesh is changed, groups still provide a fairly efficient means of assigning material properties to a large number of elements in a semi-automated way.

The finite element method has been applied to a variety of problems in engineering, including prior work in biomedical engineering, and in non-biomedical applications. FEM work is particularly commonplace in aerospace and automotive design. In these fields, there is great emphasis on cost effectiveness, reliability and performance. FEM provides a means for analyzing the structures and potential structures in a rigorous way.

Essential to work done in the finite element method analysis of structures is an understanding of the underlying mathematical framework. The next section goes over it in some detail.

6.2 Continuum Mechanics

"The *continuum hypothesis* asserts, however, that the gross (or macroscopic) response of a body can be well approximated by assuming locally averaged properties, defined at every point in a body, provided that $\delta/l \ll 1$ where δ is a characteristic length scale of a microstructure of the material and l is a length scale of the problem of interest."[15] For solving problems in continuum mechanics there are five classes of relations: kinematics, forces, balance relations, constitutive relations, and boundary/initial conditions. Kinematics deals with motions apart from mass or force. Forces are the loads acting upon the structures. Balance relations ensure that equilibrium is defined and sought. Constitutive relations define the relationship between

materials and material behavior. The boundary/initial conditions define the problem in terms of the specific constraints upon it.

Kinematics includes a consideration of the motion without mass or force. It deals with how lines deform in a sense. Specifically, the quantity of displacement (u) is given by u(X,t)=x(X,t)-X, where X is original position relative to a common origin, x is current position, and t is time(from original to current) – u, X, and x are vector quantities. From x and X, a deformation gradient second order tensor can be defined as $F = \frac{\partial x}{\partial X}$.

The Jacobian is the determinant of the Jacobian transformation matrix. The term determinant has its usual matrix/linear algebra meaning in that definition [84].

Strain is a measure of deformation that ideally does not incorporate information about rigid body motions of an object but instead indicates how much it itself stretches or is compressed. To this end there are a variety of strain measures that are useful in different situations. To illustrate the concept, consider a string fixed at its two ends, and these two fixation points are as far apart as the natural length of the string. In this instance, there is no strain in the string as it is at its natural or original length. It may be noted that the description is already becoming dependent on the experimenter to determine with reasonable certainty what constitutes a fair description of natural length as a string may very easily have different lengths at zero load

The left Cauchy-Green tensor is based on the deformation gradient tensor and is defined as: $B = F \cdot F^T$, which is a symmetric, one-point tensor defined in the current

configuration, independent of rigid body motion. The deformation gradient tensor explains the relationship between differential line segments in the current and reference configurations.

6.3 Equations to Be Solved

In structural FEM, the general equation being solved is K(u)U=F, where K is the stiffness matrix, u is displacement, and F is force. In an implicit function, the dependent is not given explicitly in terms of the independent variable – such is the case here. The equation is nonlinear because of the way K depends on displacement. This nonlinearity requires special solving techniques. For this study, and for many applications, the Newton-Raphson approach is useful. With the Newton-Raphson approach an initialization is done (F=0, x=X, R=0), where R is the residual and X is the initial position. There is then looping over the load increments. First establishing ΔF (the load increment), then setting $F=F+\Delta F$, and $R=R-\Delta F$, then while abs(R)/abs(F) > tolerance, cycling through solving Ku=-R, updating x=x+u, finding F (external forces), b (left Cauchy green tensor), and sigma for each element, finding T (internal forces) and finally finding R=T-F. After below tolerance value, the load is incremented and cycling repeated as necessary to achieve tolerances and total load. While not an exact solution, the accuracy of the solution is controlled by the tolerance value and the element sizes. The convergence rate identifies how fast the residual norm shrinks relative to iteration number [85].

Boundary conditions are necessary for problem characterization and solvability. When solving the above equation, boundary conditions come in through restrictions on F

and u. The restrictions limit the values of F and u, and they must typically be accounted for directly or enforced through a penalty method.

6.4 Method of Solution

There are a variety of methods for solving the resulting nonlinear equations. Newton-Raphson, Modified Newton-Raphson, and direct substitution are methods supported by MSC.Marc ([86] - pg 739). For the type of analyses conducted here, MSC.Marc uses the tangent modulus method which requires a convergence tolerance as well as maximum and minimum recycle limits. In the materials used for this study, their properties are considered to be time independent.

The Newton-Raphson procedure can be derived using a Taylor series expansion about a previous solution/value, then neglecting higher order terms and setting the residual of the next value to zero. The resulting increment is calculated from $\{\delta U\} = -[K_T]^{-1}\{R\}$, where R is the residual ($R(u) = K(u) \cdot u - F$). K_T is the slope of the curve R(u) at u and is defined as $K_T = \left.\frac{\partial R}{\partial u}\right|_{u^{(r-1)}}$. As the procedure is cycled, the residual (representing the difference between external and internal nodal forces) is reduced to zero or close enough as defined by a user specified tolerance value.

7. AXISYMMETRIC MODELING OF AAA

Axisymmetric and other idealized geometry models of AAA provide a framework for analyzing variations in boundary conditions and material properties. The models analyzed look at the role of graft properties, thrombus, and the impact of starting with deformed geometry as the initial, unloaded configuration.

7.1 Axisymmetric Background

Some of the first FEM models of AAA were axisymmetric models and showed the potential of FEM to identify regions of high stress and potential rupture. The early models used linear elastic material properties and small strain FEM codes. Stringfellow et al. showed that wall thickness and geometry are important to maximum diameter, though their work was limited by sharp junctions between normal and aneurysmal aorta in their models [87]. They predicted that with improved imaging, patient-specific FEM would become a clinical tool. Using a supercomputer of the time and different material properties, Mower et al. showed AAA stress increasing with increasing diameter and decreasing with increasing thickness. They found that the law of Laplace was not good enough to estimate stress because, in part, it provided only average information. However, in addition to the limitations of simplistic material properties, they did not determine how stress related to shape since diameter and curvature were varied simultaneously [88]. Inzoli et al. incorporated thrombus (0.2 MPa) and plaque (20 MPa) into axisymmetric models of aneurysms (2 MPa) utilizing different material properties for the constituents – showing plaque increase stress concentrations and thrombus caused decreases in peak stress by up to 30% [89]. Utilizing a slightly different

approach including normalized stress equations and thin shells, Elger et al, in 1996, showed how shape (curvature) influences stress distribution [90]. Mower et al. 1997 looked at a range of material properties for wall and thrombus in their models and saw thrombus will reduce stress, but emphasized that it was unwise to draw quantitative values from their study because of its limitations in material models and other parameters [91].

In 1998, the move away from axisymmetric to other idealized geometries continued with the work of Vorp et al. They showed, using linear elastic small strain models, that increased diameter or asymmetry increased wall stress. They also found that the location of maximum stress, either at the inflection points or midsection, moves with expansion [66].

In 1999, the move to more complicated material models, capable of large deformations began with a Thubrikar et al. paper, which used a 5 parameter hyperelastic model to look at rupture direction preference. Their models incorporated no thrombus and semi-sharp corners, and they showed rupture to be a function of longitudinal stress, not circumferential [92]. Even more complicated material models, in axisymmetric modeling, were utilized in the work by Watton et al. which had properties dependent upon stretch and degradation over time. Their complex work assumed many rates and parameters, considering the evolution of AAA and their remodeling, but did not address why aneurysms develop preferentially in the aorta [56].

Axisymmetric models allow investigation of parameter variation without the complications of patient-specific geometry. They have established the potential of

thrombus to reduce stress and the inadequacy of law of Laplace to calculate stress in aneurysms, as well as emphasized the importance of material properties.

7.2 Modeling Methods

The axisymmetric geometry was based on the one-eighth of an aneurysm model used by Vorp and Raghavan in their 1998 paper [66]. The length is 60 mm, with a straight portion of 13 mm. The maximum outer radius is 30mm (corresponding to a diameter of 6 cm); the wall thickness is a uniform 1.5 mm throughout the aneurysm, neck, and iliac arteries. The endograft inner radius is 12 mm, and thickness of 1 mm in the baseline model. The model can be adjusted to represent instance of different levels of over-sizing between the endograft and the neck of the aneurysm. The figure below shows the general shape of the model in the unloaded configuration with the red parts representing the vessel wall, yellow the thrombus, and white the endograft (Figure 20). The endograft is outside the aortic wall proximally because it is oversized by 20% to the systolic diameter of the vessel neck.

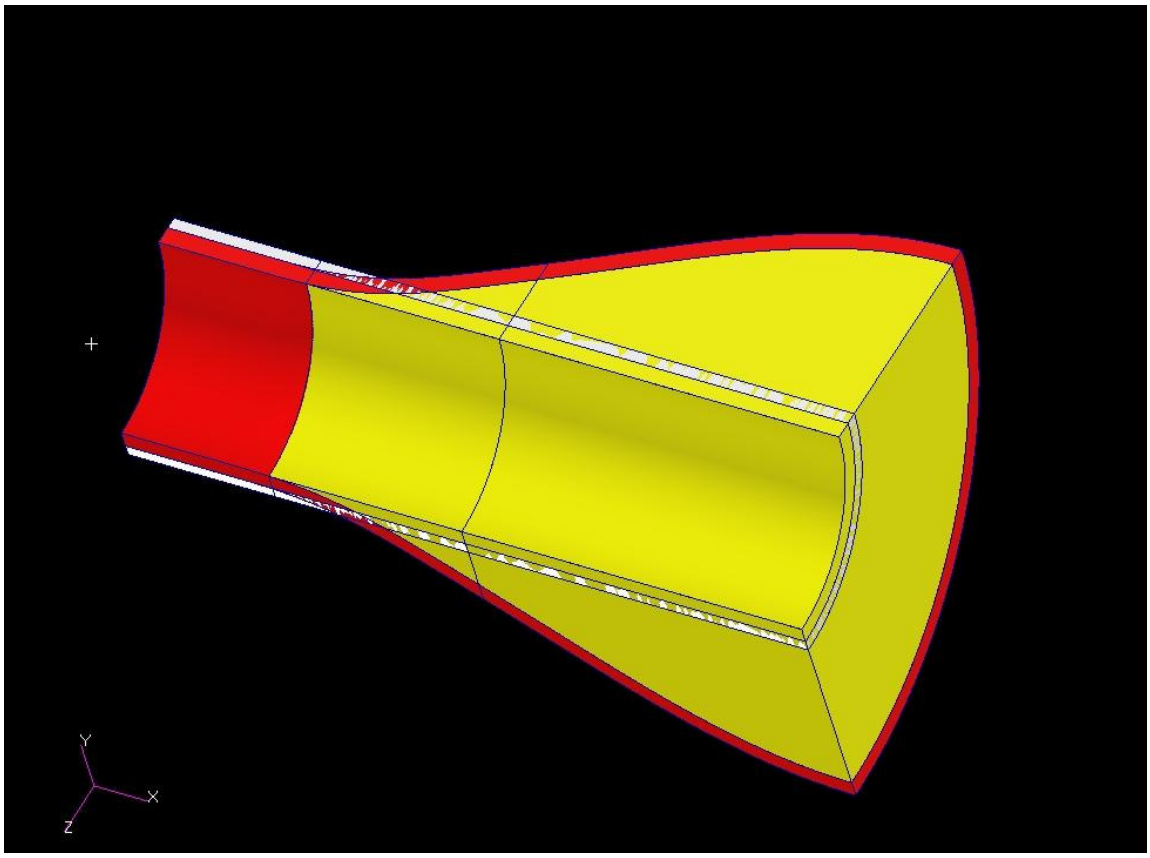

Figure 20. One-eighth model of AAA showing components

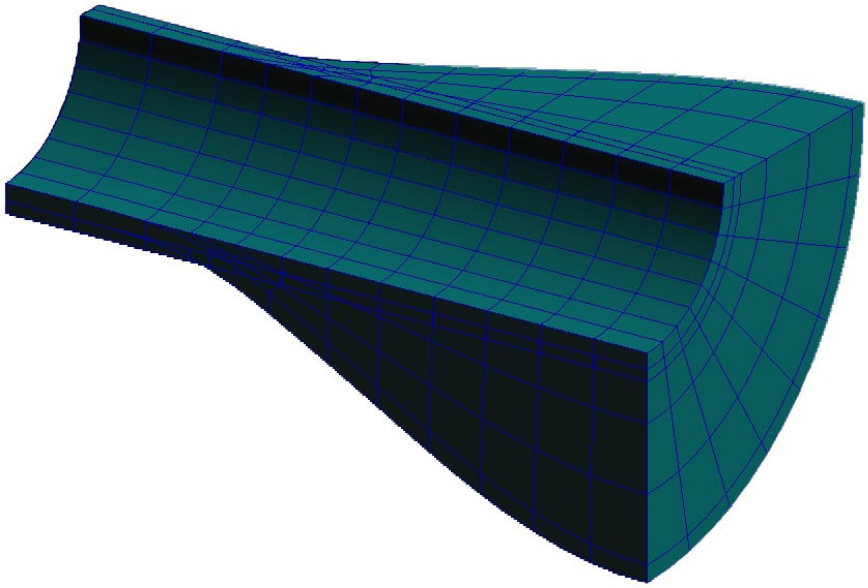

Figure 21. One-eighth model of AAA showing mesh

The mesh density was adjusted to so that models showed a difference in maximum principal stress of less than 1% when the mesh density was doubled. These denser models were relatively easy to run because of the axisymmetric nature of the geometry. There were issues in the meshing of the thrombus region due to the thinness of thrombus in the neck region. This thinness results in unstable and poorly shaped elements.

Models were run with a variation of endograft properties and conditions to see how the stresses changed. The first variations in models involved using the different moduli for compression and tension for the endograft. These moduli are not the same as

those in section 4.4 because these models were run first. The next part varied was the amount of axial tension applied to the model to reflect different levels of tethering. Also varied was the pressure internal to the system, to see the differing impact of diastolic/systolic/mean pressures on the stresses and final equilibrium position.

A series of steps are taken in MSC.Patran to define the model before solving it with MSC.Marc. Initially the geometry is defined through a CAD like drawing procedure. Subsequently meshing of the resulting solids is conducted in a semi-automated way. The mesh is created by the application of seeds to each key edge to insure matching between surfaces of different solids. Then the meshes are made equivalent at the points of intersection. The equivalence process removes nodes that are duplicated between solids. This allows the solids to be joined in an absolute way. Alternatively, instead of creating multiple solids, it is possible to assign properties to the elements themselves instead of the solids. This is problematic in cases where the mesh will be subsequently refined, as the information separating the groups is lost if there is no the underlying geometric distinction between parts.

After the mesh has been fully defined, the loads and boundary conditions are defined. Again, in this case, the boundary conditions were zero displacement in the out of plane motion of the side faces of all components and fixed displacement on the surfaces of the end faces. These fixed displacements reflected a model of tethering and were varied between values that produced a no axial stretch to a stretch of 1.6. These stretch values were chosen to simulate a wide potential range of axial tethering from an unloaded configuration. It is noteworthy that these stretches were applied at the ends of

the model, and as a result the model would stretch further in regions with less material, where it was in a sense weaker. Pressures were defined on the interior and applied either to the thrombus or to the wall, as well as the graft if present. The application of pressures to the various parts allowed for pushing the different parts out of the way temporarily so that contact could occur smoothly and then pressure reduced to physiologically relevant values. The graft is initially oversized compared to the vessel, and pressures/radial displacement boundary conditions need to be used so that it can be fit within the wall. The loads and boundary conditions needed to be set into load steps before being useful. The load steps determine what set of loads and boundary conditions will be used in a load step increment. These increments are assigned to job steps which govern the progression of the job and the series of loadings. For instance, a different step is used for the overexpansion of the wall so that the graft is on the inside, another step for the reduction in pressures so contact is made, and finally another reduction/relocation of pressure so that the loading reflects the physiologic situation. It is noteworthy that the job step specification process includes the specifying of additional input governing how the computations are to be carried out and what results are of interest.

In the axisymmetric models run for this study, software defaults were used except that the analyses were run for large displacement with large strain, constant dilatation was unchecked, and a constant load increment was used instead of an adaptive. The constant load increment makes for a more stable contact analysis. The large strain, large displacement analysis allows for the nonlinear material behavior to be accurately

modeled. Output changes included requesting additional information on contact bodies to determine which side was making the contact for troubleshooting runs and reporting of Cauchy stress, as well as writing results for only every several load sub-increments. Jobs for axisymmetric models were generally run on a Windows XP PC with dual 2.8 GHz processors and 2GB of RAM. The writing of results for only every several load sub-increments reduces the amount of data in the result files, which were unwieldy when lots of nodes were present.

There were also a small number of models run to look at the impact of starting with deformed geometry for the attachment zones, particularly the aneurysm neck. These models used a Young's Modulus of 1.0 MPa and Poisson ratio of 0.3 for the endograft. The wall properties were of C_{01}=174,000 and C_{20}=1,881,000 Pa [8]. They were begun with a quarter model of full cylinder, with inner radius of 12 mm and thickness of 2 mm. A graft was implanted with an inner radius of 14.4776 mm, 1 mm thick wall; these model dimensions were representative of over-sizing by 20% outer radius of graft to systolic inner radius. The load steps of the FEM included over-pressurizing the cylinder, activating contact, and removing pressure to allow diameter reduce down to equilibrium with no pressure.

7.3 Material Model Implementation

The isotropic properties and strain energy functions described by Raghavan and Vorp were used for the vessel wall and thrombus [8, 9]. The thrombus strain energy function, $W = C_1(I_2 - 3) + C_2(I_2 - 3)^2$ with C_1 = 26,000 Pa, and C_2 = 26,000 Pa, could not be used directly in MSC.Marc/Patran. The closest model available was the of

James-Green-Simpson full third order invariant based strain energy density function:

$$W = C_{10}(I_1 - 3) + C_{01}(I_2 - 3) + C_{11}(I_1 - 3)(I_2 - 3) + C_{20}(I_1 - 3)^2 + C_{30}(I_1 - 3)^3$$

with C_{01} = 26,000 Pa and C_{11} = 26,000 Pa – all other constants set to zero. The difference is in the $C_{11}(I_1 - 3)(I_2 - 3)$ term being utilized in place of a $C_{02}(I_2 - 3)^2$ term. A comparison of the material models was done in Matlab, simulating uniaxial and planar equibiaxial testing (Figure 22 and Figure 23).

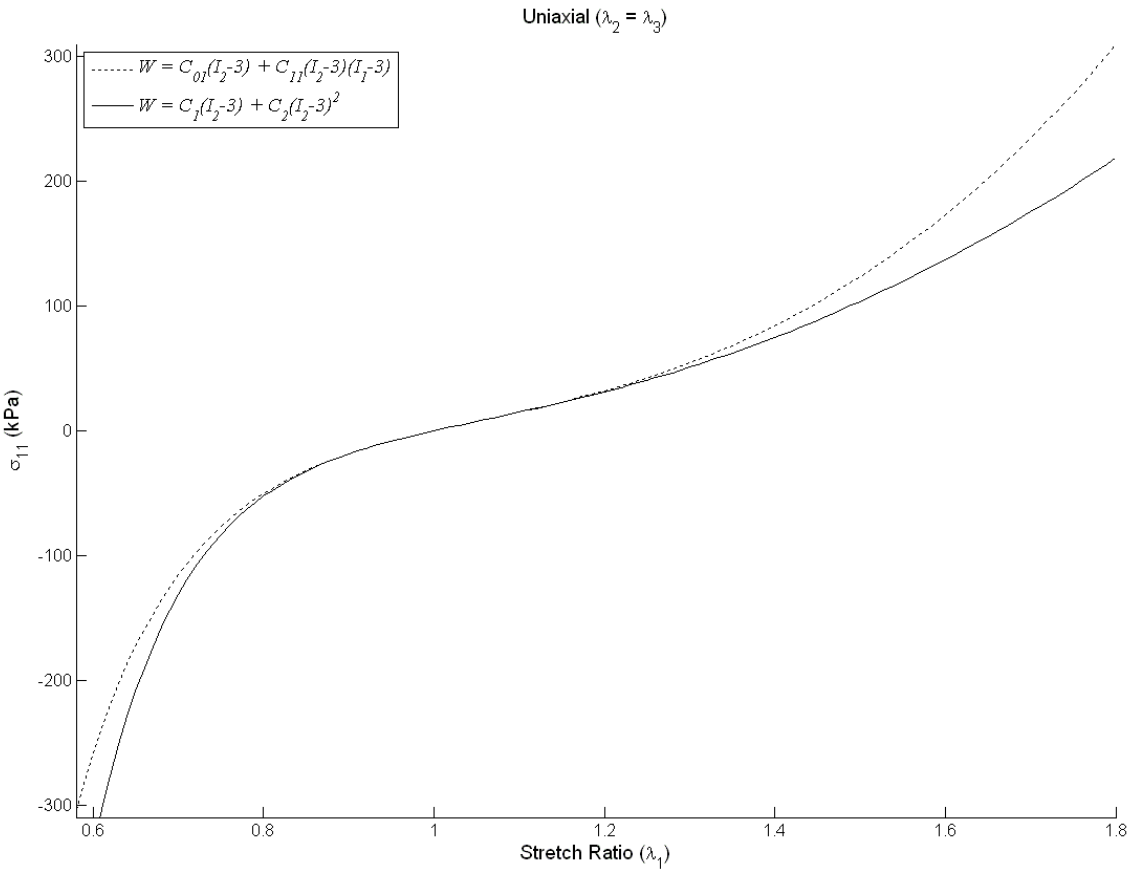

Figure 22. Figure showing material responses of Vorp thrombus (solid line) vs. Marc (dotted line).

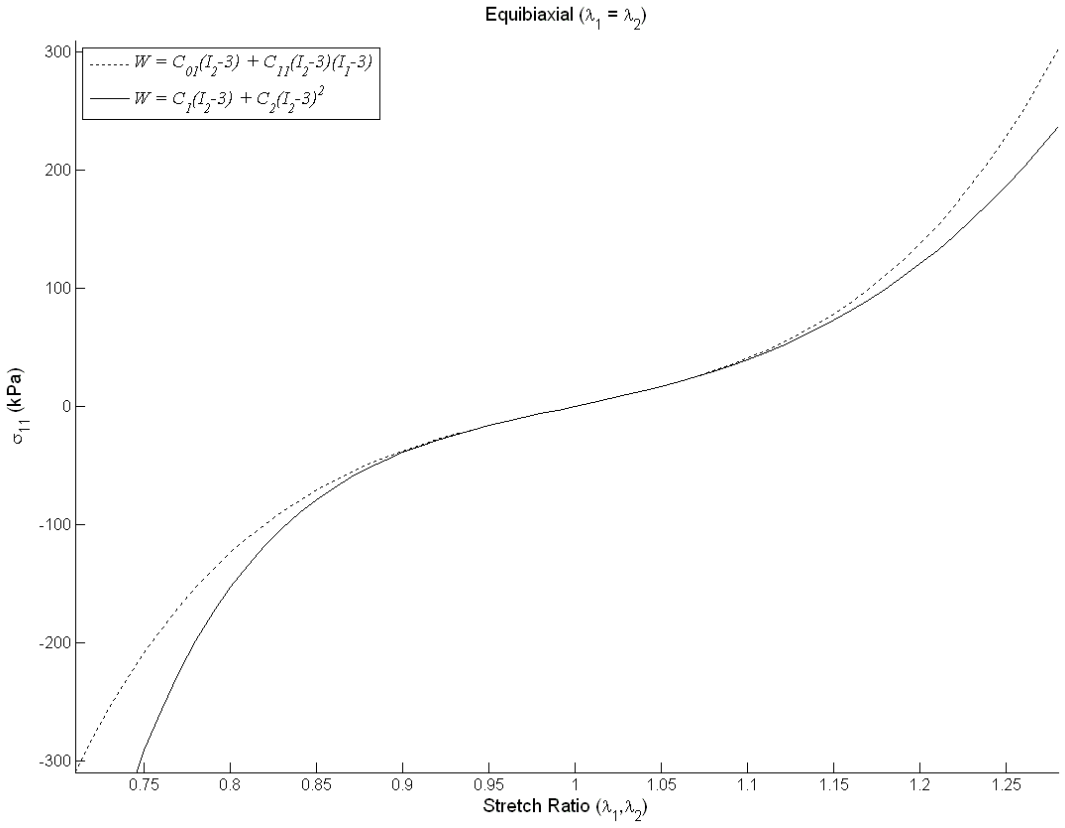

Figure 23. Comparison of Vorp (solid line) vs. Marc (dotted line) equibiaxial simulations of thrombus material. Component of Cauchy stress in kPa is shown over a narrower range of stretch ratios (same stress limits for Marc line of implementation).

This substitution of one form for the other results in similar stresses over the range of stretch ratios the SEDF was originally fit to (up to 1.2) before separation is large.

The SEDF used for the aortic wall in the models described in this dissertation was $W = \alpha(I_B - 3) + \beta(I_B - 3)^2$ with the mean values reported of 174 kPa and 1881 kPa for alpha and beta, respectively, from Raghavan and Vorp in 2000 [8].

7.4 Axisymmetric Results

7.4.1 Endograft Properties

The results indicated that softer endograft properties reduce stress and removing thrombus makes the wall distend more in response to systolic pressure (Table 4 and Table 5). Images taken of two of the results are shown as well to illustrate the distribution of stresses and location of peaks near the junction of thrombus, endograft, and wall (Figure 24 and Figure 25).

Table 4. Results of axisymmetric modeling with varying endograft properties.

Model Name (1st letter for compression part, 2nd letter for tension part)	Modulus compression part of endograft (MPa)	Modulus tension part of endograft (MPa)	Maximum von Mises stress (kPa)	Minimum von Mises stress (kPa)	Max displacement magnitude (mm)	Radial displacement of graft (mm) Maximum and Minimum
LH	4	90	1130 (in graft) 661 at bend in wall	6.90	2.41	-0.00491, -0.893
HL	90	4	1200 (in "normal" wall)	6.59	2.39	-0.0983, -0.355
HH	90	90	1200 (in "normal" wall)	6.88	2.41	-0.00281, -0.119
LL	4	4	533 (in "normal" wall)	6.64	2.32	-0.0985 -0.887

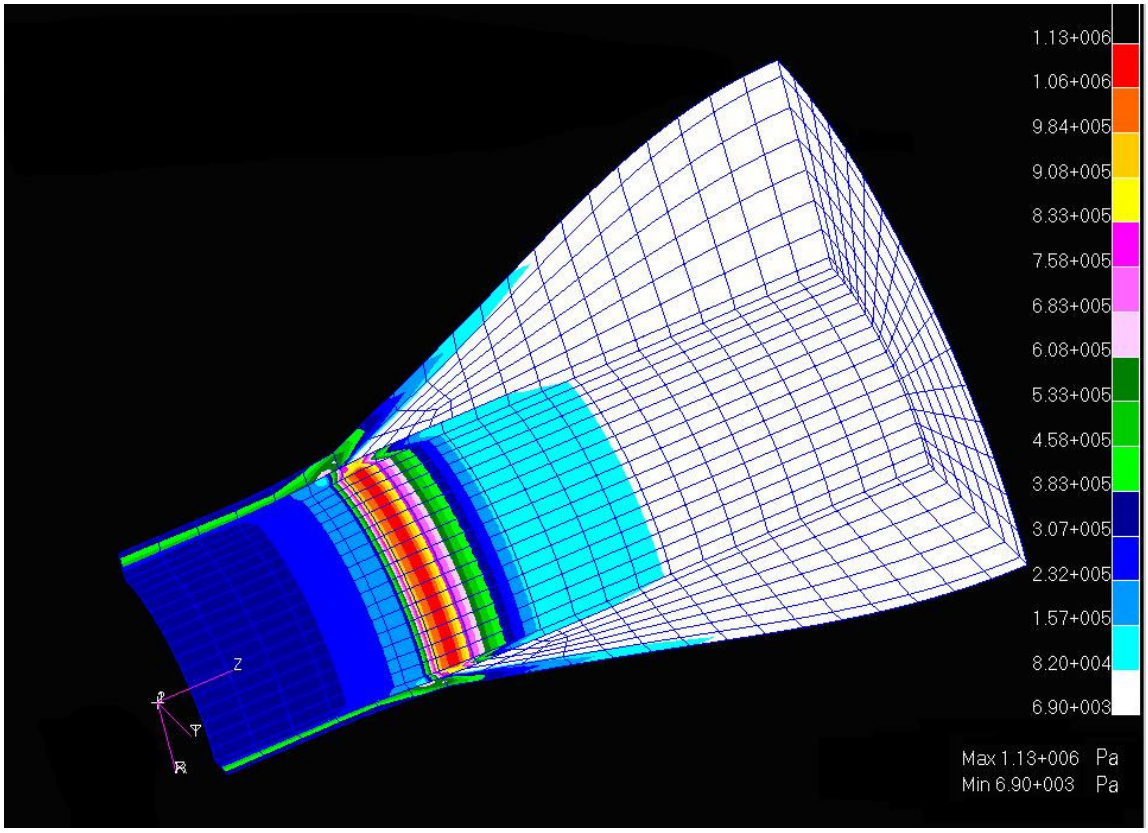

Figure 24. Model LH with elements showing von Mises stresses.

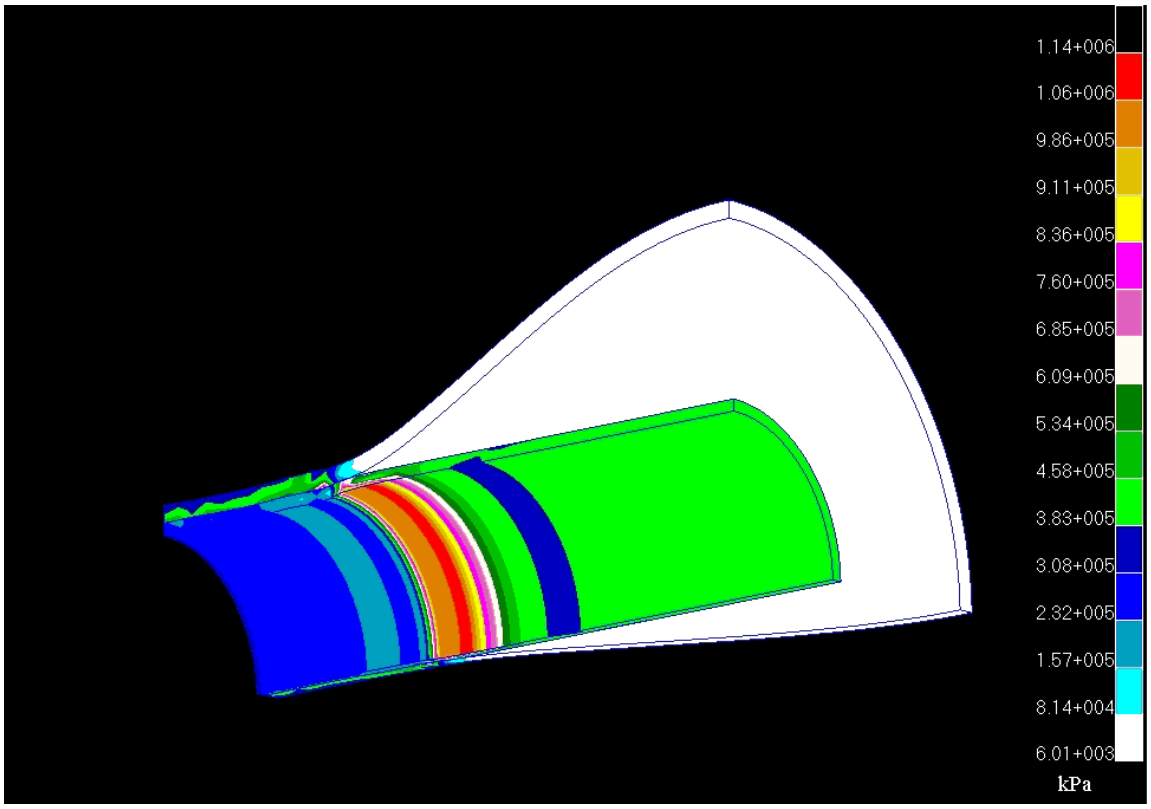

Figure 25. Von Mises stress map of oversized endograft inside axisymmetric aneurysm model.

Table 5. Results of axisymmetric modeling with varying endograft properties and no thrombus are shown indicating influence of endograft properties without thrombus presence. G and W indicate values of graft and wall components, respectively.

Modulus compression part of endograft	Modulus tension part of endograft	Maximum von Mises stress (kPa)	Minimum von Mises stress (kPa)	Max displacement magnitude (mm)	Max and min radial displacement of graft (mm)
4 MPa	90 MPa	1140 G 934 W	167 G 6.01 W	0.794 G 2.64 W	0.0654 -0.791
90 MPa	4 MPa	1380 G 1570 W	66.3 G 8.42 W	0.584 G 2.99 W	0.575 -0.124

7.4.2 Thrombus Implementation

A comparison of the modified and direct implementations of thrombus strain energy functions indicates that the difference between implementations difference is < 1% in peak von Mises stress and < 0.15% in maximum displacement. The minimum displacement difference between implementations is larger (> 2.5%), but the minimum displacement value is small compared to the dimensions of the model. The results are shown in the figure and table below (Figure 26 and Table 6).

Table 6. Results from Abaqus models implementing directly and indirectly the thrombus strain energy function.

	$W = C_{01}(II_B - 3) + C_{11}(I_B - 3)(II_B - 3)$ (using Marc capable, indirect implementation)	$W = C_1(II_B - 3) + C_2(II_B - 3)^2$ (using Abaqus based, direct implementation)	% difference from direct
Maximum displacement (mm)	0.3582 G 3.013 W	0.3587 G 3.010 W	0.14% 0.10%
Minimum displacement (mm)	0.04143 G 0.9196 W	0.04195 G 0.94241 W	1.24% 2.42%
Maximum von Mises stress (kPa)	1167 G 1405 W	1169 G 1391 W	0.17% -1.0%
Minimum von Mises stress (kPa)	1.358e5 G 7.725e3 W	1.370e5 G 7.706e3 W	0.88% -0.25%

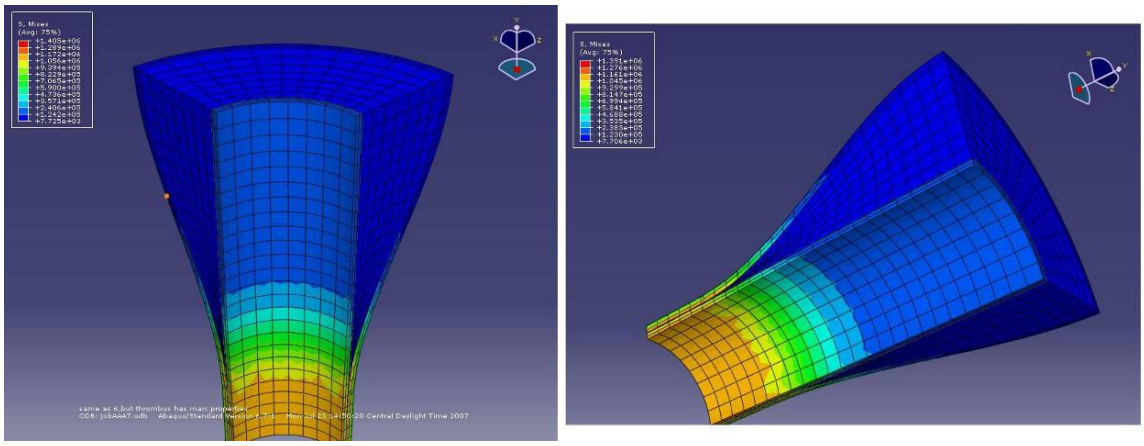

Figure 26. Stress maps of von Mises stress for indirect (left) and direct (right) implementations of thrombus material model showing similarity of results.

The results of the models to look at neck configuration are shown below (Table 7).

Table 7. Comparison of neck pressurization effects with an implanted endograft.

Vessel – Starting Geometry		Graft – Starting Geometry		Pressure Applied	Von Mises Stress		Vessel - Final Geometry	
					Maximum	Minimum		
Ri (mm)	Ro (mm)	Ri (mm)	Ro (mm)	mmHg	(kPa)	(kPa)	ri (mm)	ro (mm)
12	14	-	-	120	127	81.6	12.898	14.777
12	14	14.4776	15.4776	0	140	89	12.956	14.827
12	14	14.4776	15.4776	120	254	150	13.341	15.165
13.34	15.165	12.34	13.34	120	94.0	66.9	14.158	15.889

The outcomes from various starting configurations indicate the effect of an oversize endograft is comparable to pressurizing by 16 kPa (120 mmHg). The stresses from the most realistic case, with an oversized graft implanted and further pressurized, starting with unloaded vessel and endograft geometries, result in stresses nearly twice as high as the graft alone or pressure alone. Starting with a deformed configuration including the endograft and vessel wall already at equilibrium geometries (though without stress), gives stresses lower than all the other cases. This result indicates that the models are underestimating the stress levels within the neck. These results, using just one endograft stiffness modulus do not address the full range of issues.

7.5 Axisymmetric Discussion

The axisymmetric models show that the difference in endograft properties makes a substantial difference in the amount of stress within the wall in the neck-like region – the higher stiffness graft causing more than twice the maximum principal stress in comparison to the lower stiffness graft (HH vs. LL). The presence of thrombus reduces

displacement of the graft in the sac region by 0.2 mm for the higher stiffness graft model and 0.6 mm for the lower stiffness graft model.

Overall, the axisymmetric models indicate that graft properties have an effect on the stress within the aneurysm wall, with higher stiffness graft reducing the pressure felt on the sac, but increasing the pressure felt on the aneurysm neck. The method of implementation of the thrombus material model does not affect results substantially.

The implication of the similarity between the material models implementations indicates that there is covariance amongst the invariants, at least with regard to this test. This has been previously observed and commented on by Criscione [93]. However, this covariance can also be used to simplify the modeling methods used, allowing for usage of the 2 constants within the 3rd order James-Green-Simpson material model so that a user subroutine is not required. This method, of course, is only adequate if the stretch ratios do not exceed the range of validity.

7.6 Axisymmetric Conclusion

The usage of pressurized geometry as a starting point leads to an underestimation of stresses in the vessel wall by nearly 160 kPa, with the prediction less than half of the "true" value. This underestimation highlights the need for caution in interpreting the results of models run with already deformed geometries subjected to initial loads.

8. PATIENT-SPECIFIC MODELING OF EVAR TREATED AAA

8.1 Patient-specific Background

Historically, patient-specific modeling of AAA has been used to attempt to quantify the rupture risk a given patient has, particularly with smaller aneurysms, in order to differentiate who needs to undergo the risk of surgery to avoid the risks of acute rupture (death or emergency repair) [65]. The general trend of small diameter aneurysms rupturing less often than large aneurysms is not adequate because some small aneurysms rupture and some large do not [5].

The work by Thubrikar et al. was one of the first finite element analysis studies based upon a patient's CT data; though it was limited to one patient and ignored thrombus on the basis of authors' unreported data that it does not reduce wall stress significantly. Their study was also parametric in that they analyzed cases utilizing the highest and lowest thicknesses throughout the aneurysm because of variations in their thickness measurements. The modeling was limited by the usage of symmetry and linear elastic properties throughout; it was concluded that an increase in wall thickness (uniformly) reduces stress and that an inflation pressure raises wall stress. The authors also stated that stress distribution and orientation were affected by tethering [65].

A much more complex analysis, in terms of reconstruction technique and material properties, of patient-specific models of AAA was done recently by Vande Geest et al. It incorporated an anisotropic model into analyses of aneurysms that either subsequently ruptured or not (within 1 year of CT scan). Although they did not see statistically significant results, the trends of their small (9 ruptured, 5 non-ruptured)

sample size trended towards the anisotropic model being better at distinguishing results [67].

Another study by Li et al. looked at 20 AAA to determine effect of calcification on peak wall stress within patient-specific models. Their results showed that calcification increases wall stress by its presence. However, the location, and not net volume, plays the important role in peak wall stress value modulation [71].

In a study presented in Biomedical Engineering Online, Doyle et al. looked at the differences resulting from varying material model assumptions. They used linear and nonlinear properties with and without thrombus, as well as varying the amount of smoothing, to see how stress distributions and values were affected in one patient-specific based model. The results indicated that shell elements could possibly lead to inaccurate results. They also found that the thrombus and nonlinear properties are likely necessary for accurate stress distributions and values, with their most complex model differing by more than 55% from a simpler one [82].

The purpose of patient-specific modeling in this dissertation is slightly different in aim. The goal here is to see how AAA responds over time to treatment by endograft because the response to treatment can differ – some AAA shrink, remain stable, or (rarely) grow. To this end, patient-specific modeling was done to calculate stress induced in the wall at various time points and to quantify shape.

8.2 Patient-specific Methods

In the patient-specific models, it was desired to determine the stresses within the wall at various time points in patients treated with endografts for AAA. It was of

interest to look at stresses before implantation and after implantation, both short and long term because of the temporal nature of shape change and the requirement of continued follow-up in patients with endografts. To do this, the reconstruction method described in Chapter V was used to take CT scans of two patients treated at Scott & White Hospital in Temple, TX that had scans present from all time points of interest (pre-treatment, early follow-up, and late follow-up) and similar backgrounds. The purpose of similar backgrounds was the idea that the reconstructions might also be able to provide some insight into why the aneurysm sac shrunk notably in one patient but did not in another, after otherwise apparently successful treatment in apparently similar patients.

8.2.1 Model Parameter Variation

The patient-specific models were analyzed with a variety of conditions (differing graft properties, pressures, pressurization surfaces, and with and without thrombus) so that the relative importance of the condition's specificity could be determined. A range of graft properties was used for all cases that covered the range seen in graft experiments and an order of magnitude larger and smaller for some cases. Since endografts have different properties in tension vs. compression, for some analyses the properties of the graft were specified as a combination - based upon direction of diameter change seen in follow-up CT scans from the nominal value specified by the manufacturer. Models of pre-treatment AAA were run, with and without thrombus, to illustrate the role of thrombus since it is disputed in the literature. Also, models at all time points were run at systolic (16 kPa) and diastolic (10.667 kPa) pressures. In pre-treatment models, the

pressure load was applied either to the lumen or to the interior of the wall directly since pressure close to the wall has been found unreduced in untreated AAA despite the presence of thrombus and was purported to influence model accuracy.

These models were all run with the combination properties for the endografts where the endograft had properties of 1.0 MPa and 10.0 MPa, in regions of apparent compression and tension, respectively unless noted otherwise.

8.2.2 Model Analyses

The analyses of the models were based on stress in addition to the shape quantifications because of stress's likely role in reshaping the AAA and in AAA rupture risk. Average stress values of entire models wall nodes were used to compare the effects of different conditions. The average was calculated by summing the von Mises stress values of each node and dividing by the total number of nodes in the wall. This method would have been biased by areas of differing node densities; however, node and element densities are primarily based upon the underlying image resolution and therefore generally uniform throughout for these models. The average values of stress, though perhaps robust, cannot be relied upon for statistical significance for differentiating between stable and shrinkage because the sample size of each group is one. The results here merely point towards areas of greater study and potential interest, and they illustrate the development (and some limitations) of a technique to acquire results from a larger sample that could be used to test significance and confirm apparent trends.

Peak von Mises stresses were determined for the set of models combining graft properties by inspection of the model results in MSC.Patran. Unplotting all elements

except those of the wall left maximum and minimum values to be determined only from the vessel wall nodes. Wall elements from the axial boundaries of the model were unplotted if they exhibited highest stress values so that a number unaffected by edge effects to would be shown. The locations and values of the peak von Mises stresses were recorded. Histograms of von Mises stresses were utilized to see the distributions of stresses within some of the models. The histograms, based on all nodal values, indicated that the values of higher stresses were limited to very few nodes in the follow-up models. Histograms, peak and average stresses were recalculated without small percentages of the highest nodal values for some models.

Von Mises stresses are reported throughout, but were found to be reflective of maximum principal stress values. The differences in averages between von Mises and maximum principal were within 10% of each other for all models. The reporting of von Mises stress should not be construed to be an assumption about the nature of failure of the aneurysm.

8.2.3 Graft Compression Location Identification

In order to determine the location of the circumferential tension or compression classifications for the stent graft, a review of the CT scans and surgical notes was undertaken in addition to the comparison of hydraulic diameters noted in Chapter V. To confirm that the dimensions of the endograft could be measured accurately on the CT scans, unaffected by pixelation or metal artifact, measurements using a digital caliper were done on the struts of an AneuRx sample device and compared with the dimensions measurable on the CT scan, since strut dimensions are unlikely to change drastically in

implantation. The dimensions measured with the calipers were a strut width of 0.3 mm and a thickness of 0.4 mm. The struts were rectangular in cross-section. The CT scan image in the figure below (Figure 27) below shows that the diameters measured across the struts were similar, the cross-sectional area of an ellipse of strut size matches to within the precision of the calculation (nearest tens of mm^2) although the cross sections are less sharply rectangular. The CT measurements were done within the DICOM viewer (eFilm Lite), which was included with the CT scans obtained from Scott & White. From these results, it is apparent that the dimensions of the graft shown by CT are close to the dimensions of the graft in reality.

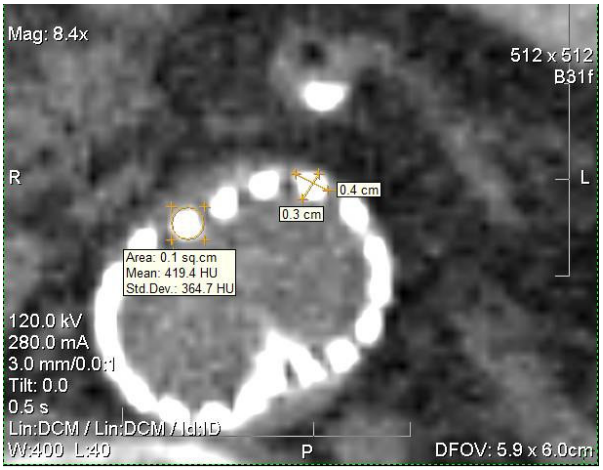

Figure 27. CT scan showing treated AAA and endograft, proximal to bifurcation, strut dimensions noted.

The neck of the aneurysm is used for endograft size selection. The measurements indicate that the diameter of this graft in this region is 26 mm (Figure 28). The minor axis is used because it is less susceptible to the error of diameter increase

resulting from the approximately cylindrical shape of the aorta not lying normal to the imaging plane. The image in the left part of the figure was taken at a slightly higher resolution both axially and spatially than the pre-operative image on the right. The image on the right shows that the measurement of a fitted ellipse to the adventitia of the aorta. The image on the left has measurements of diameters and areas. The original graft measured 28 mm in diameter according to the surgeon's notes. The reduction in diameter, as well as the smaller original area of the pre-op CT scan, indicates that the device is compression in this location.

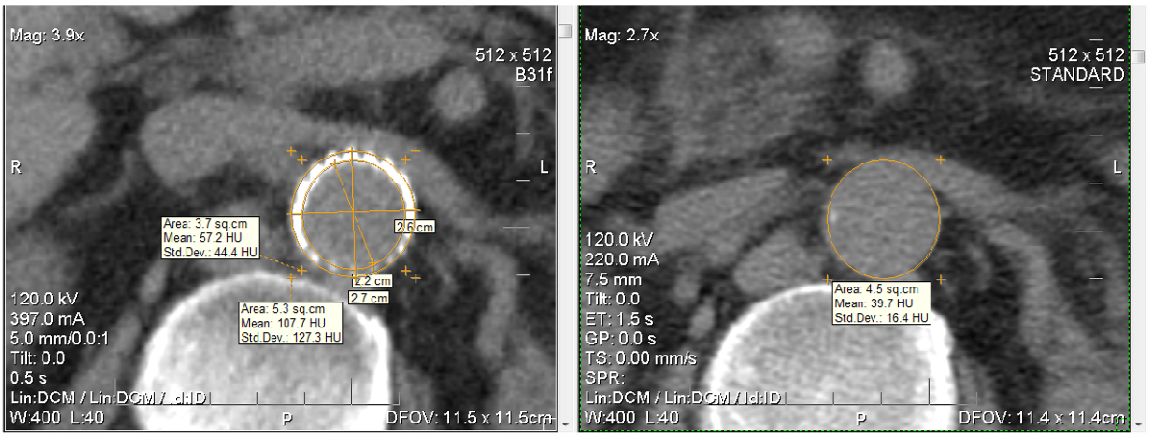

Figure 28. Figure showing post-op and pre-op CT scan slices at approximately the same proximal neck level.

The figure below shows the legs of the endograft and highlights the issue of the endograft not passing in a plane perpendicular to the imaging plane (Figure 29). The image on the right side was taken from an imaging study done nearly two years after that

of the left side. Diameter of the leg remains unchanged to within the accuracy of the measuring line from the program.

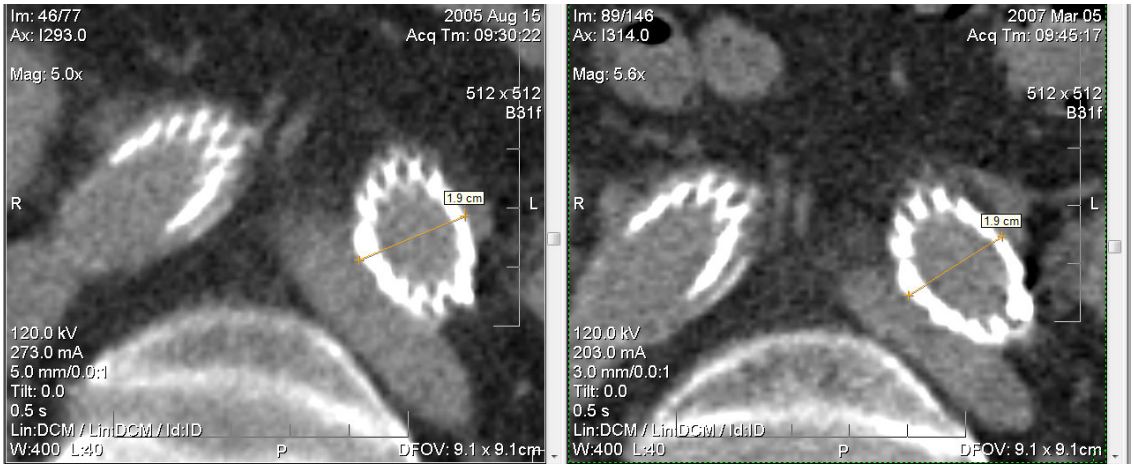

Figure 29. Endograft in iliac arteries at early and late follow-up.

The image (Figure 30) below is 1 cm proximal to that shown in the figure above (Figure 29). The legs of the graft are measured along their minor axes and can be compared with the pre-operative CT scan slice from two years prior. The white within the vessels on the right shows calcification and that the diameter appeared to be increased in the left iliac artery; although, the diameter is nearly unchanged or perhaps even reduced in the right iliac artery. Note that CT slices are viewed from the perspective of the feet, as if looking at slices from below.

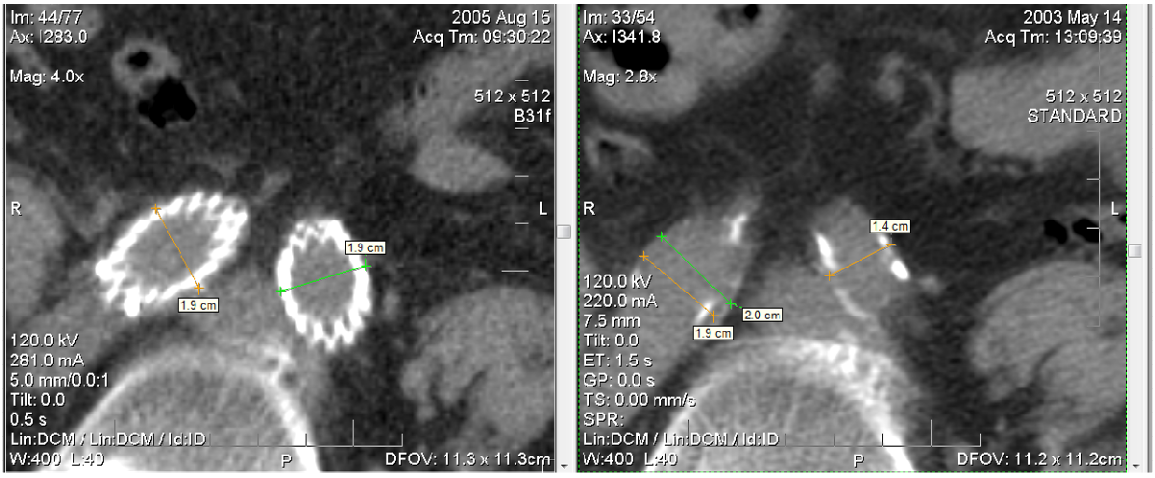

Figure 30. Figure showing the diameters of the treated arteries and those same arteries prior to endografting.

The following figure shows the portion of the graft at the mid-level of the aneurysm sac and that the graft appears expanded relative to nominal diameters (Figure 31). It indicates that the outer diameters of the legs of the graft are 1.9 cm in diameter and that the right leg branch is thicker because of the overlap between the inserted leg and the main body's leg. Full expansion of the diameters appears to be present because the outer diameter is the same for both legs despite the additional expansive force in the double walled section.

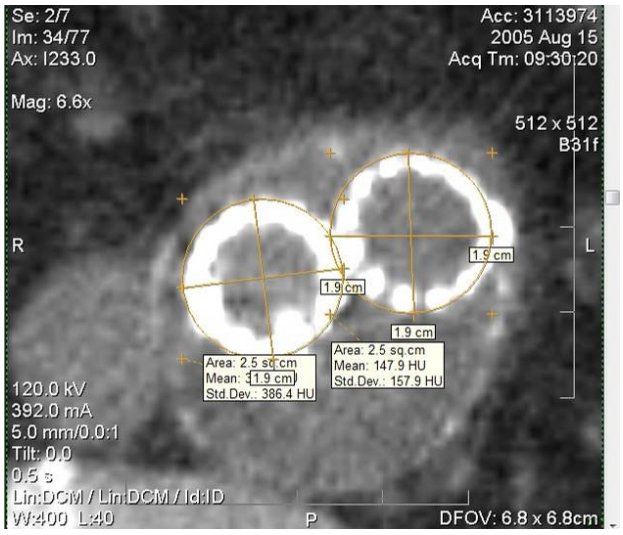

Figure 31. CT slice at mid-level of aneurysm sac.

In theory, the difference in diameter based upon the patient-specific reconstructions could show whether the endograft was under tension or compression as well or better than the CT images. In practice, this was very difficult to determine with confidence with either method. The differences in diameter are small (less than a few mm at most) and subject to noise from the rapidly changing centerline at the junction and bifurcation. It was also assumed that if the diameter was equal to nominal (within 0.1 mm), the graft was likely in tension as the response to tension is much stiffer than compression and less likely to be noticeable with the precision of the CT scans. The models were defined such that the neck and legs were in compression and the sac in tension with axial cutoffs chosen from hydraulic diameter calculations.

8.3 Patient-specific Results

The models indicate that endograft deployment reduces stress within the aneurysm wall, with the largest reductions seen occurring in the aneurysm sac. These

changes are concomitant with the size changes observed. The results of the patient-specific models were based on a series of CT scans covering pre-operation, early follow-up, and late follow-up time points for two patients – one AAA stable over time (patient A), the other reducing in size (patient B) – as defined originally by radiology reports (summarized in Table 8 and Table 9). The reports show maximum diameters for patient A (stable) were 44.5 mm at pre-treatment to 43.1 mm (-3.1%) at 24 months and then 41.3 mm (-7.2% net) at 43 months. Patient A was classified by clinicians as "essentially stable" because its volume over the same period went from 108.1 cc at pre-treatment to 111.3 cc (+3.0%) and 116.4 cc (+7.7% net) at early and late follow-ups, respectively. Patient B (shrink) showed maximum diameters of 62.3 mm at pre-treatment to 58.8 mm (-5.6%) at 20 months and 57.0 mm (-8.5% net) at 32 months. There was also a reduction in volume by from 179.8 cc to 156.9 cc (-12.7%) at early follow-up and to 146.4 cc (-18.6% net) at late follow-up.

Table 8. Maximum diameter as reported by Radiology over time course.

	Pre-treatment	Early follow-up	Late Follow-up
Patient A (stable)	44.5 mm	43.1 mm	41.3 mm
Patient B (shrink)	62.3 mm	58.8 mm	57.0 mm

Table 9. Volume as a reported by Radiology over time course.

	Pre-treatment	Early follow-up	Late Follow-up
Patient A (stable)	108.1 cc	111.3 cc	116.4 cc
Patient B (shrink)	179.8 cc	156.9 cc	146.4 cc

Overall, the results appear to indicate that stress is reduced most by graft implantation and the difference between early and late follow-up is relatively slight. The models also provide insight on modeling parameter importance – endograft properties appear to control magnitude of stress reduction, thrombus presence is important in pre-treatment models, and pressurization surface is relatively unimportant. The results also suggest that the lowest stresses are influential in shrinkage.

8.3.1 Effect of Endovascular Treatment

In a head to head comparison of stable (patient A) to shrinking (patient B) between pre-treatment and early follow-up, average von Mises stress values within the wall were apparently reduced by 87.3 kPa for patient A and by 59.3 kPa for patient B. See Table 10.

Table 10. Comparison of average von Mises stress amongst time points.

Time Point	Average von Mises Stress (kPa)	
	Patient A (stable)	Patient B (shrink)
Pre-treatment	116.7	80.9
Early Follow-Up	29.4	21.6
Late Follow-Up	28.2	25.3

These results indicate a 74.8% reduction of average stress within the wall from modeling the pre-operation situation to the early follow-up in the stable patient with the most realistic properties of the endograft modeled (combination of 1.0 and 10.0 MPa) at systolic pressure. In the patient with a shrinking aneurysm (patient B), the reduction was 73.3% between pre-treatment and early follow-up. The reduction in patient B (shrinking) also led to apparently lower average stress values than in patient A (stable) by 7.8 kPa (29.4 kPa vs. 21.6 kPa) at early follow-up and by 2.9 kPa (28.2 kPa vs. 25.3 kPa) at late follow-up. The average stress in patient B at late follow-up was slightly higher (3.7 kPa) than the average stress in patient B at early follow-up, with 21.6 kPa at early follow-up and 25.3 kPa at late follow-up. Patient A (stable), had an apparently higher pre-treatment stress than Patient B (shrink), despite a maximum diameter smaller 17.8 mm (62.3 vs. 44.5 mm, radiology measurements).

The disparities in average von Mises stress are reflective of the stress reductions occurring primarily in the sac region and not in the attachment zones of the endograft at the neck and legs (see Figure 32 and Figure 33 below for patient A (stable) and patient B (shrink), respectively).

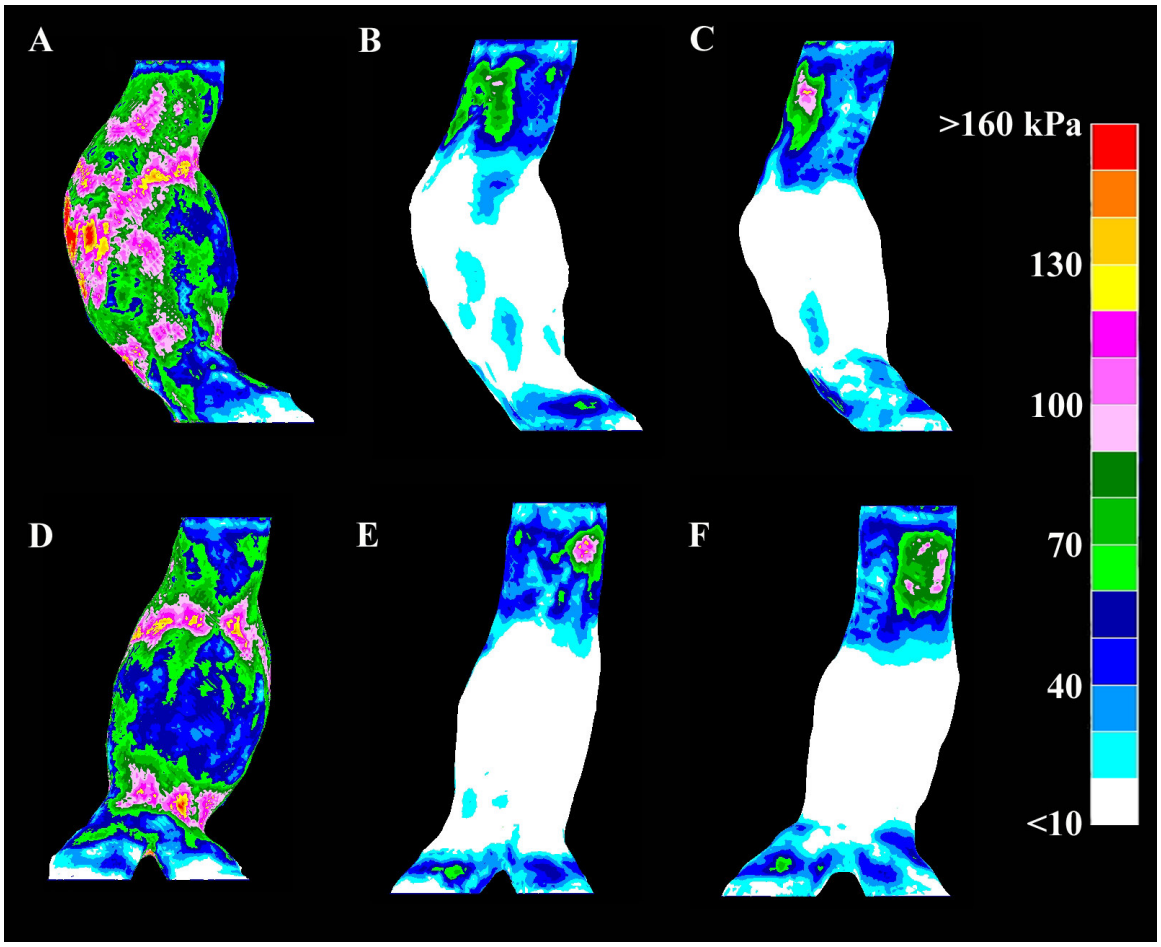

Figure 32. Map of von Mises stress on the surface of the AAA model of patient A (stable). A) lateral view of untreated, B) lateral view of early follow-up, C) lateral view of late follow-up, D) posterior view of untreated, E) posterior view of early follow-up, and F) posterior view of late follow-up.

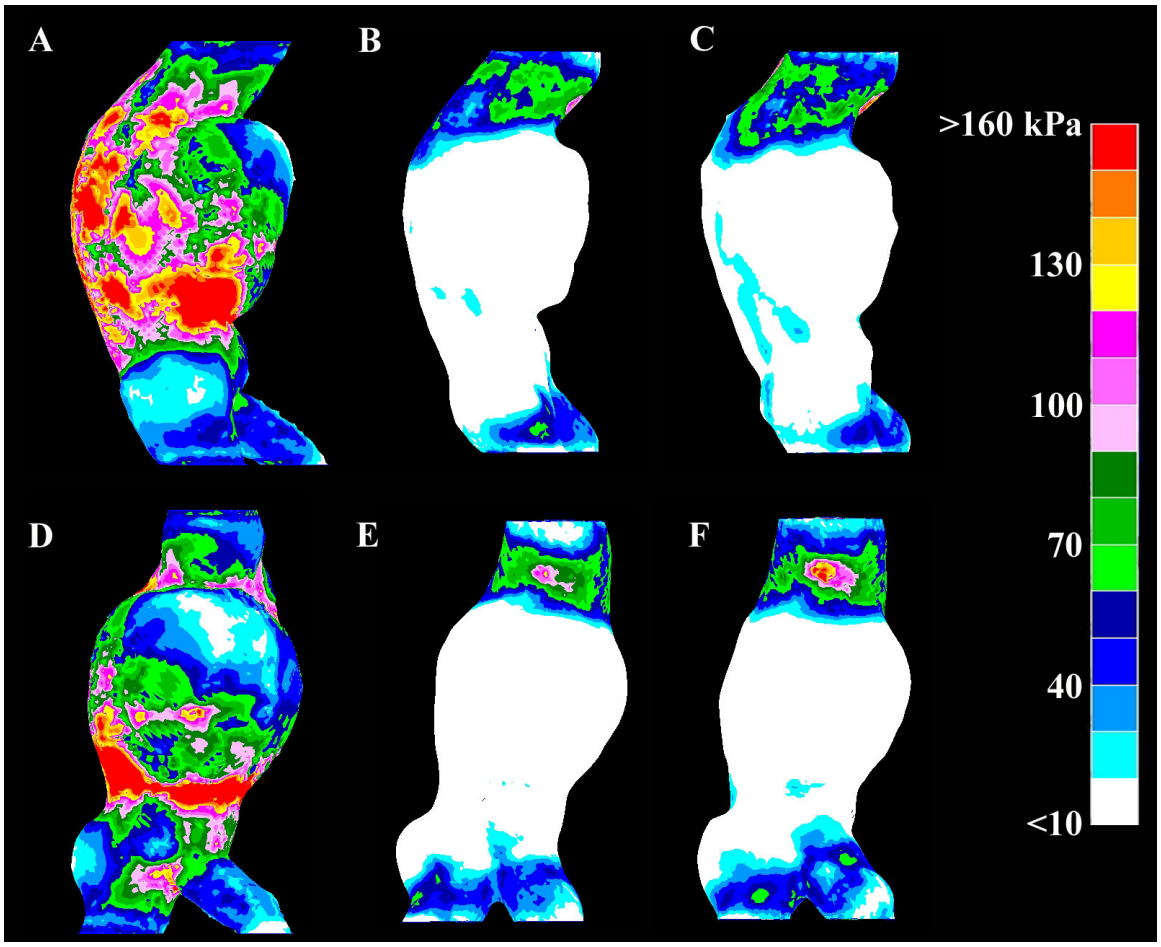

Figure 33. Maps of von Mises stress on the surface of the AAA model of patient B (shrink). A) lateral view of untreated, B) lateral view of early follow-up, C) lateral view of late follow-up, D) posterior view of untreated, E) posterior view of early follow-up, and F) posterior view of late follow-up.

Notably, the stresses within the aneurysm sac in patient A are highest on the anterior surface of the aneurysm sac in the pre-treatment model (Figure 32, A). Other areas of high stress (> 100 kPa) are present where the sac rejoins the smaller neck region and the bifurcation region (areas of pink in Figure 32, D). These regions are all markedly reduced (to less than 50 kPa) by endograft deployment in the treated models.

However, the neck region stresses are not so reduced by endograft deployment, exhibiting stresses that are within 20 kPa of the pre-treatment model. The distribution of stresses in the neck regions has shifted such that regions of higher stresses are no longer primarily laterally located but are now located on the anterior and posterior sides.

The overall patterns of stress in patient B models and patient A models are similar at similar time points. In patient B (shrink) pre-treatment, a similar pattern of stresses to that of patient A (stable) is present, with the sac region containing the highest stresses. However, the amount of area of very high stress (> 160 kPa) areas (red) is greater. Seemingly high stresses (> 100 kPa) are also focused on the anterior of the aneurysm and the region where the sac meets the bifurcation area. There is apparently less stress concentration in this model (patient B) at the region where neck meets aneurysm sac than in the patient A pre-treatment model (~80 kPa vs. ~120 kPa). In the treated models, the high (>100 kPa) regions of stress are located in the treated aneurysm neck on the posterior side. Also, the patient's right iliac artery has been brought more in-line with the aneurysm's orientation and alignment. The distribution of high stress regions in the neck region has also shifted in the treated models to be more proximal and anterior instead of lateral, though the disparity is even more pronounced than in patient A (stable) – compare Figure 33 D and Figure 33 F.

The areas of peak von Mises stress, identified away from edge elements, move from the sac to the attachment areas, primarily the aortic neck, in response to treatment throughout follow-up. This response can be seen from Figure 34 and Figure 35 which show areas of highest stress for patient A (stable) and patient B (shrink) – scales not

shown as they are unique to each model. In patient A models, the highest values of von Mises stress are on the anterior wall of the sac before treatment and are in the neck after treatment. In patient B models, the highest values of von Mises stress are found along the posterior base of the bulge of the aneurysm sac before treatment and on the anterior of the neck after treatment.

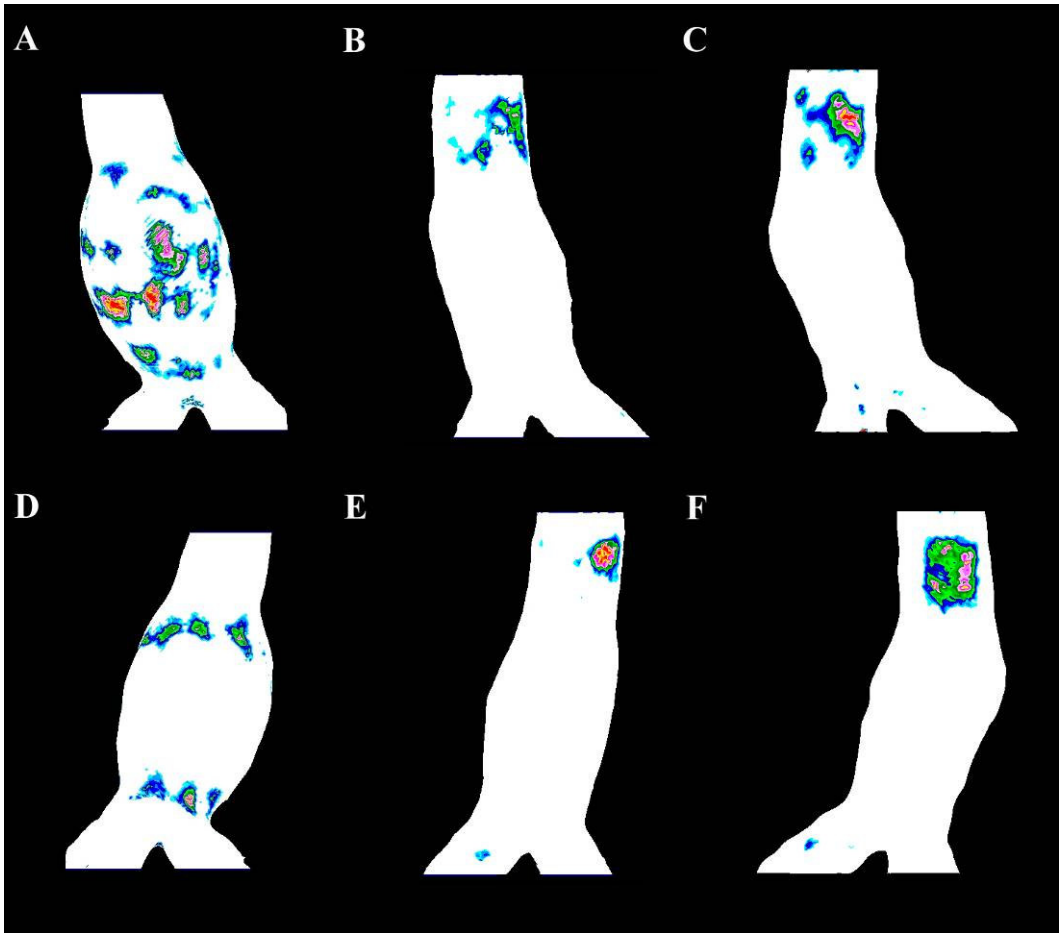

Figure 34. Peak stress locations in patient A (stable) models, A) pre-treatment with maximum von Mises stress located on anterior wall, B) early follow-up with peak stresses on and in aneurysm neck, C) anterior lateral aneurysm neck. D), E), and F) are the matching posterior views.

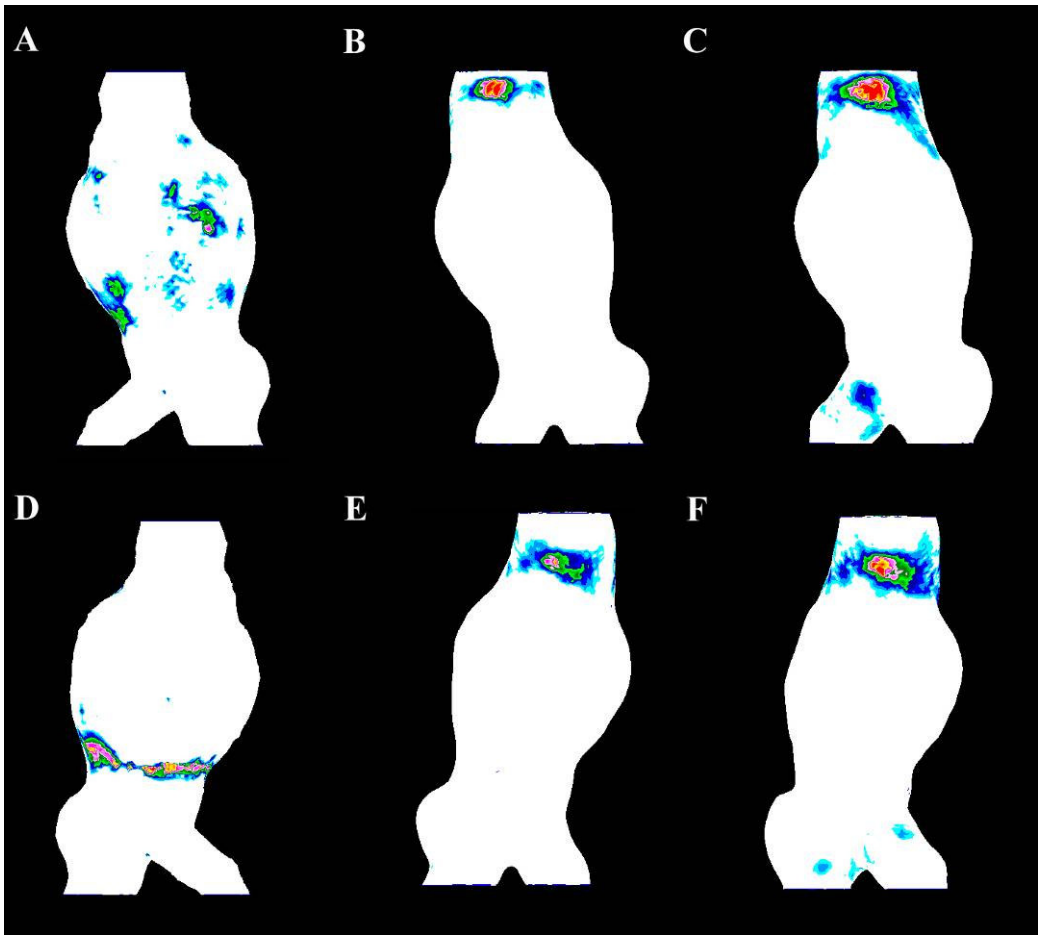

Figure 35. Peak stress locations in patient B (shrinking) models, A) pre-treatment with peak von Mises stresses located posterior along base of bulge, B) early follow-up with peak stresses on anterior aneurysm neck, C) late follow-up with peak stresses in similar location on aneurysm. D), E), and F) are the matching the posterior views.

The peak von Mises stress changes in response to treatment; the treated models indicate a markedly lower peak value (Table 11). The lowest of the peak values of von Mises stress is found in Patient A in late follow-up after treatment in the anterior neck (Figure 34). Adjusting the scales of the stress maps emphasized the location of these peak stress values. The maps indicated that although the magnitude of the peak value is

concentrated to a location, the location of highest stress is surrounded by other stress values that are also high (> 100 kPa) compared to the rest of the model.

Table 11. Maximum stress location in models of pre-treatment, early follow-up, and late follow-up with combination grafts (1 and 10 MPa) all at systolic pressure excluding "edge effect" regions.

Time Point	Peak von Mises Stress Value (kPa) and Location	
	Patient A (stable)	Patient B (shrink)
Pre-treatment	442 Anterior, middle of sac	349 Posterior distal edge of sac, above bifurcation
Early Follow-Up	375 Anterior neck	159 Anterior neck
Late Follow-Up	133 Anterior neck	233 Anterior neck

The distribution of stress relative to axial position shows how the reduction of stress is emphasized in the sac region of the aneurysm (Figure 36). "Centerline normal" indicates that the parameter was calculated normal to the centerline, not in the plane of the scan. The neck region (within the first 20 mm) has circumferentially averaged stresses of around 50 kPa in all treated models and in pre-treatment model of patient B (shrink). In the pre-treatment model of patient A (stable), the stress is closer to 80 kPa in the neck. In the sac region (from 40 to 100 mm), the effect of treatment is most clear. Average stress, around the circumference normal to the centerline, differs by more than 120 kPa in patient A (stable) and by nearly 100 kPa in patient B (shrinking). It can also be seen in the figure that patient B had a spike in stress near the distal edge of the sac,

whereas patient A had elevated stress and smaller peaks throughout the sac. Variation within a patient, between the lines representing stress, in the follow-up cases is limited to within 20 kPa with the largest of these differences occurring near the edges of the aneurysm sac.

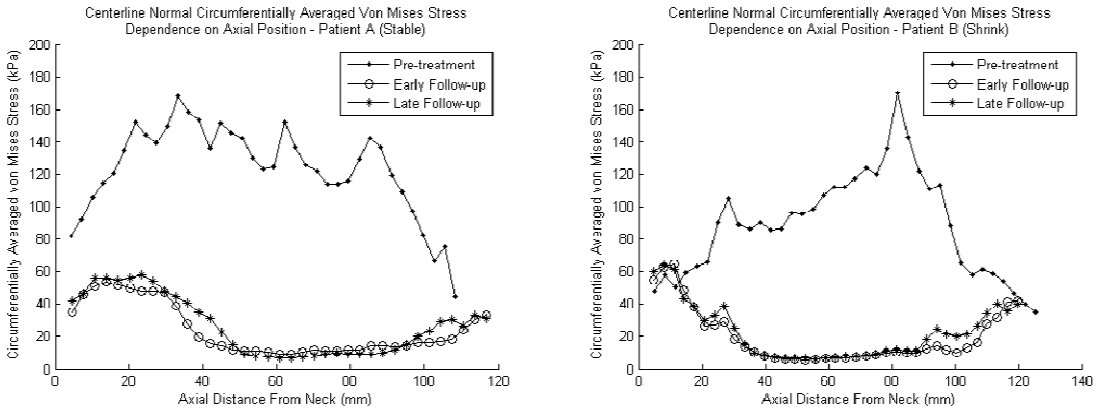

Figure 36. Centerline normal circumferentially averaged von Mises stress dependence on axial position with patient A (stable) on left and patient B (shrink) on right.

Due to the irregular shape of the lumen and subsequent difficulty in identifying a unique vessel diameter, the measurement of hydraulic diameter was used to quantify the changing size of the aneurysm. Hydraulic diameter reduces to simple diameter for a circle. The figure below shows centerline normal hydraulic diameter relative to axial position and the differences at follow-up compared to initial size (Figure 37). More details in Chapter V. Though patient A's AAA was classified as stable, there is reduction in hydraulic diameter (as was noted in the maximum diameter reports). The peak hydraulic diameter is calculated to be 47.5 mm before treatment in patient A and

43.0 and 42.8 mm in the follow-up models. There is also apparent reduction in the hydraulic diameter of patient B's AAA in response to treatment (as was noted in the maximum diameter reports), apparently larger in absolute terms but similar in relative size due to the larger size of patient B's AAA. The maximum hydraulic diameter is in patient B (shrink) was calculated to be 62.4 mm before and to be 58.7 and 58.3 mm after EVAR. The primary change occurs between pre-treatment and early follow-up (multiple millimeters), with early and late follow-up appearing similar (within 1 mm for much of the sac), although there continued to be changes >1 mm, particularly in patient A.

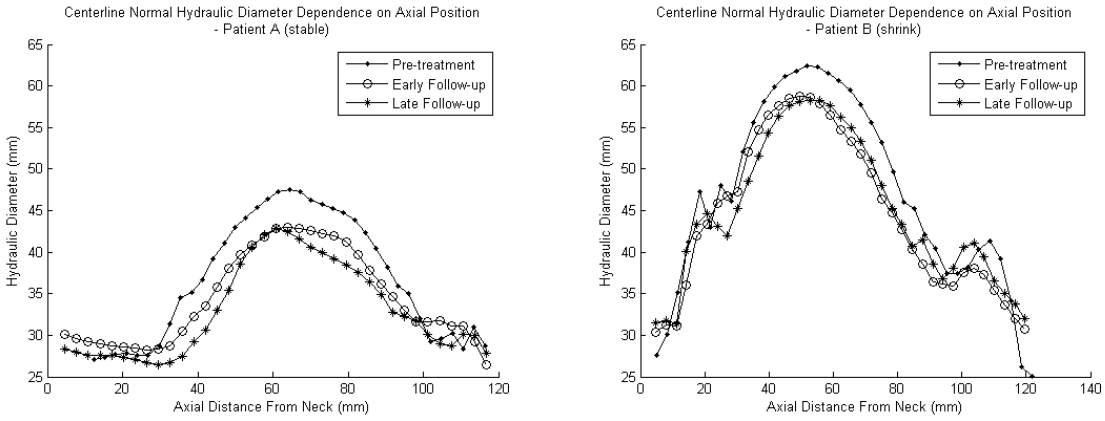

Figure 37. Centerline normal hydraulic diameter dependence on axial position for patient A on the left and patient B on the right.

In a comparison of hydraulic diameter calculated normal to the CT axis, similar results are seen (peaks vary by < 1mm from centerline normal calculation method), although the variation along the axial distance from neck is relatively reduced in the

non-normal calculation (Figure 38). The non-normal calculation is representative of a calculation that could be done without reformatting the CT scan.

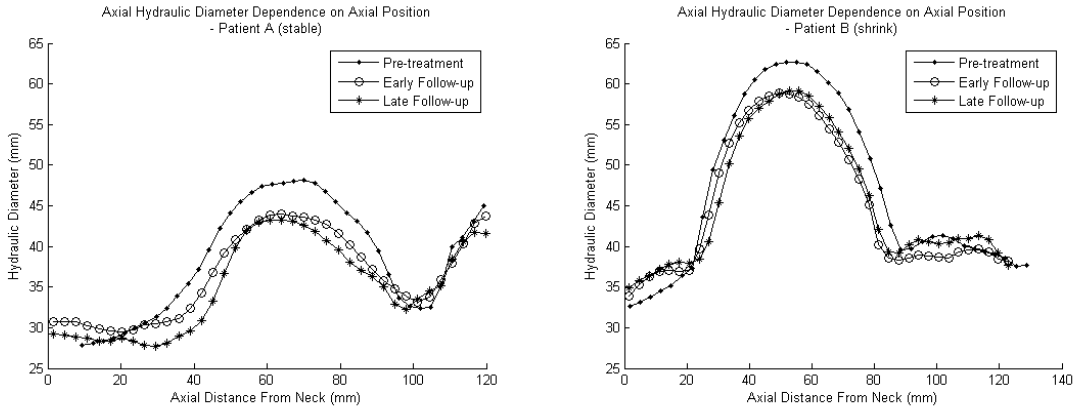

Figure 38. Axial hydraulic diameter dependence on axial position, patient A on left, patient B on right.

In addition to the comparison of hydraulic diameter, more clinically relatable parameters were used – sac area and maximum radius. Maximum radius is similar to maximum diameter, which is commonly used as a threshold for decision to operate. It is calculated by taking the maximum out of the distance of all points from the center point in the plane normal to the centerline. The centerline normal maximum radius shows reduction in the sac region (40 to 80 mm from neck) over the time in patient A (stable) from 26.3 to 25.2 to 23.6 mm, whereas variation in the maximum radius in patient B (shrink) in the neck region is less orderly from 34.7 to 31.9 to 33.2 mm. In patient B, the maximum radius in the sac region is apparently larger in late follow-up than in early follow-up – this pattern matches the average stress reduction noted in Table 10. The

distal region indicates the spread of the iliac arteries as the maximum radius is measured from a non-splitting centerline. The straightening of an iliac artery in patient B (shrink) is a possible reason why the maximum radius points do not match as well in the distal region (100 to 120 mm from neck) - Figure 39.

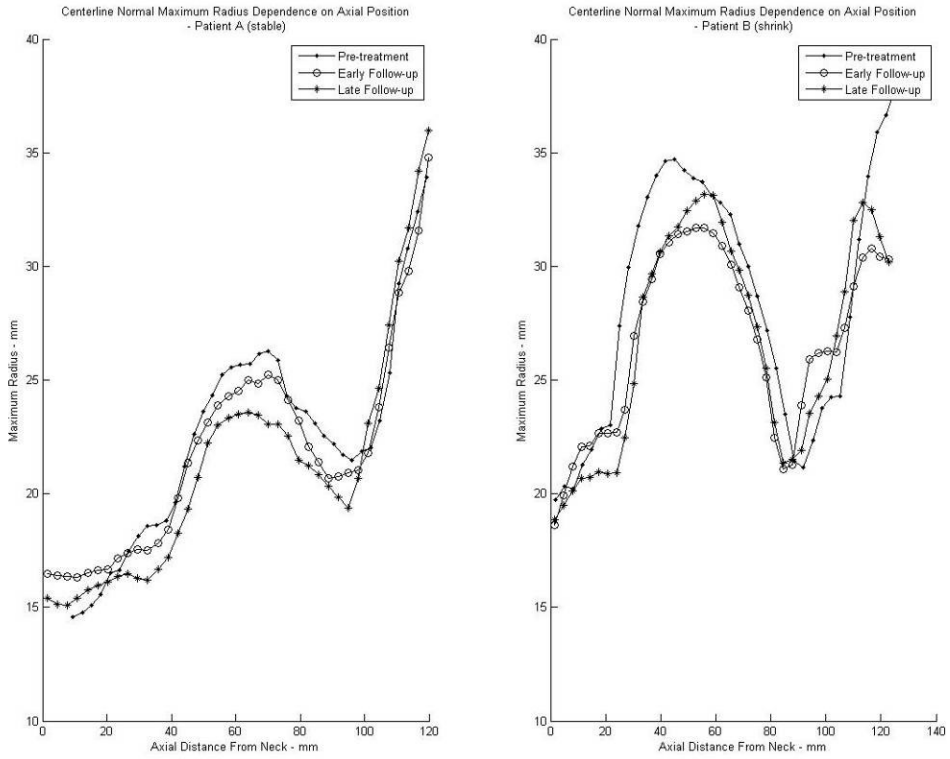

Figure 39. Centerline normal maximum radius dependence on axial position, with patient A (stable) on left and patient B (shrink) on right.

The surface area of the aneurysm at each slice changes with the shape of the aneurysm, reflecting morphology changes. It provides insight on the size of the cross-section of the aneurysm, wall exterior to wall exterior, as a function of axial position (Figure 40). The surface area of the aneurysm slice taken normal to the centerline at a series of axial positions is different from the exterior surface area of the aneurysm which has been used elsewhere to quantify aneurysm size. This slice area plot shows the primary change in magnitude occurred between pre-treatment and early follow-up. The change is of similar magnitude between patient A and patient B, a change of nearly 400 mm^2 at its peak. The peak slice areas of patient A (in sac region on up through neck) are 1838, 1558, and 1491 mm^2. For patient B (shrink), the peak slice areas are 3114, 2801, and 2754 mm^2. However, patient A (stable) appears to show a more of a narrowing of the curve as the length of the expanded region seems to reduce over the time series more than that of patient B (shrink).

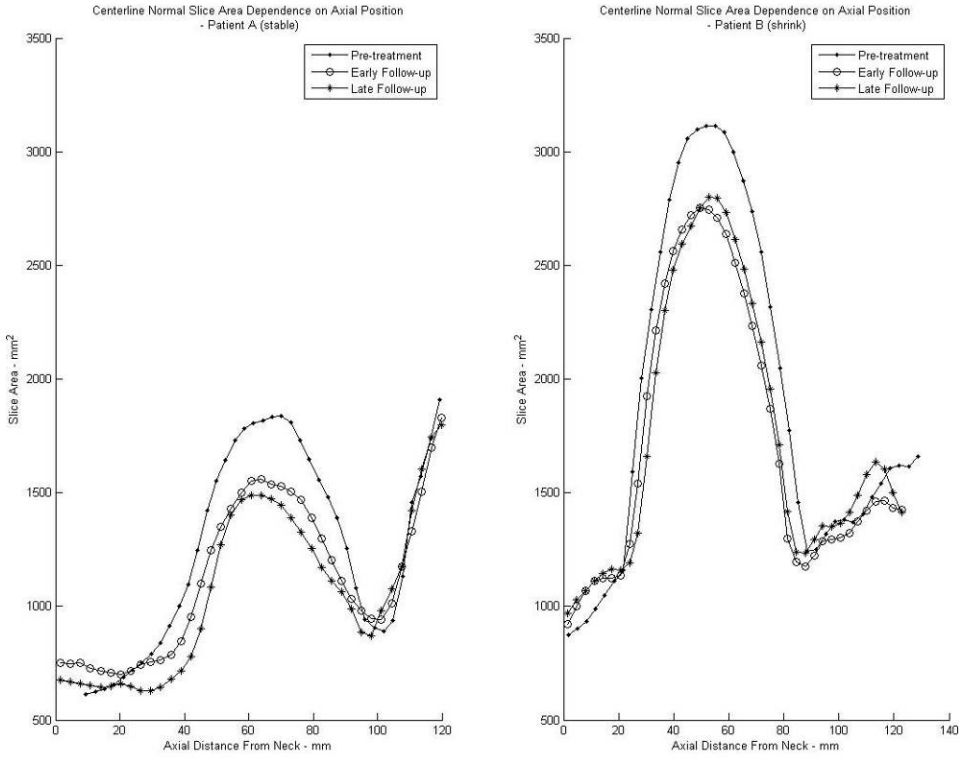

Figure 40. Slice area, calculated normal to centerline, dependence on axial position with patient A (stable) on left and patient B (shrink) on right.

The inclusion of the endograft induces regions of lower von Mises stress in the aortic walls to concentrations hardly seen in the pre-treatment models, with the lower stress nodes more prevalent in the patient B (shrink) model than in patient A (stable). These differences may or may not be significant – untestable with such a small sample. In this study, it appears that the shrinking aneurysm has a greater proportion of nodes with very low stress at early and late follow-up. These very low stresses (<10 kPa) are barely present in the nodes of pre-treatment models (< 0.1 % in each). The portion of nodal values in the 10-20 kPa range is 18.3% in patient B (shrink) early follow-up and 19.9% in late follow-up; with patient A (stable) the values are 25.2 to 15.3% over the comparable period. However, the <10kPa percentage went from 20.5 to 28.6% in patient A, and it went from 46.5 to 38.9% in patient B, early to late follow-up. The net changes over the 0-20kPa range between early and late follow-up were 45.7 to 43.9% in patient A (stable) and 64.8 to 58.8 in patient B (shrink). The location of these lower stresses can be seen in Figure 42, which shows the regions on the surface of less than 16 and 8 kPa. These stresses are found primarily in the excluded sac region of both patients, with patient B showing greater coverage of the sac with 8-16 kPa range.

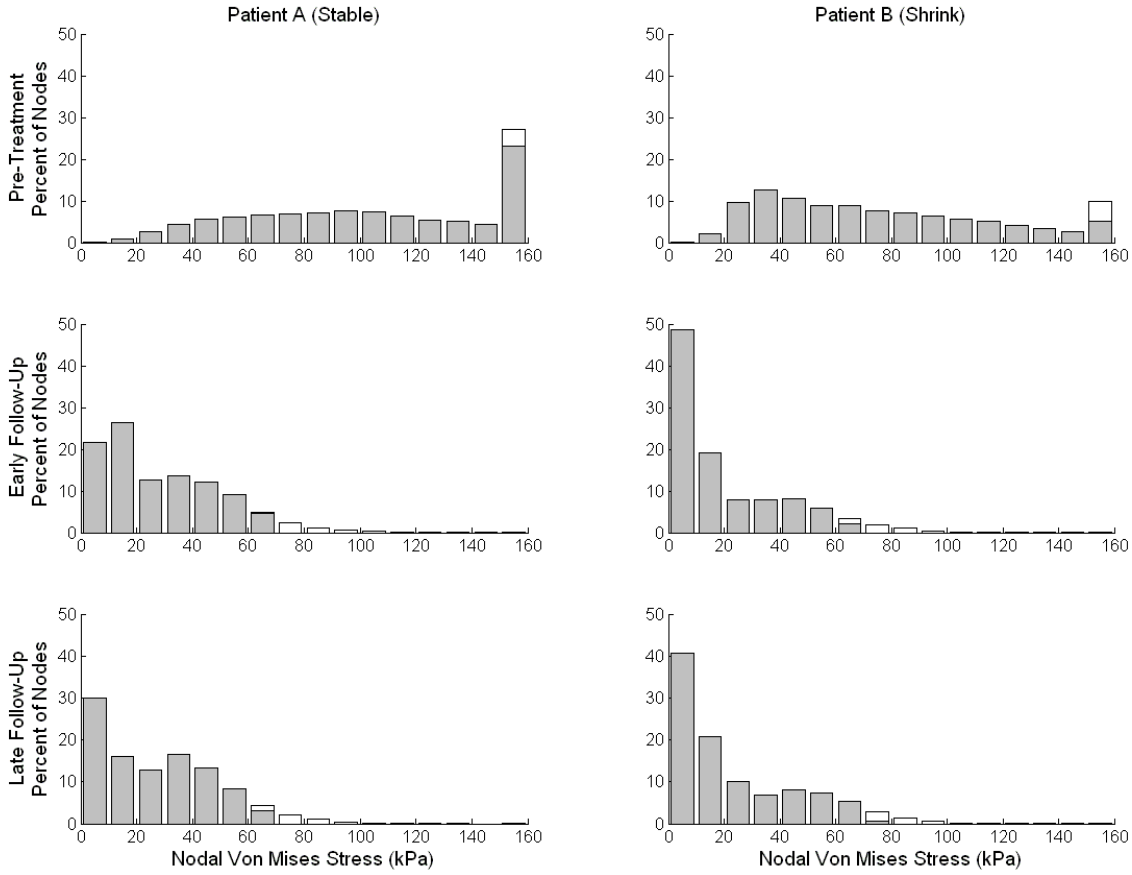

Figure 41. Histograms for each of the models run with combination grafts - gray node sets excluding top 5% of values, white rectangles for histogram with the same bins excluding no values.

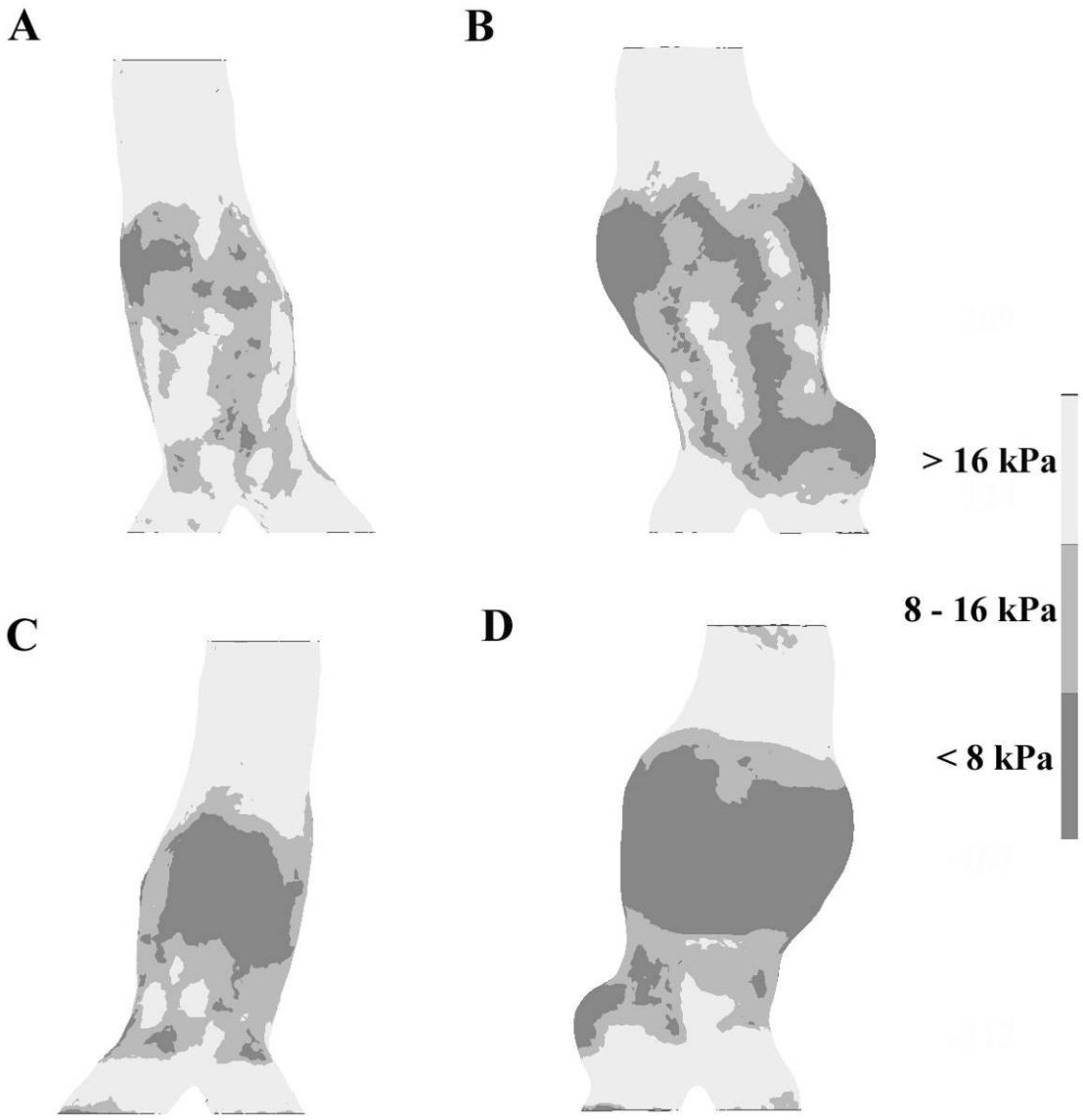

Figure 42. Von Mises stress maps of early follow-up models with adjusted scale to emphasize areas of low stress. A) patient A (stable) anterior, B) patient B (shrink) anterior, C) patient A posterior, D) patient B posterior.

The histograms in Figure 41 highlight the fact that the peak values generated in the treated models are uncommon, most nodal stress values (> 95%) are less than 80 kPa. The peak stresses (Table 12) show that eliminating the highest stress value nodes in an automated fashion (in case they represent spurious calculations), maintains trends between and within model classes.

Table 12. Peaks of von Mises stress (kPa) calculated with portion of nodes to exclude outliers.

		Peak of von Mises stress (kPa)			
		Percentage considered (higher nodes eliminated)			
Model	Time point	90.0%	95.0%	99.0%	99.5%
Patient A (stable)	Pre-treatment	197	219	273	293
	Early Follow-Up	59	69	92	104
	Late Follow-Up	57	66	84	89
Patient B (shrink)	Pre-treatment	150	174	207	220
	Early Follow-Up	54	65	86	95
	Late Follow-Up	61	72	95	109

A similar table below shows average von Mises stress values calculated with a variety of percentages of nodes eliminated. The differences between groups remain consistent.

Table 13. Average of von Mises stress with only a portion of nodes considered to see the effect of potential outliers.

		Average of von Mises stress (kPa)			
		Percentage considered (higher nodes eliminated)			
Model	Time point	90.0%	95%	99.0%	99.5%
Patient A (stable)	Pre-treatment	102.7	108.1	113.4	114.3
	Early Follow-Up	24.5	26.6	28.6	29.0
	Late Follow-Up	23.7	25.7	27.6	27.9
Patient B (shrink)	Pre-treatment	69.1	74.0	78.5	79.2
	Early Follow-Up	16.3	18.6	20.8	21.2
	Late Follow-Up	19.5	22.0	24.3	24.7

8.3.2 Endograft Properties

The stress reduction in treated aneurysms is dependent on the mechanical properties of the endograft with greater stiffness resulting in lower stress. Looking at a range of endograft properties in addition to the combination properties shows this apparent effect. In patient A (stable), a range of endograft properties results in corresponding changes in average stress values (see Table 14) within models of treated aneurysms pressurized to 120 mmHg (16 kPa).

Table 14. Role of graft properties on average von Mises stresses in patient A (stable) models.

Time Point	Graft Stiffness Parameters	Average von Mises Stress (kPa)
Early Follow-Up	10.0 MPa	21.9
Early Follow-Up	1.0 MPa	51.2
Early Follow-Up	0.1 MPa	77.3
Early Follow-Up	- (no graft)	87.8
Early Follow-Up	Combo (1/10 MPa)	29.4
Late Follow-Up	10.0 MPa	17.7
Late Follow-Up	1.0 MPa	33.0
Late Follow-Up	Combo (1/10 MPa)	28.2

Within early follow-up models, as the stiffness assigned to the graft increases, from no graft to 10.0 MPa, the stress decreases from 87.8 kPa to 21.9 kPa, a change of 75% (65.9 kPa). This decrease is greatest in the property change from 1.0 to 10.0 MPa, which is 29.3 kPa or 57% of the 1.0 MPa average von Mises stress. The disparity between no graft and a graft with a uniform modulus of 0.1 MPa is 10.5 kPa. Also, the discrepancy between average stresses in the late follow-up models of 1.0 to 10.0 MPa is 15.3 kPa (46%). This discrepancy is less than that seen in the early follow-up models, but of consistent direction. The combination properties in the grafts result in an average stress value between that of the 10.0 MPa and the 1.0 MPa endograft treated models. In the early follow-up models, the combination graft appears to be closer to the 10.0 MPa in stress than the 1.0 MPa. Whereas, in the late follow-up models, the combination graft results are apparently much closer to the 1.0 MPa results than the 10.0 MPa.

In a similar analysis of patient B (stable) models, the results follow the same trends over the smaller range of models run (see Table 15) in that the average stress

calculated with a combination graft is more than 1.0 MPa and less than 10.0 MPa models. The early follow-up models indicate the disparity in average von Mises stress between 1.0 MPa and 10.0 MPa endografts is 18.2 kPa, the combination properties lie near the middle, but apparently closer to the 10.0 MPa endograft treated model. The late follow-up model run indicates that the combination properties may result in lower average stress than the 1.0 MPa graft stiffness.

Table 15. Role of graft properties on average von Mises stresses in patient B (shrink) model.

Time Point	Graft Stiffness Parameters	Average von Mises Stress (kPa)
Early Follow-Up	10.0 MPa	13.1
Early Follow-Up	1.0 MPa	31.3
Early Follow-Up	Combo (1/10 MPa)	21.6
Late Follow-Up	1.0 MPa	38.0
Late Follow-Up	Combo (1/10 MPa)	25.3

The stiffer graft appears to reduce stress more in these models, but the amount by which it does so does not seem to scale perfectly with endograft properties independent of model geometry/patient.

8.3.3 Role of Thrombus

Thrombus is present in most aneurysms before treatment with endograft, but it also forms within the gap between the original lumen and endograft subsequent to endovascular repair. In the models analyzed here at systolic pressure, the inclusion of thrombus made a notable difference in stresses. For instance, from comparison of the values in the table, the role of thrombus might be seen as crucial (46.5% reduction) in

stress calculations for patient B pre-treatment, the patient whose aneurysm showed shrinking in follow-up CT scans (Table 16). The impact thrombus inclusion makes in modeling the stress of patient A (stable) is a 40.2% reduction.

Table 16. Average von Mises stress with and without thrombus in untreated patient-specific models.

	Average von Mises stress (kPa)	
	Patient A (stable)	Patient B (shrink)
With thrombus	115.3	80.0
No thrombus	192.7	149.6

A potential reason for this can be seen in the following figures (Figure 44 and Figure 43), which show the thrombus shape apparent difference between the two models. The figures show the nodes at the surfaces of the wall and thrombus in addition to the calculated stress patterns with and without thrombus in the models. In Figure 44, the thrombus of patient B (shrink) is thickest in the proximal half of the aneurysm sac as can be seen from the lateral view. Thrombus is present laterally as well in the proximal half of the aneurysm sac and also is present near the bifurcation in the secondary bulge. In these areas of greatest thrombus thickness, the apparent stress reduction as a result of thrombus presence is most notable. In the anterior view of the model areas of high stress (shown in pink to red) appear to increase in area covered in the absence of thrombus. In the posterior view, the impact of thrombus is more dramatic as the colors shift from green and light pink to red (increased by > 100 kPa), with nearly the entire posterior surface turning red (> 310 kPa). In Figure 43, which shows patient A (stable), the

changes are again clear. The effect of thrombus is noteworthy on the posterior surface where an area of stresses (blue) on the thrombus model is green to red (increased by > 100 kPa) on the model without thrombus. This area corresponds to the area of greatest thickness of thrombus in this model. Figure 43 also shows a slight decrease in stress with thrombus presence on the anterior surface. This surface contains lesser thrombus so that the increased net stiffness of the posterior wall may be increasing the percentage of load carried by the anterior wall.

8.3.4 Pressurization Method

Whether pressure is applied to the lumen (comprised of thrombus and wall surfaces) or wall (entire interior surface, including regions covered by thrombus) in these models seemingly makes little difference. The impact on average von Mises stresses is 1.2% for patient A (1.4 kPa) and 1.1% for patient B (0.9 kPa) (Table 17). The figures showing stress on the exterior walls using both methods are nearly indistinguishable (Figure 45 and Figure 46).

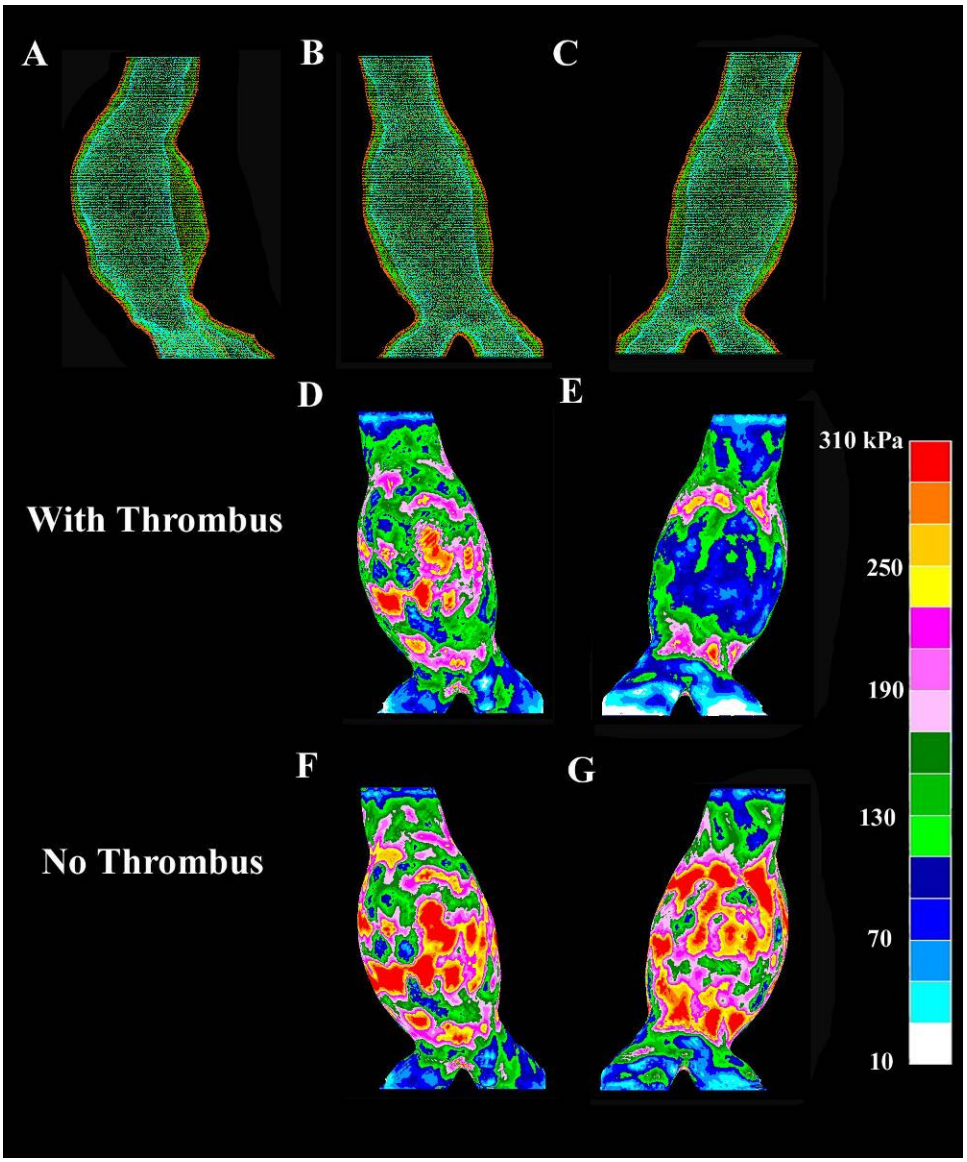

Figure 43. Effect of thrombus on von Mises stress in patient A (stable) model. A) is lateral view of nodes of inner thrombus and wall surfaces, B) anterior view of surface nodes, C) posterior view of surface nodes. D) Anterior with thrombus, E) posterior with thrombus, F) anterior without thrombus, and G) posterior without thrombus.

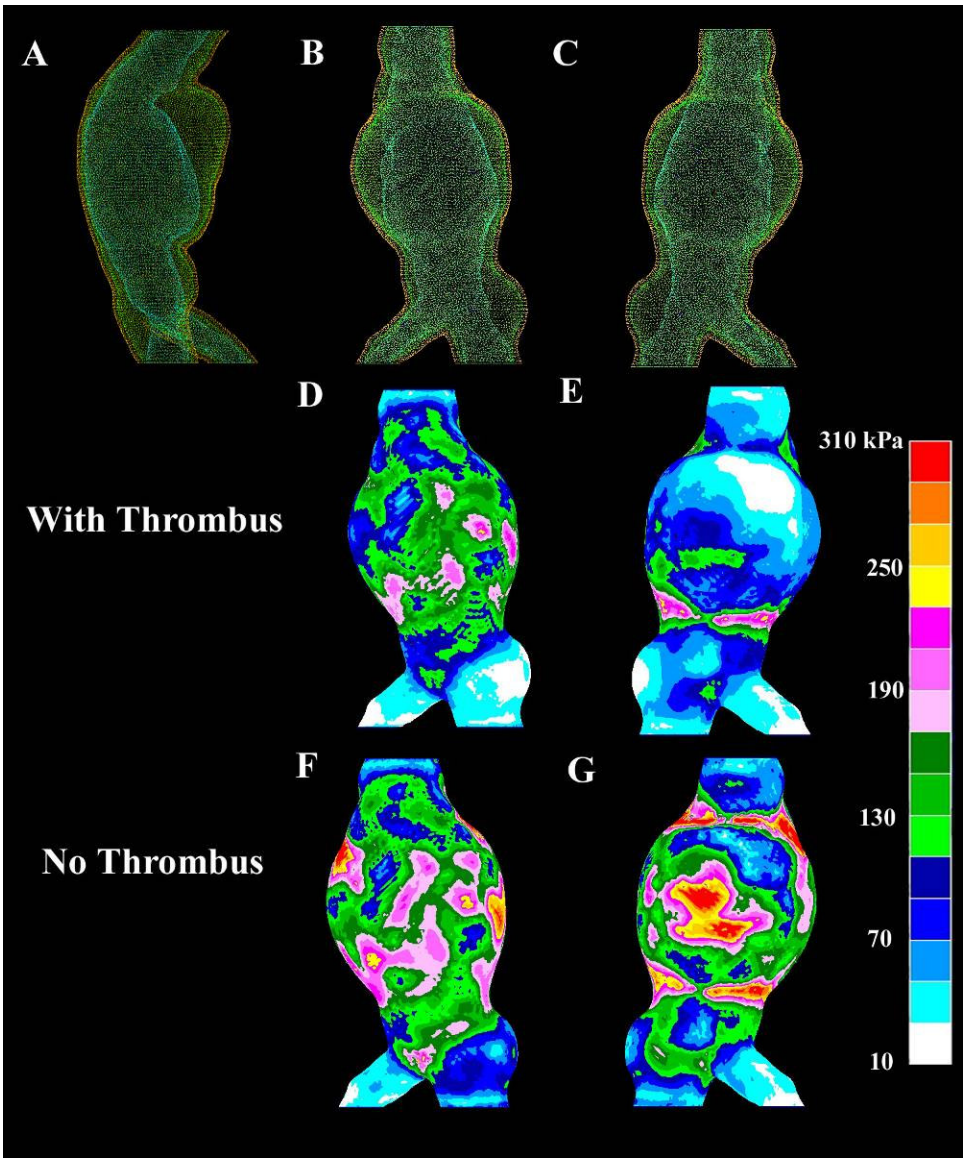

Figure 44. Effect of thrombus on von Mises stress in patient B (shrink) model. A) is lateral view of nodes of inner thrombus and wall surfaces, B) anterior view of surface nodes, C) posterior view of surface nodes. D) Anterior stress map with thrombus, E) posterior with thrombus, F) anterior without thrombus, and G) posterior without thrombus.

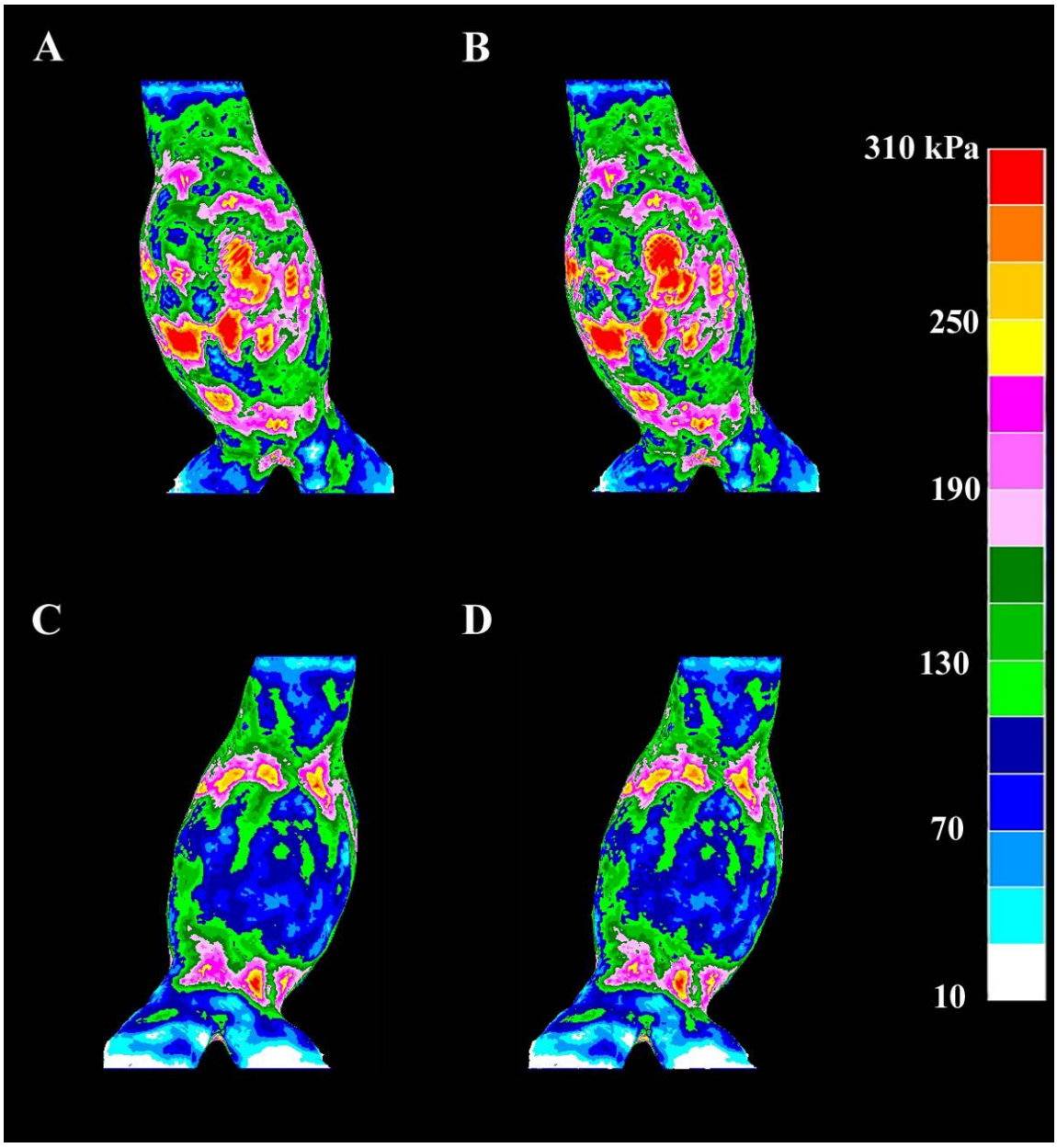

Figure 45. Von Mises stress maps for patient A (stable) - pre-treatment model with wall pressurization on left and lumen pressurization on right side. A) Anterior view, pressurized wall B) anterior view, pressurized lumen, C) posterior view, pressurized wall, and D) posterior view, pressurized lumen.

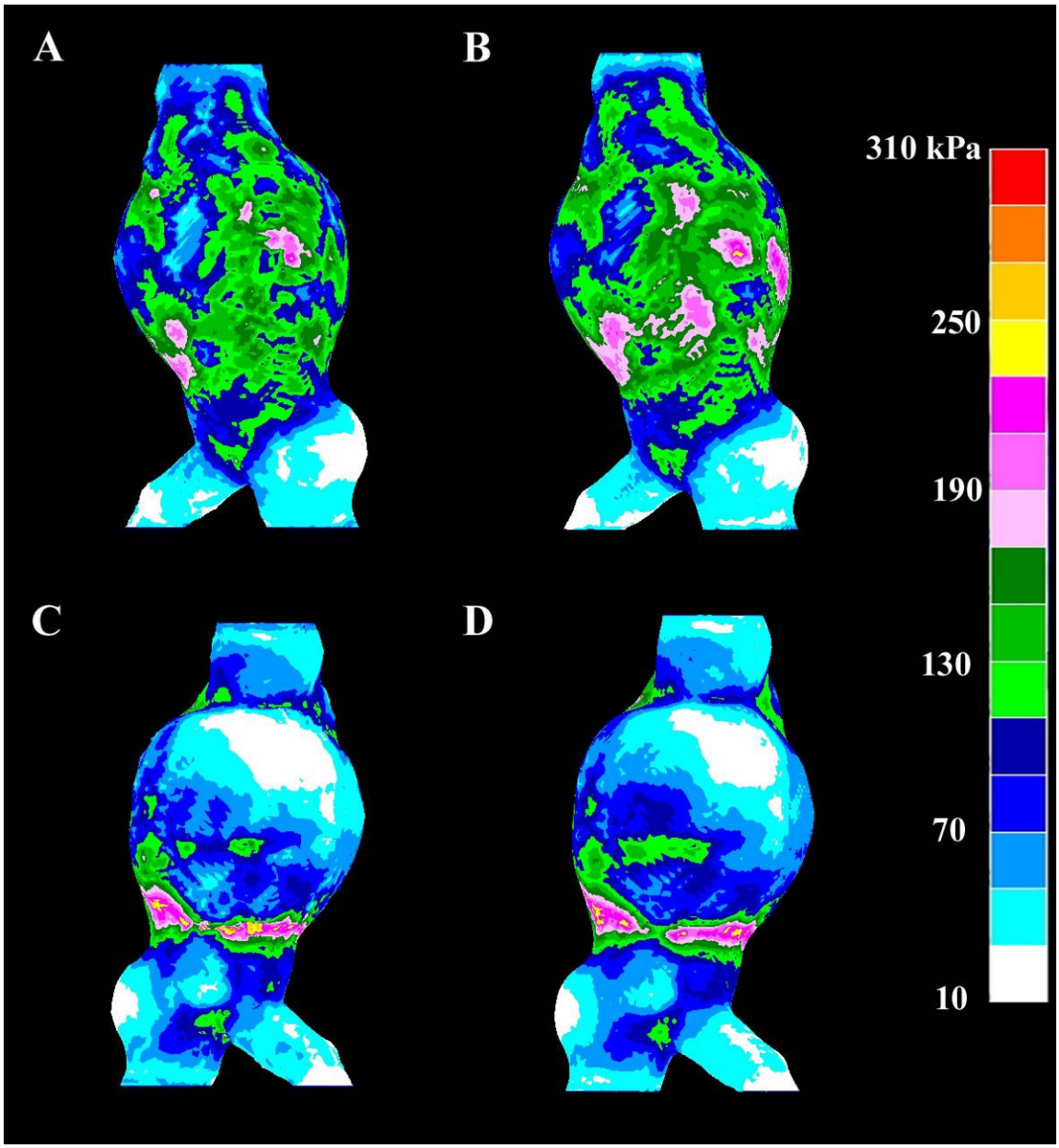

Figure 46. Von Mises stress maps for patient B (shrink) pre-treatment model showing pressurization of wall (left) and lumen (right). A) Anterior view with pressurized wall, B) anterior view, pressurized lumen, C) posterior view, pressurized wall, and D) posterior view, pressurized lumen.

Table 17. Pressurization surface influence on average von Mises stress in untreated models.

Pressurization Surface	Average of Von Mises Stress – kPa	
	Patient A ("stable")	Patient B ("shrinking")
Lumen	116.7	80.9
Wall	115.3	80.0

The amount of pressure applied to the interior of the model affects the final average stress value with diastolic pressurization (80 mmHg) resulting in less than 2/3's of the value in the same models pressurized systolic value (120 mmHg) (see Table 18). The difference in average stress is ~62%, except in the case of patient A early follow-up (stable) where the difference is 50%. The trend of seemingly much lower stress in treated than pre-treated continued in these diastolic models with differences of 79.8% for patient A (stable) and 72.3% for patient B (shrink).

Table 18. Average of von Mises stress values of patient-specific models in response to systolic and diastolic pressurization.

Patient	Time Point	Average von Mises Stress (kPa)	
		Systolic (16 kPa)	Diastolic (10.667 kPa)
A ("stable")	Pre	116.7	72.8
A	Early Follow-Up	29.4	14.7
B ("shrinking")	Pre	80.9	50.1
B	Early Follow-Up	21.6	13.9

8.3.5 Notes on Method of Presentation

The stresses shown for the outer wall are comparable to the inner wall in relative value (relatively high and low stress areas remain relatively high and low); though the absolute magnitudes are reduced on the interior (Figure 47 has an illustrative example from patient B). The stress values along the anterior exterior side are > 100 kPa as are stresses near the lower edge of the sac. These places on the anterior are shown to be relatively high, but reduced, (> 78 kPa) in mostly the same places both from interior view and exterior view. There is some variation in patterns of stress values as the reduction of scale to 60% of other scale shows more regions of red lie on the anterior wall than on the exterior view. There is also apparently greater relative stress at the top of the sac where the sac meets the neck in the interior view. However, both views appear to show lower stress in the area of the wall at the proximal posterior portion of the sac away from the neck and in the iliac artery.

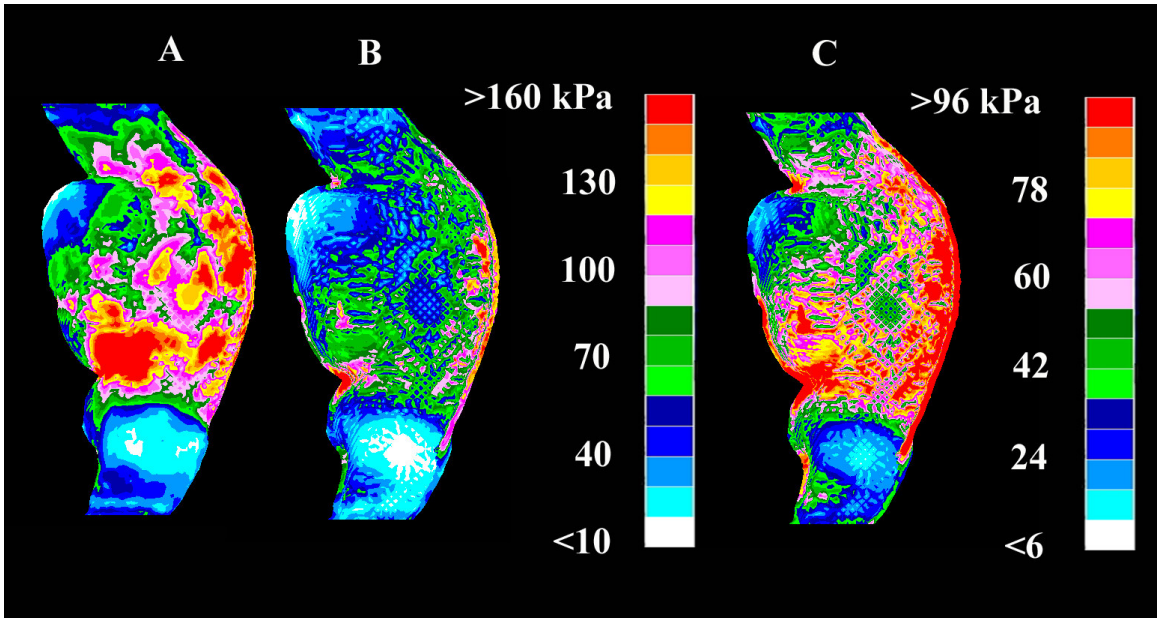

Figure 47. Maps of von Mises stress on the AAA pre-treatment model of patient B. (A) Side view from the exterior with standard scale – mirrored to match interior views, (B) is of the elements of the wall viewed from the interior with standard scale, and (C) is of the interior with scale reduced by 60%.

9. PATIENT-SPECIFIC MODELING DISCUSSION AND CONCLUSIONS

9.1 Patient-specific Discussion

The purpose of the patient-specific models was to quantify the nature of stress changes in the region of two different AAA following endograft implantation. In the two patient-specific geometries studied, stress in the sac region of treated geometry models was reduced under a range of endograft properties (0.1 to 10 MPa) and throughout the range of physiologic pressures (80 to 120 mmHg). In the most realistic set of models (using combination endograft properties), the reduction of average stress was accompanied by a shift in peak stress location from the sac to the neck as well as reduction in peak stress value (Table 11 and Table 12). There is evidence of high stress being associated with rupture (even better than the clinical diameter measure) [7].

The reduction and shift of high stress implies that after technically successful deployment of the endograft, the greatest rupture risk and growth/remodeling risk is in the attachment regions instead of the sac. However, this implication is constrained by factors not included in this model, such as changes in the wall's material strength, stiffness, or thickness in response to endograft treatment – all which may change unfavorably in response to reduced loading and blood flow.

Patient A (stable), had a higher pre-treatment average stress than Patient B (shrink), despite a smaller maximum diameter. The maximum diameter in Patient A was 44.5 mm by radiology report (47.5 mm hydraulic diameter in reconstruction) with an average stress of 116.7 kPa. The maximum diameter of Patient B was 62.3 mm by radiology report (62.4 mm hydraulic diameter in reconstruction) with an average stress

of 80.9 kPa. The patient A pre-treatment model had higher stress as indicated by peak values of von Mises stress. This finding is consistent with the reports of aneurysms at lower maximum diameters being capable of having higher stress, and it is a reason the maximum diameter criterion has been questioned. Since there are only one set of geometries for each "stable" and "shrink" patient, the differences between the two cannot be confirmed as statistically significant. There are marked differences between the treated and pre-treatment groups as well as some apparent differences between the "stable" and "shrink" patient in stress values, suggesting further study in a larger population is warranted.

The endograft's impact on stress reduction is dependent on the material properties used in the models, within a given geometric case, with the stiffest graft reducing average stress by the most. This reduction is not surprising because the implantation of the graft is modeled such that the increased stiffness of the graft causes reduced diameter expansion at the same pressure. However, this reduction is not realistic over all regions because a stiffer endograft would cause a larger equilibrium diameter in the attachment regions because it is oversized relative to the initial pressurized geometry. The magnitude of overall reduction is in-line with the pressure reductions of 80% and 70% measured in aneurysm sacs of treated, shrinking and stable AAA, respectively [31].

A comparison of the model run of patient A with 0.1 MPa graft and with no graft to those over the range of properties (1.0 to 10.0 MPa) shows that there is a limit as to the amount of impact a graft would have if it were softer – meaning, if soft enough, it

would act the same way as an untreated aneurysm in terms of reducing displacement in response to pressure. There must be some tension taken up in the wall of the endograft to provide a difference in transmural pressure, and this requires a certain degree of mechanical rigidity. Even stiffer (> 10 MPa) endografts would likely result in a different equilibrium geometry, but reduce stress further within the aneurysm sac – although it appears that stress is already reduced to a low value (below the values of stresses in the attachment regions in the pre-treatment models).

The model of early follow-up geometry of patient A ("stable") run without a graft allows a comparison to pre-treatment model highlighting that the stress in the wall has been apparently reduced by the remodeling process (including wall and thrombus morphology changes). This reduction in the early follow-up model run without the endograft is probably reflective of the reduced external diameter (in conjunction with the modeling method that allows for no change in wall thickness) and increased thrombus, each of which should contribute to reduced stress.

Atrophy may be indicated by the changes in proportion of low stresses (< 20 kPa). The proportion of low stresses is increased dramatically by treatment but falls somewhat at subsequent follow-up. This fall may reflect shape change as the wall tries to return tension to nominal value/range (Figure 36). A cuffing procedure using a carotid artery around another carotid showed wall atrophy in response to the induced reduction of wall tension [94]. If this trend of low stress reshaping holds in a larger sample size, it would imply that graft design should consider this effect and graft properties tailored to reduce size of the sac slightly (so as to alleviate symptoms, if

present) or to be capable of tolerating the drastic changes in sac shape that can lead to device separation, kinking, and failure.

The important role of thrombus inclusion in modeling shown here was shown in the Vande Geest thesis [95], which showed a 1% to 61% reduction in peak maximum principal stress in their patient-specific models of untreated AAA. A 4% to 85% reduction in average maximum principal stress as a result of thrombus inclusion in their models when using the same isotropic properties for the aneurysm and thrombus as used here, though they used shell elements for the aneurysm wall which another group associated with potential inaccuracies in stress distributions [82].

The various measures of aneurysm size quantification used in this study included hydraulic diameter which is quickly relatable to initial nominal size, maximum radius which is half of the maximum diameter criterion, and slice area which provides an idea of area change. Hydraulic diameters can be compared to nominal graft component diameters to detect graft compression/tension – which are indicative of sac pressure relative to lumen and might eventually be useful for detecting pernicious endoleaks. However, due to the noise present in the measurement with current method, it is not immediately useful for endoleak detection (Figure 16). Hydraulic diameter and slice area indicate that the largest change occurs between pre-treatment and early follow-up in both models. The maximum radius value is more subject to noise, since there is no integral area calculation involved. The usage of image plane/axial normal references complicates comparison using any of these measures as both references have their limitations that prevent direct comparison with each other across time points and

patients. Image plane measurements are easier to implement because there is no need for creating a reformatted image from the stack.

The lack of difference seen with pressurization method can provide guidance for future modeling, in that the limitation seen in applying pressure to the lumen or the entire inner wall surface (with thrombus still present) makes little difference. It also implies that if the thrombus is found to be of capable of transmitting pressure directly it will not necessarily imply a mechanically insignificant role for the thrombus in reducing stress. The thrombus, if firmly attached, can provide a supporting framework preventing what would be otherwise greater dilation of the AAA.

The difference between averages of von Mises and maximum principal stresses were small (<10%). Other measures of comparison between stresses were not evaluated. The similarity between von Mises and maximum principal stresses result was also noted in the appendix of Fillinger et al. 2003 in their analysis of untreated patient-specific models [7], though the models here show that this can be extended to models incorporating endografts.

9.2 Patient-specific Conclusions

The models built from CT scans covering treatment history of two patients with stable and shrinking aneurysms treated with endografts show that stress average was reduced in the aneurysm wall by the endograft by nearly 75%. The changes in stress were strongly dependent on position. The greatest stress reduction occurred in the sac, while an increase in stress was noted in the aneurysm neck. The stress reduction is dependent on graft properties, with the reduction greater with higher stiffness grafts and

the combination graft creating a reduction of the average stress between that of the higher and lower stiffness grafts. Also noteworthy, but very limited by the sample size, the "shrinking" aneurysm had a lower average stress value after early treatment than the "stable" aneurysm, though the amount of reduction was similar and the definition of stable/shrinking imprecise. Also interesting was the reduction in percentage of nodes with stresses < 20 kPa between early and late follow-up, potentially implying that aneurysm shrinkage is continuing and controlled by low stress regions.

10. SUMMARY

The work here addresses the specific aims of developing and analyzing axisymmetric models of AAA, developing patient-specific solid mechanical models of AAA, analyzing a series of patient-specific models of AAA treated with endografts over a period of 2 years, and determining the effects of key modeling assumptions on outcomes. The axisymmetric models show that the presence of the endograft causes reduced displacements in the aneurysm sac in response to pressure and an increase in neck diameter that are related to graft stiffness. The solid mechanical models of AAA were built from patient CT scans obtained from Scott & White and reflect a patient with a clinically stable aneurysm and a patient with a clinically shrinking aneurysm. These aneurysms were modeled at their pre-treatment, early follow-up, and late follow-up time points. It appears that larger areas of lower stress in the aneurysm are associated with more reduction in sac size, and endografts do reduce the stress in the aneurysm wall. The work is unique in its following of endograft treated patients over years with nonlinear solid mechanical FEM models suggests including thrombus is important to modeling the pre-treatment case of AAA.

11. LIMITATIONS, FUTURE DIRECTIONS, AND CONCLUSIONS

11.1 Assumptions and Limitations

This study has several key limitations related to geometry, materials, and loading conditions. These limitations restrict accuracy and limit the strength of the conclusions, but are not likely to change the fundamental conclusion that the endograft reduces stress in the aneurysm sac when successful. Also, the reporting of von Mises stress does not imply that von Mises stress is necessarily the best or most useful measure of stress for association with rupture or adaptation.

The geometric assumptions include a uniform thickness for the aneurysm wall, appropriate smoothness of all structures, loading an already pressurized shape, and identifying tension/compression. The assumption of a uniform thickness for the aneurysm wall is based on a lack of clear information on wall thickness from the CT scans. Other studies have utilized a range of thicknesses in their analyses to indicate that non-uniformity affects stress distribution, but a uniform change in thickness primarily changes amplitude uniformly (without affecting distribution). An appropriate smoothness of structures is important because reconstructions too smooth will prevent stress from concentrating as it should and reconstructions too rough will have unrealistic stress concentrations. Unrealistic stress concentrations are a concern in this study when looking at peak stress values, as they may be reflective in some cases of poor mesh construction. The underlying trends do appear valid, as the peaks and averages maintain their relative differences even when excluding different percentages of the highest nodal values. Using an initially pressurized geometry as the starting point changes final values

of stress (reducing stress in the neck by over 60% in axisymmetric models) and artificially improves smoothness, but these impacts should be consistent across the models used. The segmentation of the graft into tension and compression regions was based on results which were not absolutely clear-cut. Changing the assignment of properties could change the distribution of stresses, although the magnitude of change would be restricted to the range of those results shown by the 1.0 and 10.0 MPa models run with uniform properties, which also showed stress reduction resulting from endograft presence. The geometric assumptions give uncertainty to the numeric values but do not challenge the broad conclusions.

The material properties utilized in the models are uniform and isotropic despite non-uniformity and anisotropy in some material testing. The uniformity of the wall, with its lack of calcifications, means that there are no structures within it that can create concentrations or extra rigidity. The anisotropic models are based on anterior wall samples from repaired AAA, and while differences have been seen in magnitude of stress in models, the amount of difference associated with directions is not large. These limitations reduce the confidence in stress distributions and values.

The loading conditions in the models reflect average and uniform constraints. The usage of 80 and 120 mmHg as pressures instead of patient specific values allows for direct comparison. Using a patient specific value is convoluted by the variations found in patient BP over the course of their treatment and by different measurement locations. A true measure of aortic blood pressures taken during a gated CT scan would be ideal, but invasive and not available in this retrospective study. The fixed ends allow no

further stretch, which is consistent across models but does not allow any axial motion to occur that could reduce some of the stresses generated by the pressure. The lack of contact with other structures prevents stress concentrations and load distribution changes which may occur. There is very little information available on the nature of the contact between internal structures (such as spine) so their potential contributions have been ignored. The loading conditions used are uniformly applied to the models to allow comparison and do not account for all loads present in vivo.

The sample of one stable and one shrink patient means that the study is not adequately powered to confirm important differences. This limitation is present because of the cost in time and resources necessary for development of the tools used in this study. It is uncertain whether the differences between stable and shrinking treated aneurysms that were identified are statistically significant and important. However, it is presumed that existing differences can be tested for significance after applying the methods developed herein to a larger population.

11.2 Future Directions

Future models could include modeling the deployment of the endograft, better material models, better image resolution, and incorporate growth and remodeling. Including the deployment of the endograft would allow for the pre-loading and equilibrium diameter to be estimated as well as providing better stress estimates in attachment regions. The usage of material models with anisotropy, residual stress, and graft material models based on more thorough testing could provide a more accurate picture of the values of stress over the time course of treatment. Improved image

resolution would allow for better constituent identification - perhaps allowing for greater automation of the process, identifying wall thickness at all levels, and calcification. Improved image resolution would also allow for better identification of graft tension/compression which would allow more confident assignment of properties eventually leading towards pre-loading the graft, in case deployment was not directly modeled. Incorporating growth and remodeling would allow prediction of the aneurysm response to EVAR, perhaps allowing for greater specificity in patient eligibility and improvements to endografts design.

Abdominal aortic aneurysm research has come a long way from the autopsy study of diameter. Stress analysis is best suited for management of patients for whom surgery is high risk and greater insight into likelihood of rupture is needed. The work done here can be extended to model the effect of grafts on stresses within these patients. It should also be extended to a larger patient population.

11.3 Conclusions

The results indicate that the variation of endograft properties can play a large role in the stresses within the aneurysm wall – both peak and average. The sample sizes are much too small to draw any statistically significant conclusions, but it appears that the shrink patient had lower average stress than the stable patient after treatment. It also appears that the inclusion of thrombus is important for accurate pre-treatment models.

REFERENCES

[1] Perler, B. A., and Becker, G. J., eds., 1997, *Vascular Intervention: A Clinical Approach*, Theime Medical Publishers, Inc., New York.

[2] Thomas, P. R., and Stewart, R. D., 1988, "Abdominal Aortic Aneurysm," Br. J. Surg., **75**(8), pp. 733-736.

[3] Hoornweg, L. L., Storm-Versloot, M. N., Ubbink, D. T., Koelemay, M. J. W., Legemate, D. A., and Balm, R., 2008, "Meta Analysis on Mortality of Ruptured Abdominal Aortic Aneurysms," Euro. J. Vasc. Endovasc. Surg., **35**(5), pp. 558-570.

[4] Darling, R. C., 1970, "Ruptured Arteriosclerotic Abdominal Aortic Aneurysms. A Pathologic and Clinical Study," Am. J. Surg., **119**(4), pp. 397-401.

[5] Darling, R. C., Messina, C. R., Brewster, D. C., and Ottinger, L. W., 1977, "Autopsy Study of Unoperated Abdominal Aortic Aneurysms. The Case for Early Resection," Circulation, **56**(3 Suppl (Print)), pp. II161-164.

[6] Simao da Silva, E., Rodrigues, A. J., Magalhaes Castro de Tolosa, E., Rodrigues, C. J., Villas Boas do Prado, G., and Nakamoto, J. C., 2000, "Morphology and Diameter of Infrarenal Aortic Aneurysms: A Prospective Autopsy Study," Cardiovasc. Surg., **8**(7), pp. 526-532.

[7] Fillinger, M. F., Marra, S. P., Raghavan, M. L., and Kennedy, F. E., 2003, "Prediction of Rupture Risk in Abdominal Aortic Aneurysm During Observation: Wall Stress Versus Diameter," J. Vasc. Surg., **37**(4), pp. 724-732.

[8] Raghavan, M. L., and Vorp, D. A., 2000, "Toward a Biomechanical Tool to Evaluate Rupture Potential of Abdominal Aortic Aneurysm: Identification of a Finite Strain Constitutive Model and Evaluation of Its Applicability," J. Biomech., **33**(4), pp. 475-482.

[9] Wang, D. H., Makaroun, M., Webster, M. W., and Vorp, D. A., 2001, "Mechanical Properties and Microstructure of Intraluminal Thrombus from Abdominal Aortic Aneurysm," J. Biomech. Eng., **123**(6), pp. 536-539.

[10] Aaronson, P. I., Ward, J. P. T., and Wiener, C. M., 2004, *The Cardiovascular System at a Glance*, Blackwell Publishing, Madden, MA.

[11] Westerhof, N., Stergiopulos, N., and Noble, M. I. M., 2005, *Snapshots of Hemodynamics: An Aid for Clinical Research and Graduate Education*, Springer, New York.

[12] Cheng, C. P., Herfkens, R. J., and Taylor, C. A., 2003, "Comparison of Abdominal Aortic Hemodynamics between Men and Women at Rest and During Lower Limb Exercise," J. Vasc. Surg., **37**(1), pp. 118-123.

[13] Finol, E. A., Keyhani, K., and Amon, C. H., 2003, "The Effect of Asymmetry in Abdominal Aortic Aneurysms under Physiologically Realistic Pulsatile Flow Conditions," J. Biomech. Eng., **125**(2), pp. 207-217.

[14] Bergqvist, D., Bjorck, M., and Wanhainen, A., 2007, "Abdominal Aortic Aneurysm (AAA)," *Vascular Surgery*, C. D. Liapis, K. Balzer, F. Benedetti-Valentini, and J. Fernandes e Fernandes, eds., Springer-Verlag, Berlin.

[15] Humphrey, J. D., 2002, *Cardiovascular Solid Mechanics. Cells, Tissues, and Organs*, Springer, New York.

[16] Dobrin, P. B., Baker, W. H., and Gley, W. C., 1984, "Elastolytic and Collagenolytic Studies of Arteries. Implications for the Mechanical Properties of Aneurysms," Arch. Surg., **119**(4), pp. 405-409.

[17] Zhao, S., Suciu, A., Ziegler, T., Moore, J. E., Jr., Burki, E., Meister, J.-J., and Brunner, H. R., 1995, "Synergistic Effects of Fluid Shear Stress and Cyclic Circumferential Stretch on Vascular Endothelial Cell Morphology and Cytoskeleton," Arterioscler Thromb Vasc Biol, **15**(10), pp. 1781-1786.

[18] Choke, E., Cockerill, G., Wilson, W. R., Sayed, S., Dawson, J., Loftus, I., and Thompson, M. M., 2005, "A Review of Biological Factors Implicated in Abdominal Aortic Aneurysm Rupture," Eur. J. Vasc. Endovasc. Surg., **30**(3), pp. 227-244.

[19] Howard, J., 2001, *Mechanics of Motor Proteins and the Cytoskeleton*, Sinauer Associates, Inc., Sunderland, MA.

[20] Forester, N. D., Cruickshank, S. M., Scott, D. J., and Carding, S. R., 2006, "Increased Natural Killer Cell Activity in Patients with an Abdominal Aortic Aneurysm," Br. J. Surg., **93**(1), pp. 46-54.

[21] Galle, C., Schandene, L., Stordeur, P., Peignois, Y., Ferreira, J., Wautrecht, J. C., Dereume, J. P., and Goldman, M., 2005, "Predominance of Type 1 Cd4+ T Cells in Human Abdominal Aortic Aneurysm," Clin. Exp. Immunol., **142**(3), pp. 519-527.

[22] Bengtsson, H., Sonesson, B., and Bergqvist, D., 1996, "Incidence and Prevalence of Abdominal Aortic Aneurysms, Estimated by Necropsy Studies and Population Screening by Ultrasound," Ann. N. Y. Acad. Sci., **800**, pp. 1-24.

[23] Lederle, F. A., Johnson, G. R., Wilson, S. E., Chute, E. P., Littooy, F. N., Bandyk, D., Krupski, W. C., Barone, G. W., Acher, C. W., and Ballard, D. J., 1997, "Prevalence and Associations of Abdominal Aortic Aneurysm Detected through Screening. Aneurysm Detection and Management (Adam) Veterans Affairs Cooperative Study Group," Ann. Int. Med., **126**(6), pp. 441-449.

[24] Golledge, J., Karan, M., Moran, C. S., Muller, J., Clancy, P., Dear, A. E., and Norman, P. E., 2008, "Reduced Expansion Rate of Abdominal Aortic Aneurysms in Patients with Diabetes May Be Related to Aberrant Monocyte-Matrix Interactions," Euro. Heart J., **29**(5), pp. 665-672.

[25] Pacanowski, J. P., Stevens, S. L., Freeman, M. B., Dieter, R. S., Klosterman, L. A., Kirkpatrick, S. S., Ragsdale, J. W., Davis, S. E., and Goldman, M. H., 2002, "Endotension Distribution and the Role of Thrombus Following Endovascular Aaa Exclusion," J. Endovasc. Ther., **9**(5), pp. 639-651.

[26] Raghavan, M. L., Kratzberg, J. A., and Golzarian, J., 2005, "Introduction to Biomechanics Related to Endovascular Repair of Abdominal Aortic Aneurysm," Tech. Vasc. Interv. Radiol., **8**(1), pp. 50-55.

[27] Schurink, G. W., van Baalen, J. M., Visser, M. J., and van Bockel, J. H., 2000, "Thrombus within an Aortic Aneurysm Does Not Reduce Pressure on the Aneurysmal Wall," J Vasc Surg, **31**(3), pp. 501-506.

[28] Springer, F., Gunther, R. W., and Schmitz-Rode, T., 2008, "Aneurysm Sac Pressure Measurement with Minimally Invasive Implantable Pressure Sensors: An Alternative to Current Surveillance Regimes after Evar?," Cardiovasc. Intervent. Radiol., **31**(3), pp. 460-467.

[29] Vorp, D. A., Mandarino, W. A., Webster, M. W., and Gorcsan, J., 3rd, 1996, "Potential Influence of Intraluminal Thrombus on Abdominal Aortic Aneurysm as Assessed by a New Non-Invasive Method," Cardiovasc. Surg., **4**(6), pp. 732-739.

[30] Sonesson, B., Dias, N., Malina, M., Olofsson, P., Griffin, D., Lindblad, B., and Ivancev, K., 2003, "Intra-Aneurysm Pressure Measurements in Successfully Excluded Abdominal Aortic Aneurysm after Endovascular Repair," J. Vasc. Surg., **37**(4), pp. 733-738.

[31] Dias, N. V., Ivancev, K., Malina, M., Resch, T., Lindblad, B., and Sonesson, B., 2004, "Intra-Aneurysm Sac Pressure Measurements after Endovascular Aneurysm Repair: Differences between Shrinking, Unchanged, and Expanding Aneurysms with and without Endoleaks," J. Vasc. Surg., **39**(6), pp. 1229-1235.

[32] Holzapfel, G. A., Sommer, G., Auer, M., Regitnig, P., and Ogden, R. W., 2007, "Layer-Specific 3d Residual Deformations of Human Aortas with Non-Atherosclerotic Intimal Thickening," Ann. Biomed. Eng., **35**(4), pp. 530-545.

[33] Li, Z., and Kleinstreuer, C., 2005, "A New Wall Stress Equation for Aneurysm-Rupture Prediction," Ann. Biomed. Eng., **33**(2), pp. 209-213.

[34] Han, H. C., and Fung, Y. C., 1995, "Longitudinal Strain of Canine and Porcine Aortas," J. Biomech., **28**(5), pp. 637-641.

[35] Vos, A. W., Wisselink, W., Marcus, J. T., Vahl, A. C., Manoliu, R. A., and Rauwerda, J. A., 2003, "Cine Mri Assessment of Aortic Aneurysm Dynamics before and after Endovascular Repair," J. Endovasc. Ther., **10**(3), pp. 433-439.

[36] Hans, S. S., Jareunpoon, O., Balasubramaniam, M., and Zelenock, G. B., 2005, "Size and Location of Thrombus in Intact and Ruptured Abdominal Aortic Aneurysms," J. Vasc. Surg., **41**(4), pp. 584-588.

[37] Fillinger, M. F., Racusin, J., Baker, R. K., Cronenwett, J. L., Teutelink, A., Schermerhorn, M. L., Zwolak, R. M., Powell, R. J., Walsh, D. B., and Rzucidlo, E. M., 2004, "Anatomic Characteristics of Ruptured Abdominal Aortic Aneurysm on Conventional Ct Scans: Implications for Rupture Risk," J. Vasc. Surg., **39**(6), pp. 1243-1252.

[38] Humphrey, J. D., and Taylor, C. A., 2008, "Intracranial and Abdominal Aortic Aneurysms: Similarities, Differences, and Need for a New Class of Computational Models," Ann. Rev. Biomed. Eng., **10**(1), pp. 221-246.

[39] Badran, M. F., Gould, D. A., Raza, I., McWilliams, R. G., Brown, O., Harris, P. L., Gilling-Smith, G. L., Brennan, J., White, D., Meakin, S., and Rowlands, P. C., 2002, "Aneurysm Neck Diameter after Endovascular Repair of Abdominal Aortic Aneurysms," J. Vasc. Interv. Radiol., **13**(9 Pt 1), pp. 887-892.

[40] Arko, F. R., Hill, B. B., Reeves, T. R., Olcott, C., Harris, E. J., Fogarty, T. J., and Zarins, C. K., 2003, "Early and Late Functional Outcome Assessments

Following Endovascular and Open Aneurysm Repair," J. Endo. Ther., **10**(1), pp. 2-9.

[41] Blankensteijn, J. D., de Jong, S. E., Prinssen, M., van der Ham, A. C., Buth, J., van Sterkenburg, S. M., Verhagen, H. J., Buskens, E., Grobbee, D. E., and Dutch Randomized Endovascular Aneurysm Management Trial, G., 2005, "Two-Year Outcomes after Conventional or Endovascular Repair of Abdominal Aortic Aneurysms.[See Comment]," N. Engl. J. Med., **352**(23), pp. 2398-2405.

[42] Brooks, M. J., Brown, L. C., and Greenhalgh, R. M., 2006, "Defining the Role of Endovascular Therapy in the Treatment of Abdominal Aortic Aneurysm: Results of a Prospective Randomized Trial," Adv. Surg., **40**, pp. 191-204.

[43] Cotroneo, A. R., Iezzi, R., Giancristofaro, D., Santoro, M., Quinto, F., Spigonardo, F., and Storto, M. L., 2006, "Endovascular Abdominal Aortic Aneurysm Repair: How Many Patients Are Eligible for Endovascular Repair?," Radiol. Med., **111**(4), pp. 597-606.

[44] Veith, F. J., Baum, R. A., Ohki, T., Amor, M., Adiseshiah, M., Blankensteijn, J. D., Buth, J., Chuter, T. A., Fairman, R. M., Gilling-Smith, G., Harris, P. L., Hodgson, K. J., Hopkinson, B. R., Ivancev, K., Katzen, B. T., Lawrence-Brown, M., Meier, G. H., Malina, M., Makaroun, M. S., Parodi, J. C., Richter, G. M., Rubin, G. D., Stelter, W. J., White, G. H., White, R. A., Wisselink, W., and Zarins, C. K., 2002, "Nature and Significance of Endoleaks and Endotension: Summary of Opinions Expressed at an International Conference," J. Vasc. Surg., **35**(5), pp. 1029-1035.

[45] Chaikof, E. L., Blankensteijn, J. D., Harris, P. L., White, G. H., Zarins, C. K., Bernhard, V. M., Matsumura, J. S., May, J., Veith, F. J., Fillinger, M. F., Rutherford, R. B., Kent, K. C., and Ad Hoc Committee for Standardized Reporting Practices in Vascular Surgery of The Society for Vascular Surgery/American Association for Vascular, S., 2002, "Reporting Standards for Endovascular Aortic Aneurysm Repair," J. Vasc. Surg., **35**(5), pp. 1048-1060.

[46] He, C. M., and Roach, M. R., 1994, "The Composition and Mechanical Properties of Abdominal Aortic Aneurysms," J. Vasc. Surg., **20**(1), pp. 6-13.

[47] Vardulaki, K. A., Prevost, T. C., Walker, N. M., Day, N. E., Wilmink, A. B., Quick, C. R., Ashton, H. A., and Scott, R. A., 1998, "Growth Rates and Risk of Rupture of Abdominal Aortic Aneurysms.," Br. J. Surg., **85**(12), pp. 1674-1680.

[48] Brady, A. R., Thompson, S. G., Fowkes, F. G., Greenhalgh, R. M., Powell, J. T., and Participants, U. K. S. A. T., 2004, "Abdominal Aortic Aneurysm Expansion: Risk Factors and Time Intervals for Surveillance," Circulation, **110**(1), pp. 16-21.

[49] Love, M., Wray, A., Worthington, M., and Ellis, P., 2005, "Failure of Aneurysm Sac Shrinkage after Endovascular Repair; the Effect of Mural Calcification," Clin Radiol, **60**(12), pp. 1290-1294.

[50] Thubrikar, M. J., Labrosse, M., Robicsek, F., Al-Soudi, J., and Fowler, B., 2001, "Mechanical Properties of Abdominal Aortic Aneurysm Wall," J. Med. Eng. Technol., **25**(4), pp. 133-142.

[51] Raghavan, M. L., Kratzberg, J., Castro de Tolosa, E. M., Hanaoka, M. M., Walker, P., and da Silva, E. S., 2005, "Regional Distribution of Wall Thickness and Failure Properties of Human Abdominal Aortic Aneurysm," J. Biomech., **9**, p. 9.

[52] Marra, S. P., Daghlian, C. P., Fillinger, M. F., and Kennedy, F. E., 2006, "Elemental Composition, Morphology and Mechanical Properties of Calcified Deposits Obtained from Abdominal Aortic Aneurysms," Acta Biomat., **2**(5), pp. 515-520.

[53] Satta, J., Laara, E., and Juvonen, T., 1996, "Intraluminal Thrombus Predicts Rupture of an Abdominal Aortic Aneurysm," J Vasc Surg, **23**(4), pp. 737-739.

[54] Raghavan, M. L., Webster, M. W., and Vorp, D. A., 1996, "Ex Vivo Biomechanical Behavior of Abdominal Aortic Aneurysm: Assessment Using a New Mathematical Model," Ann. Biomed. Eng., **24**(5), pp. 573-582.

[55] Wang, D. H., Makaroun, M. S., Webster, M. W., and Vorp, D. A., 2002, "Effect of Intraluminal Thrombus on Wall Stress in Patient-Specific Models of Abdominal Aortic Aneurysm," J. Vasc. Surg., **36**(3), pp. 598-604.

[56] Watton, P. N., Hill, N. A., and Heil, M., 2004, "A Mathematical Model for the Growth of the Abdominal Aortic Aneurysm," Biomech. Model. Mechanobiol., **3**(2), pp. 98-113.

[57] Vande Geest, J. P., Wang, D. H., Wisniewski, S. R., Makaroun, M. S., and Vorp, D. A., 2006, "Towards a Noninvasive Method for Determination of

Patient-Specific Wall Strength Distribution in Abdominal Aortic Aneurysms," Ann. Biomed. Eng., **34**(7), pp. 1098-1106.

[58] Hunter, G. C., Smyth, S. H., Aguirre, M. L., Baxter, B. T., Bull, D. A., King, D. D., Wang, Y. P., Hall, K. A., and Putnam, C. W., 1996, "Incidence and Histologic Characteristics of Blebs in Patients with Abdominal Aortic Aneurysms," J. Vasc. Surg., **24**(1), pp. 93-101.

[59] Lindholt, J. S., 2008, "Aneurysmal Wall Calcification Predicts Natural History of Small Abdominal Aortic Aneurysms," Atherosclerosis, **197**(2), pp. 673-678.

[60] Vande Geest, J. P., Sacks, M. S., and Vorp, D. A., 2006, "The Effects of Aneurysm on the Biaxial Mechanical Behavior of Human Abdominal Aorta," J. Biomech., **39**(7), pp. 1324-1334.

[61] Vande Geest, J. P., Sacks, M. S., and Vorp, D. A., 2006, "A Planar Biaxial Constitutive Relation for the Luminal Layer of Intra-Luminal Thrombus in Abdominal Aortic Aneurysms," J. Biomech., **39**(13), pp. 2347-2354.

[62] Ohashi, T., Sugita, S., Matsumoto, T., Kumagai, K., Akimoto, H., Tabayashi, K., and Sato, M., 2003, "Rupture Properties of Blood Vessel Walls Measured by Pressure-Imposed Test," JSME Intl. J. Series C, **46**(No. 4 Special Issue on Bioengineering), pp. 1290-1296.

[63] Macsweeney, S. T. R., Young, G., Greenhalgh, R. M., and Powell, J. T., 1992, "Mechanical Properties of the Aneurysmal Aorta," Br. J. Surg., **79**(12), pp. 1281-1284.

[64] McDonald, D. A., 1974, *Blood Flow in Arteries*, Williams & Wilkins, Baltimore.

[65] Thubrikar, M. J., al-Soudi, J., and Robicsek, F., 2001, "Wall Stress Studies of Abdominal Aortic Aneurysm in a Clinical Model," Ann Vasc Surg, **15**(3), pp. 355-366.

[66] Vorp, D. A., Raghavan, M. L., and Webster, M. W., 1998, "Mechanical Wall Stress in Abdominal Aortic Aneurysm: Influence of Diameter and Asymmetry," J. Vasc. Surg., **27**(4), pp. 632-639.

[67] Vande Geest, J. P., Schmidt, D. E., Sacks, M. S., and Vorp, D. A., 2008, "The Effects of Anisotropy on the Stress Analyses of Patient-Specific Abdominal Aortic Aneurysms," Ann. Biomed. Eng., **36**(6), pp. 921-932.

[68] Rodriguez, J. F., Ruiz, C., Doblare, M., and Holzapfel, G. A., 2008, "Mechanical Stresses in Abdominal Aortic Aneurysms: Influence of Diameter, Asymmetry, and Material Anisotropy," J. Biomech. Eng., **130**(2), pp. 021023-021010.

[69] Vande Geest, J. P., Di Martino, E. S., Bohra, A., Makaroun, M. S., and Vorp, D. A., 2006, "A Biomechanics-Based Rupture Potential Index for Abdominal Aortic Aneurysm Risk Assessment: Demonstrative Application," Ann. N. Y. Acad. Sci., **1085**, pp. 11-21.

[70] Hinnen, J. W., Rixen, D. J., Koning, O. H., van Bockel, J. H., and Hamming, J. F., 2007, "Development of Fibrinous Thrombus Analogue for in-Vitro Abdominal Aortic Aneurysm Studies," J Biomech, **40**(2), pp. 289-295.

[71] Li, Z.-Y., U-King-Im, J., Tang, T. Y., Soh, E., See, T. C., and Gillard, J. H., 2008, "Impact of Calcification and Intraluminal Thrombus on the Computed Wall Stresses of Abdominal Aortic Aneurysm," J. Vasc. Surg., **47**(5), pp. 928-935.

[72] Di Martino, E. S., and Vorp, D. A., 2003, "Effect of Variation in Intraluminal Thrombus Constitutive Properties on Abdominal Aortic Aneurysm Wall Stress," Ann Biomed Eng, **31**(7), pp. 804-809.

[73] Canic, S., Ravi-Chandar, K., Krajcer, Z., Mirkovic, D., and Lapin, S., 2005, "Mathematical Model Analysis of Wallstent and Aneurx: Dynamic Responses of Bare-Metal Endoprosthesis Compared with Those of Stent-Graft," Tex. Heart. Inst. J., **32**(4), pp. 502-506.

[74] Li, Z., Kleinstreuer, C., and Farber, M., 2005, "Computational Analysis of Biomechanical Contributors to Possible Endovascular Graft Failure," Biomech. Model. Mechanobiol., **4**(4), pp. 221-234.

[75] Li, Z., and Kleinstreuer, C., 2006, "Analysis of Biomechanical Factors Affecting Stent-Graft Migration in an Abdominal Aortic Aneurysm Model," J. Biomech., **39**(12), pp. 2264-2273.

[76] Tan, J. W., Yeo, K. K., and Laird, J. R., 2008, "Food and Drug Administration-Approved Endovascular Repair Devices for Abdominal Aortic Aneurysms: A Review," J. Vasc. Interv. Radiol., **19**(6 Suppl), pp. S9-S17.

[77] Fallone, B. G., Wallace, S., and Gianturco, C., 1988, "Elastic Characteristics of the Self-Expanding Metallic Stents," Invest. Radiol., **23**(5), pp. 370-376.

[78] Agrawal, C. M., and Clark, H. G., 1992, "Deformation Characteristics of a Bioabsorbable Intravascular Stent," Invest Radiol, **27**(12), pp. 1020-1024.

[79] Schwartz, S. A., Taljanovic, M. S., Smyth, S., O'Brien, M. J., and Rogers, L. F., 2007, "Ct Findings of Rupture, Impending Rupture, and Contained Rupture of Abdominal Aortic Aneurysms," Am. J. Roentgenol., **188**(1), pp. W57-62.

[80] Smith, D. B., Sacks, M. S., Vorp, D. A., and Thornton, M., 2000, "Surface Geometric Analysis of Anatomic Structures Using Biquintic Finite Element Interpolation," Ann. Biomed. Eng., **28**(6), pp. 598-611.

[81] Steinman, D. A., 2002, "Image-Based Computational Fluid Dynamics Modeling in Realistic Arterial Geometries," Ann. Biomed. Eng., **30**(4), pp. 483-497.

[82] Doyle, B. J., Callanan, A., and McGloughlin, T. M., 2007, "A Comparison of Modelling Techniques for Computing Wall Stress in Abdominal Aortic Aneurysms," Biomed. Eng. OnLine, **6**, p. 38.

[83] MSC.Software, 2006, "Msc.Marc Volume C: Program Input," Santa Ana, CA.

[84] Reddy, J. N., 2003, *An Introduction to the Finite Element Method*, Tata-McGraw-Hill, Dehli.

[85] Bonet, J., and Wood, R. D., 1997, *Nonlinear Continuum Mechanics for Finite Element Analysis*, Cambridge University Press, New York.

[86] MSC.Software, 2006, "Msc.Marc Volume A: Theory and User Information," Santa Ana, CA.

[87] Stringfellow, M. M., Lawrence, P. F., and Stringfellow, R. G., 1987, "The Influence of Aorta-Aneurysm Geometry Upon Stress in the Aneurysm Wall," J. Surg. Res., **42**(4), pp. 425-433.

[88] Mower, W. R., Baraff, L. J., and Sneyd, J., 1993, "Stress Distributions in Vascular Aneurysms: Factors Affecting Risk of Aneurysm Rupture," J. Surg. Res., **55**(2), pp. 155-161.

[89] Inzoli, F., Boschetti, F., Zappa, M., Longo, T., and Fumero, R., 1993, "Biomechanical Factors in Abdominal Aortic Aneurysm Rupture," Euro. J. Vasc. Surg., **7**(6), pp. 667-674.

[90] Elger, D. F., Blackketter, D. M., Budwig, R. S., and Johansen, K. H., 1996, "The Influence of Shape on the Stresses in Model Abdominal Aortic Aneurysms," J. Biomech. Eng., **118**(3), pp. 326-332.

[91] Mower, W. R., Quinones, W. J., and Gambhir, S. S., 1997, "Effect of Intraluminal Thrombus on Abdominal Aortic Aneurysm Wall Stress.," J. Vasc. Surg., **26**(4), pp. 602-608.

[92] Thubrikar, M. J., Agali, P., and Robicsek, F., 1999, "Wall Stress as a Possible Mechanism for the Development of Transverse Intimal Tears in Aortic Dissections," J. Med. Eng. Technol., **23**(4), pp. 127-134.

[93] Criscione, J. C., 2003, "Rivlin's Representation Formula Is Ill-Conceived for the Determination of Response Functions Via Biaxial Testing," J. Elasticity, **70**(1-3), pp. 129-147.

[94] Bayer, I. M., Adamson, S. L., and Langille, B. L., 1999, "Atrophic Remodeling of the Artery-Cuffed Artery," Arterioscler. Thromb. Vasc. Biol., **19**(6), pp. 1499-1505.

[95] Vande Geest, J. P., 2005, "Towards an Improved Rupture Potential Index for Abdominal Aortic Aneurysms: Anisotropic Constitutive Modeling and Noninvasive Wall Strength Estimation.," Ph.D. Thesis, University of Pittsburgh.

APPENDIX A

Table 19. Average von Mises stress and Average Maximum Principal stress in models.

Pressure	Patient	Time Point	Graft Stiffness Parameters	Avg von Mises Stress (kPa)	Avg Maximum Principal Stress (kPa)
16 kPa (lumen)	A ("stable")	Pre	-	116.7	122.9
16 kPa (wall)	A	Pre	-	115.3	124.9
16 kPa (no thrombus)	A	Pre	-	124.4	134.4
16 kPa	A	Early Follow-Up	10.0 MPa	21.9	20.5
16 kPa	A	Early Follow-Up	1.0 MPa	51.2	51.2
16 kPa	A	Early Follow-Up	0.10 MPa	77.3	77.3
16 kPa	A	Early Follow-Up	- (no graft)	87.8	91.5
16 kPa	A	Early Follow-Up	Combo (1/10 MPa)	29.4	27.8
16 kPa	A	Late Follow-Up	1 MPa	33.0	31.4
16 kPa	A	Late Follow-Up	10 MPa	17.7	17.0
16 kPa	A	Late Follow-Up	Combo (1/10 MPa)	28.2	26.9
16 kPa (lumen)	B ("shrinking")	Pre	-	80.9	84.0
16 kPa (no thrombus)	B	Pre	-	149.6	159.1
16 kPa	B	Early Follow-Up	10.0 MPa	13.1	12.9
16 kPa	B	Early Follow-Up	1.0 MPa	31.3	31.2
16 kPa	B	Early Follow-Up	Combo (1/10 MPa)	21.6	20.8
16 kPa	B	Late Follow-Up	1.0 MPa	38.0	38.8
16 kPa	B	Late Follow-Up	Combo (1/10 MPa)	25.3	24.5
10.667 kPa	A	Pre	-	72.8	76.5
10.667 kPa	A	Early Follow-Up	Combo (1/10 MPa)	14.7	13.7
10.667 kPa	B	Pre	-	50.1	53.8
10.667 kPa	B	Early Follow-Up	Combo (1/10 MPa)	13.9	13.3

APPENDIX B

The cyclic strain of the aneurysm in response to loading is of interest as well as stress because strain can be inferred more directly from gated CT measurements that show shape change over time. However, what is shown here is strain relative to unloaded configuration. In this study, maximum principal strain is reduced, much like von Mises stress, in response to endograft treatment. The largest reductions occur in the sac region and there are rearrangements and some reduction in strains in the neck after endograft treatment. The areas of high strain correspond to the areas of high stress (compare Figure 32 and Figure 33 with Figure 48 and Figure 49).

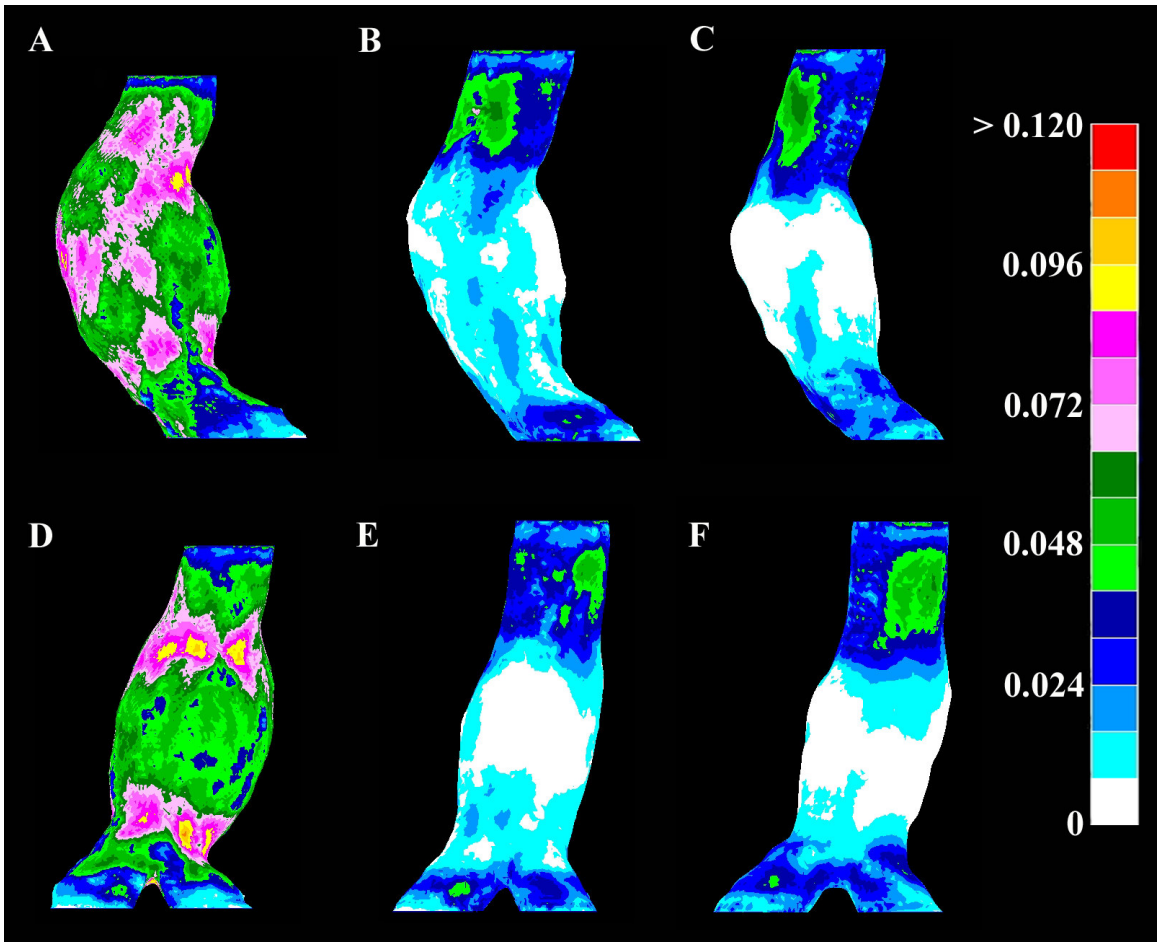

Figure 48. Maximum principal strain in patient A (stable). A) side view of untreated, B) side view of early follow-up, C) side view of late follow-up D) rear view of untreated, E) rear view of early follow-up and F) rear view of late follow-up.

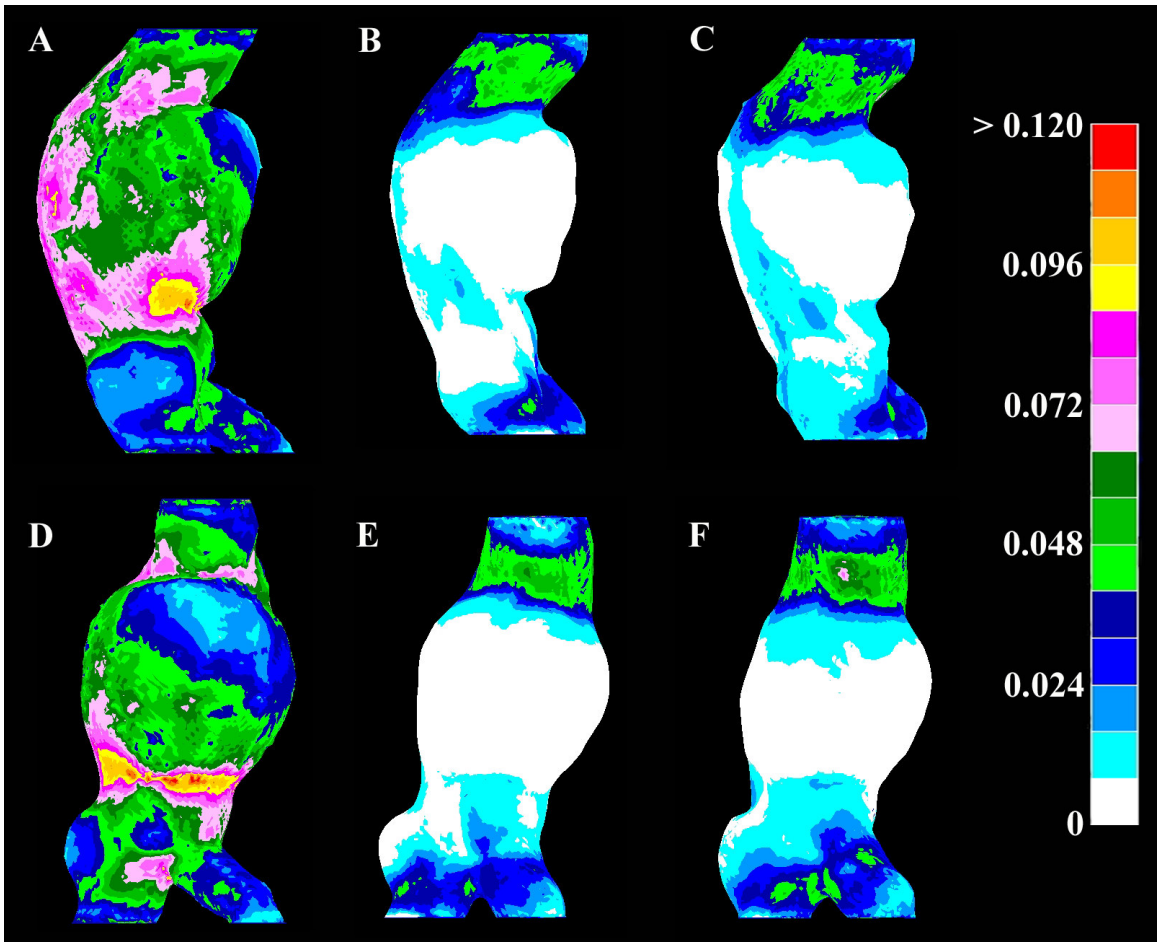

Figure 49. Maximum principal strain in patient B (shrink). A) side view of untreated, B) side view of early follow-up, C) side view of late follow-up D) rear view of untreated, E) rear view of early follow-up and F) rear view of late follow-up.

VITA

Name:	Clark Andrew Meyer
Address:	337 Zachry Engineering Center MS 3120 College Station, TX 77843-3120
Email Addresses:	clarkmeyer@tamu.edu, clarkmeyer@gmail.com
Education:	B.S., Biomedical Engineering, Texas A&M University, 2002 Ph.D., Biomedical Engineering, Texas A&M University, 2009